Citation (APA)
Soman, S. (2026). *High-Speed: Coherent fourier scatterometry*. [Dissertation (TU Delft), Delft University of Technology]. https://doi.org/10.4233/uuid:88cd1453-8898-4b1d-9963-5edf36b9c758

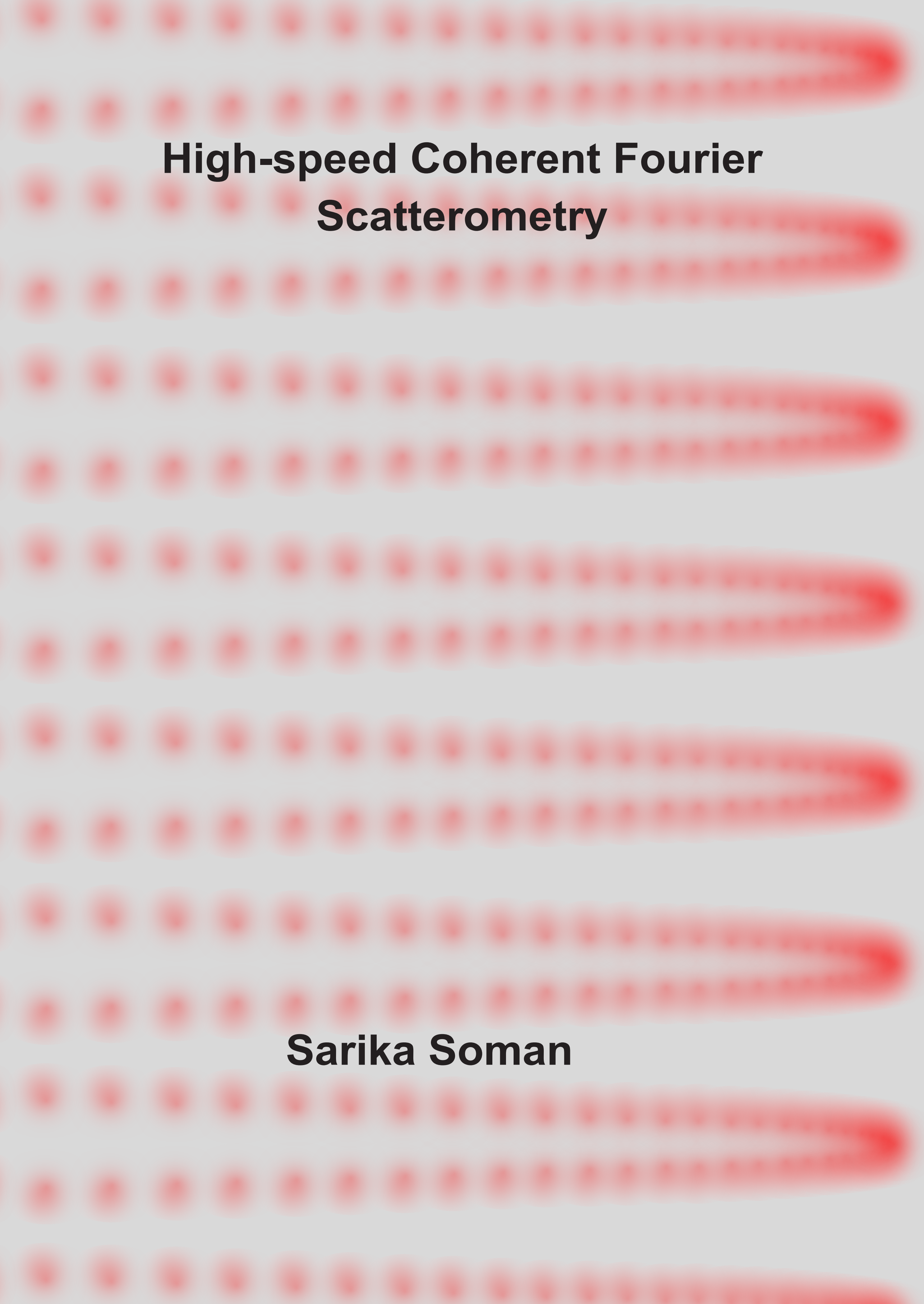

High-speed Coherent Fourier Scatterometry

Sarika Soman

HIGH-SPEED

COHERENT FOURIER SCATTEROMETRY

HIGH-SPEED
COHERENT FOURIER SCATTEROMETRY

Dissertation

for the purpose of obtaining the degree of
at Delft University of Technology
by the authority of the Rector Magnificus,
Prof.dr.ir. H. Bijl,
chair of the Board for Doctorates
to be defended publicly on
Monday, 11 May 2026, 17:30

by

Sarika SOMAN

This dissertation has been approved by the (co)promotors.

Composition of the doctoral committee:

Rector Magnificus,	chairperson
Dr. ir. S.F. Pereira,	Delft University of Technology, promotor
Dr. O. El Gawhary,	Delft University of Technology, copromotor
Independent members:	
Prof. dr. ir. J.P. Hoogenboom,	Delft University of Technology
Dr. N. Bhattacharya,	Delft University of Technology
Prof. dr. ir. H. Ottevaere,	Vrije Universiteit Brussel
Prof. dr. A.P. Mosk,	Utrecht University
Dr. P. van der Walle,	TNO Science and Industry
Prof. dr. B. Rieger,	Delft University of Technology, *reserve member*

Keywords: coherent Fourier scatterometry; optical metrology; scanning; high-speed

Printed by: proefschriftenprinten.nl

Front & Back: Sarika Soman.

CONTENTS

SUMMARY

In a wide range of manufacturing industries, including semiconductors, photonics, transportation, healthcare and energy storage, there is a need for increasingly smaller structures with strict tolerances. To continue this trend, fast, non-destructive, and traceable metrology that can keep pace with these developments is essential. Although electron and scanning probe microscopies have excellent spatial resolution, they suffer from low throughput, stringent measurement conditions, and can be destructive to the sample. On the other hand, optics-based techniques are attractive for fast, non-contact metrology in manufacturing environments. Coherent Fourier scatterometry (CFS) meets this need by providing an optical measurement solution that uses low light power, is non-destructive, and has a simple optical design. The technique involves focusing a coherent beam onto a diffraction-limited spot, collecting the field scattered in the Fourier plane after interaction with the sample. By scanning the spot across the surface, a scattering map is constructed from which parameters of the structures can be derived using a forward simulation model. Since scanning time accounts for most of the total measurement time, this thesis focuses on accelerating CFS by investigating different approaches, such as probe multiplexing and non-raster scanning, to increase the scanning speed. The central research question is how each of these options balances speed, optical complexity, alignment effort, and the overall noise floor of the system.

Chapter 1 places CFS in the broader metrology landscape and describes its unique advantages and disadvantages, including the need for scanning systems with high throughput capacity. The chapter also outlines the approach of the thesis and provides a brief overview of the other chapters.

Chapter 2 develops the basic theory and modelling of CFS that underlines all subsequent designs, from scalar to vectorial descriptions of a highly focused probe and differential detection in the Fourier plane, to rigorous forward solvers that predict Fourier plane signatures for known structures. Aberrations, electronic bandwidth, and input power limitations collectively determine the smallest features that can be measured at a given speed.

Chapter 3 investigates the practical detection limits in CFS by analysing how low-order aberrations reshape the focal field distribution, the scattered field recorded in the Fourier plane, and the corresponding measured difference signal. It also describes how the focus criteria derived from the signal peak-to-peak can deviate from the actual best focus position and how scan trajectories and power budgets interact with detector and electronic limits to determine the operating windows.

Chapter 4 implements multi-beam CFS by parallelising the scanning using multiple focused spots. A diffractive beam splitter produces multiple spots that share a common focal plane, and a microlens/detector relay ensures independent readout. The research approach validates independent detection on sparsely populated particle samples. In addition, a calibration curve was created using a Si sample with etched silicon wells of different diameters, followed by the development of a phase correlation algorithm to link the overlapping scan areas. The method offers linear throughput gains for a given area as a function of the number of probes but requires precise alignment and careful management of off-axis deviations.

Chapter 5 replaces the fast raster scan axis with a galvanometric mirror to achieve scans at kHz speeds. The fast galvo scan is synchronised with a low-speed piezo axis. An angle-dependent beam shift that occurs at the detector plane, caused by the position of the mirror relative to the rear focal plane of the objective is modelled. The chapter also describes the calibration of the diameters of etched pits on a Si sample and provides an overview of the contribution of measurement uncertainty from diverse sources. Galvo scanning provides an order of magnitude faster scan times with compact hardware, at the expense of angle-dependent beam shifts at the detector and field aberration management.

Chapter 6 discusses a rotation-based CFS example in which the fast axis undergoes continuous angular motion in combination with radial steps using a slow piezo. Using a procedure for minimising frequency dispersion, the actual rotation axis can be determined directly from the frequency spectrum of the measured CFS signal to correct for errors in probe centring. The axial wobble is quantified using a depth response curve of the CFS signal and is measured to less than one micrometer. The polar data is mapped onto 2D Cartesian coordinates after compensation for the deviations in probe centring.

Chapter 7 demonstrates scanning with a digital micromirror device (DMD) without macroscopic moving parts by moving Fresnel zone plates (FZPs) on the DMD. The scan signal per position is normalised by the input power to compensate for the non-uniform input beam. The FZP patterns are also adapted to combine aberration correction patterns for each scan position, enabling fast scanning with aberration correction without the need for additional hardware. The main disadvantage of this scanning technique is the poor utilisation of the input power.

Chapter 8 provides an overview of different scanning strategies, comparing scanning parameters and the advantages and disadvantages of different techniques. It is important to note that the figures do not represent final values, but only correspond to the specific implementations discussed in the previous chapters. The scanning speed is a compromise between input power, electronic bandwidth, and system complexity. Each technique has unique advantages and disadvantages and must be chosen with specific applications in mind.

SAMENVATTING

In een breed scala aan productie-industrieën, waaronder de halfgeleider-, fotonica-, transport-, gezondheidszorg- en energieopslagsector, bestaat een groeiende behoefte aan steeds kleinere structuren met strikte toleranties. Om deze trend voort te zetten is snelle, niet-destructieve en traceerbare metrologie die gelijke tred kan houden met deze ontwikkelingen essentieel. Hoewel elektronen- en scanning-probe-microscopieën een uitstekende ruimtelijke resolutie bieden, hebben zij een lage doorvoersnelheid, vereisen zij stringente meetcondities en kunnen zij destructief zijn voor het monster. Optisch gebaseerde technieken zijn daarentegen aantrekkelijk voor snelle, contactloze metrologie in productieomgevingen. Coherent Fourier-scatterometrie (CFS) voorziet in deze behoefte door een optische meetoplossing te bieden die weinig lichtvermogen gebruikt, niet-destructief is en een eenvoudige optische opstelling heeft. De techniek omvat het focussen van een coherente bundel op een diffractielimietspot en het verzamelen van het veld dat na interactie met het monster in het Fourier-vlak wordt verstrooid. Door de spot over het oppervlak te scannen, wordt een verstrooiingskaart opgebouwd waarvan structuurparameters kunnen worden afgeleid met behulp van een voorwaarts simulatiemodel. Aangezien de scantijd het grootste deel van de totale meettijd bepaalt, richt dit proefschrift zich op het versnellen van CFS door verschillende benaderingen te onderzoeken, zoals probe-multiplexing en niet-rastergebaseerd scannen, om de scansnelheid te verhogen. De centrale onderzoeksvraag is hoe elk van deze opties snelheid, optische complexiteit, uitlijningsinspanning en de algehele ruisvloer van het systeem in balans brengt.

Hoofdstuk 1 plaatst CFS in het bredere metrologielandschap en beschrijft de unieke voor- en nadelen, waaronder de noodzaak van scansystemen met hoge doorvoercapaciteit. Het hoofdstuk schetst ook de aanpak van het proefschrift en geeft een kort overzicht van de overige hoofdstukken.

Hoofdstuk 2 ontwikkelt de basistheorie en modellering van CFS die aan alle daaropvolgende ontwerpen ten grondslag ligt, van scalair tot vectorieel beschreven sterk gefocusseerde probes en differentiële detectie in het Fourier-vlak, tot rigoureuze forwardsolvers die Fourier-vlaksignaturen voorspellen voor bekende structuren. Aberraties, elektronische bandbreedte en beperkingen in het invoervermogen bepalen gezamenlijk de kleinste kenmerken die bij een gegeven snelheid kunnen worden gemeten.

Hoofdstuk 3 onderzoekt de praktische detectielimieten van CFS door te analyseren hoe laag-orde-aberraties de brandveldverdeling, het verstrooide veld in het Fourier-vlak en het overeenkomstige gemeten differentiesignaal vervormen. Het hoofdstuk beschrijft ook hoe de focuscriteria, afgeleid uit de piek-tot-piek van het signaal, kunnen afwijken van de werkelijke beste focuspositie en hoe scantrajecten en vermogensbudgetten interageren met detector- en elektronicalimieten om de operationele vensters te bepalen.

Hoofdstuk 4 implementeert multi-beam CFS door het scannen te paralleliseren met meerdere gefocusseerde spots. Een diffractieve bundelsplitser genereert meerdere spots

die een gemeenschappelijk brandvlak delen, terwijl een microlens-/detectorrelais voor onafhankelijke uitlezing zorgt. De onderzoeksaanpak valideert onafhankelijke detectie op schaars bevolkte deeltjesmonsters. Daarnaast werd een calibratiecurve opgesteld met behulp van een Si-monster met geëtste siliciumputten van verschillende diameters, gevolgd door de ontwikkeling van een fasecorrelatie-algoritme om de overlappende scangebieden te koppelen. De methode biedt lineaire doorvoersnelheidswinst voor een gegeven gebied als functie van het aantal probes, maar vereist nauwkeurige uitlijning en zorgvuldig beheer van off-axis afwijkingen.

Hoofdstuk 5 vervangt de snelle raster-scan-as door een galvanometrische spiegel om scans op kHz-snelheden te realiseren. De snelle galvo-scan wordt gesynchroniseerd met een langzame piezo-as. Een hoekafhankelijke bundelverschuiving die optreedt in het detectorvlak, veroorzaakt door de positie van de spiegel ten opzichte van het achterste brandvlak van het objectief, wordt gemodelleerd om het bruikbare galvo-hoekbereik te bepalen. Het hoofdstuk beschrijft ook de calibratie van de diameters van geëtste putten op een Si-monster en geeft een overzicht van de bijdragen van meetonzekerheden uit diverse bronnen. Galvo-scanning levert een orde van grootte snellere scantijden met compacte hardware, ten koste van hoekafhankelijke bundelverschuivingen bij de detector en het beheer van veldaberraties.

Hoofdstuk 6 bespreekt een rotatiegebaseerd CFS-voorbeeld waarin de snelle as een continue hoekbeweging ondergaat in combinatie met radiale stappen via een langzame piezo. Met behulp van een procedure voor het minimaliseren van frequentiedispersie kan de daadwerkelijke rotatie-as direct worden bepaald uit het frequentiespectrum van het gemeten CFS-signaal, om fouten in de positionering van de probe te corrigeren. De axiale “wobble” wordt gekwantificeerd aan de hand van een diepte-responskromme van het CFS-signaal en blijkt kleiner dan één micrometer. De polaire data wordt na compensatie voor afwijkingen in de probe-centrering omgerekend naar 2D Cartesische coördinaten.

Hoofdstuk 7 demonstreert scannen met een digital micro-mirror device (DMD) zonder macroscopische bewegende delen door Fresnel-zoneplaten (FZP’s) op de DMD te verplaatsen. Het scansignaal per positie wordt genormaliseerd op het invoervermogen om te compenseren voor de niet-uniforme invoerbundel. De FZP-patronen worden ook aangepast om aberratiecorrectiepatronen voor elke scanpositie te combineren, wat snel scannen met aberratiecorrectie mogelijk maakt zonder de noodzaak voor extra hardware. Het belangrijkste nadeel van deze scan techniek is het geringe rendement van het invoervermogen.

Hoofdstuk 8 biedt een overzicht van verschillende scanstrategieën, waarbij scanparameters en de voor- en nadelen van verschillende technieken worden vergeleken. Het is belangrijk op te merken dat de weergegeven waarden geen eindwaarden vormen, maar enkel betrekking hebben op de specifieke implementaties die in de voorgaande hoofdstukken zijn besproken. De scansnelheid is een compromis tussen invoervermogen, elektronische bandbreedte en systeemcomplexiteit. Elke techniek heeft unieke voor- en nadelen en moet worden gekozen met specifieke toepassingen in gedachten.

1

INTRODUCTION

Sarika Soman

When you can measure what you are speaking about, and express it in numbers, you know something about it; but when you cannot measure it, when you cannot express it in numbers, your knowledge is of a meagre and unsatisfactory kind: it may be the beginning of knowledge, but you have scarcely, in your thoughts, advanced to the stage of science, whatever the matter may be.

Lord Kelvin

Metrology drives progress across a wide range of fields from semiconductors to nano-medicine. This chapter introduces coherent Fourier scatterometry (CFS) as an optical metrology tool that uses a focused spot as a probe to characterise nano-structures, while highlighting one of its principal limitations: long measurement time. Competing metrology tools are surveyed, their strengths and shortcomings compared, and CFS is positioned within this landscape. The chapter concludes with a discussion on possible approaches to solve the problem of long scanning time.

1.1. IMPORTANCE OF METROLOGY

THE history of metrology mirrors the history of humans. Every milestone in human achievement also marks a step in the advancement of tools of measurement. “Man is the measure of all things”, said Protagoras [1]. While he likely meant this in a philosophical sense, for early societies, this statement had a more literal meaning. Body-based units of measurement were used as convenient measurement standards across the world [2]. In ancient Egypt, a cubit (the length of the pharaoh’s arm from his elbow to the fingertip) was used as a standardised unit of measurement [3]. The lengths were marked in black granite and stored in temples as references [4]. In fact they were so serious that the priests who failed to recalibrate the cubit standard on time were beheaded [5]. The use of such standards greatly aided the commerce and trade at the time. As civilizations advanced, so too did their need for precision. This is exemplified by the steam engine, a symbol of the first industrial revolution. Manufacturing its cylinders demanded such tight tolerances that uniformity was said to be "within the thickness of a worn shilling" [6]. It is no coincidence that James Watt, the engineer who invented the rotary steam engine, also invented the screw micrometer, a tool capable of measuring differences of just a few microns. He made it a standard practice in his factories, proving that no meaningful innovation happens without the ability to measure precisely.

As technology advances, metrology tools face increasing pressure to keep up. Where measuring a micron was a challenge more than 300 years ago, today we routinely deal in nanometers, or even smaller. This demand is driven by the widespread adoption of nanotechnology across industries and its infiltration into everyday products. Nanostructures and nanoscale devices are no longer confined to academic research or niche sectors; they are embedded in the chips powering our electronics, in pharmaceuticals enabling targeted drug delivery, in lightweight composites used in aircraft and electric vehicles and in energy technologies from high-efficiency solar cells to next-generation batteries [7]–[13]. The age-old adage “you make what you measure” has never been more relevant. Metrology is a core enabler of modern manufacturing and innovation. In industries striving for near-zero defects, such as those adhering to Six Sigma standards, measurement has evolved from a product-level concern to a process-level imperative [14]. Producing fewer than 3.4 defects per million means every aspect of production must be tightly monitored and controlled, and that starts with measurement.

A classic example of the critical role of metrology is the semiconductor industry. The ongoing miniaturisation in electronics has been fuelled by the ability to precisely manufacture and monitor ever-smaller components. Modern integrated circuits now contain billions of transistors, each built using complex nano-fabrication processes involving multiple layers of different materials. At the “2 nm” node, the gate pitch has shrunk to just 45 nm (still some way from 2 nm) [15]. Device architectures have evolved from planar transistors to gate-all-around (GAA) nanosheet transistors and even to sequential or monolithic 3D field-effect transistors (FETs) [16]–[19]. These innovations not only introduce finer geometries but also highly complex three-dimensional shapes, often incorporating heterogeneous materials like III-V compounds, and 2D materials [20], [21]. With nodes approaching physical limits, metrology now faces a convergence of challenges: stochastic variation, materials diversity, and architectural complexity [15]. Tools must be capable of measuring at sub-nanometer resolution, operate in-line and nondestructively, and adapt to hybrid materials and advanced process flows.

While the semiconductor industry has benefited from decades of metrology-driven refinement, emerging fields may depend on it even more critically. Nanomedicine and nano-enabled medical device therapeutics exemplify this need. Positioned at the intersection of biology, pharmacology, microfluidics, advanced materials, and photonics, these technologies are tackling complex medical challenges that traditional approaches cannot always solve. Breakthroughs such as COVID mRNA vaccines and over 50 clinically approved nanomedicine formulations demonstrate their rising importance, with many more than 400 in clinical trials [22]–[24]. To ensure safety, efficacy, and regulatory compliance, accurate measurement of critical quality attributes like particle size, size distribution, surface properties, and drug loading is essential [25]–[28]. This calls for dedicated measurement strategies not only during development but throughout the manufacturing process. The increasing number of research projects focused on refining metrology standards for nanomedicine reflects the urgency and complexity of this requirement [29].

1.2. SURFACE METROLOGY

Every metrology tool has three basic components: a probe, interaction between the probe and the sample, and a detector to record the effect of the interaction. For surface measurement tools, the probe can be a mechanical structure such as in stylus-based tools, electromagnetic fields such as optical or electron microscopy, or even acoustic waves [30]. Atomic Force Microscopy (AFM) is one of the most widely used stylus-based measurement techniques [31], [32]. As the probe scans the sample surface, attractive or repulsive surface forces cause the probe to deflect. A laser beam reflected off the probe is detected by a photodetector, converting the deflection into an accurate surface topography map at the nanometer scale. The advantage of using an AFM is that the sample topography information can be measured with high spatial resolution along both lateral and axial directions. One of the major disadvantages is that the measurement process is contact-based and quite slow, limiting its use to small scan areas and for reference measurements. There is also the issue of tip wear and contamination, causing tip replacement after prolonged use [33]–[36].

A complementary technique is scanning electron microscopy (SEM) [37]. It uses a focused electron beam to scan the sample and records the backscattered electrons. SEM has high spatial resolution and can also give additional material information about the sample [38]. However, the measurement can be damaging to delicate samples such as biological specimens, metal oxide semiconductor field effect transistor (MOSFET) logic gates, and for non-conducting samples, additional coatings are often required to increase contrast [35], [39]–[41]. It also requires high vacuum conditions, which can be challenging during production. These examples underscore a common challenge in metrology: the trade-off between resolution, speed, and sample compatibility. High-resolution tools often struggle with throughput and stringent measurement conditions, making them less ideal for high-volume manufacturing environments.

Optical metrology tools use electromagnetic waves in the optical spectral range as the probe [42]–[44]. It includes a wide range of tools such as interferometry, scanning microscopy, scatterometry, speckle-based techniques, fringe-projection and so on [45]–

[50]. These tools use different properties of light such as intensity, phase and polarisation to retrieve information about the sample. Optical tools are advantageous due to their non-contact and non-destructive measurements, fast measurement times, and capability to measure large scan areas. The biggest disadvantage however is the limited spatial resolution. Spatial resolution is inversely proportional to the wavelength of the field used as the probe and the smaller the wavelength, the better the resolution. Electron beams have a much shorter wavelength (0.0388 nm for 1 keV) compared to light in the visible range (400-700 nm), enabling the superior spatial resolution for the electron microscopy tools. Prior information about the sample can help resolve the information in the measurement which is highly non-linearly entangled in the signal.

Scatterometry refers to a branch of metrology techniques in which changes in the light scattered off a sample combined with *a priori* information is used to infer certain properties of the sample [49], [51]. When light interacts with a structure on the sample surface, the scattered field encodes a unique “fingerprint” of that structure in its polarisation state, diffraction intensities or phase. By comparing this measured fingerprint with the response predicted by an accurate electromagnetic model of the sample, an inverse problem is solved that yields quantitative parameters such as film thickness, critical dimension (CD), side-wall angle or refractive index [52]–[55]. Variants of optical scatterometry such as spectroscopic scatterometry, fixed-angle scatterometry and spectroscopic ellipsometry differ mainly in which part of the fingerprint they record (wavelength-dependent intensity, angular distribution, or polarisation changes) [56]–[58]. All three can reconstruct sub-nanometer variations in material or geometric properties, yet their applicability is limited by poor lateral resolution because their probe beams are only weakly focused or even collimated; the illuminated spot typically spans tens to hundreds of micrometers [49].

Coherent Fourier scatterometry (CFS) fills this niche. By tightly focusing a coherent light beam with a high-NA objective and analysing the complete diffraction pattern in the Fourier plane of the objective, CFS preserves the parameter sensitivity inherent to scatterometric techniques while shrinking the spot to the diffraction limit (spot size $\approx 0.55\,\mu\text{m}$ for $\lambda = 405$ nm, NA = 0.9) [59]. Consequently, CFS enables classical scatterometry-style parameter extraction together with the lateral resolution required for mapping sub-wavelength structures. An additional advantage is that since CFS collects all the light reflected from the sample, the input power is a few orders of magnitude lower compared to similar dark field techniques with comparable sensitivity. Having detection capabilities limited only by the noise floor along with high spatial resolution makes CFS a powerful tool. The technique has been employed with great success across a wide range of applications, including diffraction grating characterisation, label-free nerve crossing detection, killer-defect detection on SiC layer for power electronics, shape determination of sub-wavelength structures, and nanoparticle characterisation on Si wafers and plastic substrates [60]–[64].

When CFS is used for large area inspection of defects, contamination and detection of isolated particles on surfaces, the small focused spot needs to be scanned across the sample to map the entire area of interest. Typically this necessitates the use of piezo-based scanning stages often having sub-nanometer positioning accuracy and repeatability. The fast axis follows a triangular waveform while the slow axis moves incrementally following a staircase pattern or slow ramp as illustrated in Figure 1.1. These systems, while being precise, are slow and can limit the range of applications in which CFS can be used [65]. For instance, in high-throughput environments such as fast-moving production lines, the in-line metrology tools must keep pace with the production requirements. Furthermore, during measurements over a large area (a few millimeters), the scanning time can increase from a few tens of minutes to a few hours. The system can undergo significant drift within the duration of one measurement contributing to measurement uncertainties. This can pose a significant challenge in the adoption of CFS as a commercial metrology tool. For comparison, Table 1.1 shows the scanning times of a piezo-based CFS system and comparable commercial metrology tools. The order-of-magnitude difference in the scanning time is a daunting deterrent.

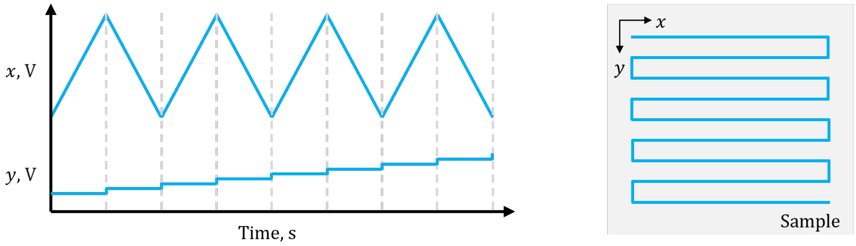

(a) (b)

Figure 1.1: a) Input waveforms for fast (x) and slow (y) axes, b) combined 2D raster scan pattern.

Table 1.1: Side-by-side comparison of different surface-inspection tools.

Technique	**Scan time for** 100 µm × 100 µm	**Pros**	**Cons**
AFM	Very slow. Scan time ≈27.7 min for pixel size of 10 nm and 60 kHz feedback loop bandwidth [66].	Excellent lateral and vertical resolution; Absolute 3D topography; Compatible with different surfaces.	Slow with limited field of view; Needs regular tip replacement due to tip wear; Can be potentially damaging to the sample surface;

Continued on next page

Technique	**Scan time for** 100 µm × 100 µm	**Pros**	**Cons**
SEM	Slow. Scan time ≈75 s with dwell time of 10 µs and pixel size 36.6 nm [67].	Excellent lateral resolution; Elemental and crystallographic studies possible.	Stringent measurement conditions; requires high/ultra-high vacuum; charging effects for non-conducting samples; can cause sample contamination due to carbon deposition.
Dark-field	Very fast. Scan time ≈0.003 s for a system using 193 nm wavelength to detect contaminants >35 nm[1] [68].	High throughput; High sensitivity to scatterers; Simple optics design.	Requires high laser power; Dynamic range limits detection near edges due to detector saturation; Model-based inference; Difficulty in measuring low-contrast particles.
Confocal microscopy	Fast. Scan time of ≈0.06 s with a pixel size of 100 nm using rotating polygons [69].	Good lateral and axial resolution.	Complicated optical system; Low signal-to-noise ratio for small and low contrast particles; Correction required for off-axis beam aberrations.

Continued on next page

Technique	**Scan time for** 100 µm × 100 µm	**Pros**	**Cons**
CFS — piezo-based	Slow. Scan time 300 s for a system with pixel size of 100 nm [2].	Good lateral resolution and axial resolution; High sensitivity to low-contrast scatterers; Simple optics design; Low power ideal for delicate samples; Possible to retrieve the size and shape of sub-wavelength nanostructures [64], [70], [71].	Slow; Model-based inference.

1.3. RESEARCH QUESTION

CFS is a low power, sensitive metrology tool with good spatial resolution. Adding fast scan speed to the arsenal can increase the range of applications of CFS-based tools to those requiring high throughput or video-rate measurements. The goal of this thesis is to investigate the use of non-piezo based scanning platforms to replace one or both scan axes and the implementation of parallel probe illumination. The study does not focus on the design or mechanical properties of the scanning systems but only on its impact on the CFS scan signal.

KEY QUESTIONS

1. What are the different ways to improve the scanning speed of the system?
2. How can they be adapted to be used in CFS systems?
3. What is the influence of each scheme on the system performance?

1.3.1. THESIS APPROACH

The primary aim of this research is to enhance the scanning speed of CFS systems, making them more suitable for high-throughput and dynamic measurement environments. To accomplish this, various strategies are explored. In literature, some approaches involve improving the mechanical design of scanning stages - for instance, designing flexure-guided nano-positioning stages with resonant frequencies exceeding several kilo Hertz [72], [73]. Such designs exploit the advantages of compliant mechanisms, thereby increasing achievable scanning speeds while maintaining high

---

[1] Polystyrene latex (PSL) particle equivalent.

[2] Scan frequency = 1/35 of the first resonant frequency of the piezo (P-625.2 CD, Physik Instrumente).

positional accuracy [65], [74]. However, in this thesis, we specifically adopt a complementary strategy, integrating existing high-speed optical scanning devices such as galvanometric mirrors, rotating polygon mirrors, resonant mirrors, acousto-optic modulators, digital micro-mirror devices (DMD), rotational stages and so on into conventional CFS setups [75]–[82]. The existing CFS designs are adapted for each scanning strategy. The research evaluates the impact of these optical adaptations on measurement signals, in terms of the influence on signal-to-noise ratios (SNR) using calibrated targets. Additionally, to further boost measurement throughput, the thesis explores parallelisation of scanning probes, using diffraction gratings to generate multiple simultaneous illumination spots, each independently detected and analysed.

1.4. THESIS OUTLINE

This dissertation is divided into different chapters as follows:

- **Chapter 2**: Coherent Fourier scatterometry: Theory. Discussion of the theory behind coherent Fourier scatterometry.
- **Chapter 3**: Practical limits to detectability. We define the important quantities influencing the performance of the system and quantify the effect on the system in terms of signal quality. These include the optical aberrations, input power, electronic detection bandwidth, and numerical aperture.
- **Chapter 4**: Multi-beam coherent Fourier scatterometry. The chapter details the design, implementation and performance of probe multiplexing in a CFS system. The approach uses a diffractive beam splitter to generate multiple probes to scan a sample surface with separate detection and acquisition channels corresponding to each probe. The scan speed improvement for a given area scales inversely with the number of probes.
- **Chapter 5**: Galvo-based coherent Fourier scatterometry. The chapter details the design and implementation of a galvo-based CFS system. The setup uses a galvo mirror to replace the piezo stage used for the fast axis. The mirror scans the beam before the objective and the sample moves along the slow axis. The setup is limited to movements along the slow axis.
- **Chapter 6**: Rotation-based coherent Fourier scatterometry. The chapter details the design and implementation of rotation-based CFS. The setup uses a rotation stage to rotate the sample continuously while the CFS scan head is mounted on a piezo stage to step along the radial direction.
- **Chapter 7**: Scanning using digital micromirror device. The chapter details the design using a digital micromirror device (DMD) for a fast multiplexed CFS setup. The key advantage of the design is that there are no moving parts and the sample can be kept fixed while the DMD mirrors are used to scan a beam across the sample.
- **Chapter 8**: Conclusions and outlook. The chapter includes the thesis summary and a discussion on the possible future work.

BIBLIOGRAPHY

[1] L. Versenyi, “Protagoras’ man-measure fragment”, *The American Journal of Philology*, vol. 83, no. 2, pp. 178–184, 1962, ISSN: 00029475, 10863168. [Online]. Available: `http://www.jstor.org/stable/292215`.

[2] R. O. Kaaronen, M. A. Manninen, and J. T. Eronen, “Body-based units of measure in cultural evolution”, *Science*, vol. 380, no. 6648, pp. 948–954, 2023. DOI: `https://doi.org/10.1126/science.adf1936`.

[3] M. H. Stone, “The cubit: A history and measurement commentary”, *Journal of Anthropology*, vol. 2014, no. 1, p. 489 757, 2014. DOI: `https://doi-org.tudelft.idm.oclc.org/10.1155/2014/489757`.

[4] F. Monnier, J. Petit, and C. Tardy, “The use of the ‘ceremonial’ cubit rod as a measuring tool. an explanation”, *The Journal of Ancient Egyptian Architecture*, vol. 1, pp. 1–9, 2016.

[5] P. D. Bièvre, “Learning lessons from ancient Egypt”, *Accreditation and Quality Assurance*, vol. 10, no. 7, pp. 325–326, 2005. DOI: `https://doi.org/10.1007/s00769-005-0010-y`.

[6] K. J. Hume, *A History of Engineering Metrology*. Mechanical Engineering Publications, 1980.

[7] A. A. Yetisgin, S. Cetinel, M. Zuvin, A. Kosar, and O. Kutlu, “Therapeutic nanoparticles and their targeted delivery applications”, *Molecules*, vol. 25, no. 9, 2020, ISSN: 1420-3049. DOI: `https://doi.org/10.3390/molecules25092193`.

[8] M. J. Mitchell, M. M. Billingsley, R. M. Haley, M. E. Wechsler, N. A. Peppas, and R. Langer, “Engineering precision nanoparticles for drug delivery”, *Nature Reviews Drug Discovery*, vol. 20, no. 2, pp. 101–24, 2021. DOI: `https://doi.org/10.1038/s41573-020-0090-8`.

[9] A. Bhat, S. Budholiya, S. A. Raj, *et al.*, “Review on nanocomposites based on aerospace applications”, *Nanotechnology Reviews*, vol. 10, no. 1, pp. 237–253, 2021. DOI: `https://doi.org/10.1515/ntrev-2021-0018`.

[10] M. Shafique and X. Luo, “Nanotechnology in transportation vehicles: An overview of its applications, environmental, health and safety concerns”, *Materials*, vol. 12, no. 15, 2019, ISSN: 1996-1944. DOI: `https://doi.org/10.3390/ma12152493`.

[11] A. L. M. Reddy, S. R. Gowda, M. M. Shaijumon, and P. M. Ajayan, “Hybrid nanostructures for energy storage applications”, *Advanced Materials*, vol. 24, no. 37, pp. 5045–5064, 2012. DOI: `https://doi.org/10.1002/adma.201104502`.

[12] F. Priolo, T. Gregorkiewicz, and T. F. Krauss, “Silicon nanostructures for photonics and photovoltaics”, *Nature Nanotechnology*, vol. 9, no. 1, pp. 19–32, 2014. DOI: `https://doi.org/10.1038/nnano.2013.271`.

[13] W. A. D. M. Jayathilaka, K. Qi, Y. Qin, *et al.*, “Significance of nanomaterials in wearables: A review on wearable actuators and sensors”, *Advanced Materials*, vol. 31, no. 7, p. 1 805 921, 2019. DOI: `https://doi.org/10.1002/adma.201805921`.

[14] T. Pyzdek and P. Keller, *Six Sigma Handbook*. McGraw-Hill Education, 2024.

[15] IEEE International Roadmap for Devices and Systems, “Metrology”, *Institute of Electrical and Electronics Engineers*, 2023. DOI: `https://doi.org/10.60627/FF6XD213`.

[16] M. A. Breton, D. Schmidt, A. Greene, *et al.*, “Nanosheet metrology opportunities for technology readiness”, in *Metrology, Inspection, and Process Control for Semiconductor Manufacturing XXXV*, O. Adan and J. C. Robinson, Eds., International Society for Optics and Photonics, vol. 11611, SPIE, 2021, 116111R. DOI: `10.1117/12.2583636`.

[17] P. Batude, M. Vinet, B. Previtali, *et al.*, “Advances, challenges and opportunities in 3D CMOS sequential integration”, in *2011 International Electron Devices Meeting*, 2011, pp. 7.3.1–7.3.4. DOI: `10.1109/IEDM.2011.6131506`.

[18] M. M. Shulaker, T. F. Wu, A. Pal, *et al.*, “Monolithic 3D integration of logic and memory: Carbon nanotube FETs, resistive RAM, and silicon FETs”, in *2014 IEEE International Electron Devices Meeting*, 2014, pp. 27.4.1–27.4.4. DOI: `10.1109/IEDM.2014.7047120`.

[19] S.-X. Guan, T. H. Yang, C.-H. Yang, *et al.*, “Monolithic 3D integration of back-end compatible 2D material FET on Si FinFET”, *npj 2D Materials and Applications*, vol. 7, no. 1, 2023. DOI: `10.1038/s41699-023-00371-7`.

[20] J. A. del Alamo, “Nanometre-scale electronics with III-V compound semiconductors”, *Nature*, vol. 479, no. 7373, pp. 317–323, 2011. DOI: `10.1038/nature10677`.

[21] M. C. Lemme, D. Akinwande, C. Huyghebaert, and C. Stampfer, “2D materials for future heterogeneous electronics”, *Nature Communications*, vol. 13, no. 1, 2022. DOI: `10.1038/s41467-022-29001-4`.

[22] M. Germain, F. Caputo, S. Metcalfe, *et al.*, “Delivering the power of nanomedicine to patients today”, *Journal of Controlled Release*, vol. 326, pp. 164–171, 2020, ISSN: 0168-3659. DOI: `https://doi.org/10.1016/j.jconrel.2020.07.007`.

[23] M. J. Nirmala, U. Kizhuveetil, A. Johnson, R. Nagarajan, V. Muthuvijayan, *et al.*, “Cancer nanomedicine: A review of nano-therapeutics and challenges ahead”, *RSC advances*, vol. 13, no. 13, pp. 8606–8629, 2023. DOI: `https://doi.org/10.1039/D2RA07863E`.

[24] X. Huang, N. Kong, X. Zhang, Y. Cao, R. Langer, and W. Tao, “The landscape of mRNA nanomedicine”, *Nature Medicine*, vol. 28, no. 11, pp. 2273–2287, 2022. DOI: `10.1038/s41591-022-02061-1`.

[25] J. Deumer, E. Andresen, C. Gollwitzer, R. Schürmann, and U. Resch-Genger, "Adding more shape to nanoscale reference materials-LiYF4: Yb, Tm bipyramids as standards for sizing methods and particle number concentration", *Analytical Chemistry*, vol. 96, no. 48, pp. 19 004–19 011, 2024. DOI: https://doi.org/10.1021/acs.analchem.4c03641.

[26] J. D. Clogston, V. A. Hackley, A. Prina-Mello, S. Puri, S. Sonzini, and P. L. Soo, "Sizing up the next generation of nanomedicines", *Pharmaceutical Research*, vol. 37, no. 1, 2019. DOI: https://doi.org/10.1007/s11095-019-2736-y.

[27] B. Halamoda-Kenzaoui, S. Baconnier, T. Bastogne, *et al.*, "Bridging communities in the field of nanomedicine", *Regulatory Toxicology and Pharmacology*, vol. 106, pp. 187–196, 2019, ISSN: 0273-2300. DOI: https://doi.org/10.1016/j.yrtph.2019.04.011.

[28] J. Parot, F. Caputo, D. Mehn, V. Hackley, and L. Calzolai, "Physical characterization of liposomal drug formulations using multi-detector asymmetrical-flow field flow fractionation", *Journal of Controlled Release*, vol. 320, pp. 495–510, 2020, ISSN: 0168-3659. DOI: https://doi.org/10.1016/j.jconrel.2020.01.049.

[29] F. Caputo, G. Favre, G. Borchard, *et al.*, "Toward an international standardisation roadmap for nanomedicine", *Drug Delivery and Translational Research*, vol. 14, no. 9, pp. 2578–2588, 2024. DOI: https://doi.org/10.1007/s13346-024-01646-2.

[30] D. J. Whitehouse, *Handbook of surface metrology*. Routledge, 2023.

[31] G. Binnig, C. F. Quate, and C. Gerber, "Atomic force microscope", *Phys. Rev. Lett.*, vol. 56, pp. 930–933, 9 1986. DOI: 10.1103/PhysRevLett.56.930.

[32] A. Yacoot and L. Koenders, "Recent developments in dimensional nanometrology using AFMs", *Measurement Science and Technology*, vol. 22, no. 12, p. 122 001, 2011. DOI: https://doi.org/10.1088/0957-0233/22/12/122001.

[33] M. Kopycinska-Müller, R. H. Geiss, and D. C. Hurley, "Contact mechanics and tip shape in AFM-based nanomechanical measurements", *Ultramicroscopy*, vol. 106, no. 6, pp. 466–474, 2006, ISSN: 0304-3991. DOI: https://doi.org/10.1016/j.ultramic.2005.12.006.

[34] T. Strahlendorff, G. Dai, D. Bergmann, and R. Tutsch, "Tip wear and tip breakage in high-speed atomic force microscopes", *Ultramicroscopy*, vol. 201, pp. 28–37, 2019, ISSN: 0304-3991. DOI: https://doi.org/10.1016/j.ultramic.2019.03.013.

[35] W. Häßler-Grohne, D. Hüser, K.-P. Johnsen, C. G. Frase, and H. Bosse, "Current limitations of SEM and AFM metrology for the characterization of 3d nanostructures", *Measurement Science and Technology*, vol. 22, no. 9, p. 094 003, 2011. DOI: 10.1088/0957-0233/22/9/094003.

[36] A. A. Tseng, "Advancements and challenges in development of atomic force microscopy for nanofabrication", *Nano Today*, vol. 6, no. 5, pp. 493–509, 2011, ISSN: 1748-0132. DOI: https://doi.org/10.1016/j.nantod.2011.08.003.

[37] K. Nakamae, "Electron microscopy in semiconductor inspection", *Measurement Science and Technology*, vol. 32, no. 5, p. 052 003, 2021. DOI: `https://doi.org/10.1088/1361-6501/abd96d`.

[38] B. Inkson, "2 - Scanning electron microscopy (SEM) and transmission electron microscopy (TEM) for materials characterization", in *Materials Characterization Using Nondestructive Evaluation (NDE) Methods*, G. Hübschen, I. Altpeter, R. Tschuncky, and H.-G. Herrmann, Eds., Woodhead Publishing, 2016, pp. 17–43, ISBN: 978-0-08-100040-3. DOI: `https://doi.org/10.1016/B978-0-08-100040-3.00002-X`.

[39] M. T. Postek, "Critical issues in scanning electron microscope metrology", *Journal of research of the National Institute of Standards and Technology*, vol. 99, no. 5, p. 641, 1994. DOI: `https://doi.org/10.6028/jres.099.059`.

[40] Y. Mitsui, T. Sunaoshi, and J. Lee, "A study of electrical characteristic changes in mosfet by electron beam irradiation", *Microelectronics Reliability*, vol. 49, pp. 1182–1187, Sep. 2009. DOI: `10.1016/j.microrel.2009.07.019`.

[41] R. Nandakumar, P. B. P. Bhattacharya, and G. K. G. Kousik, "Study of scanning electron microscope irradiated damage to gate oxides of metal oxide semiconductor field effect transistors", *Japanese journal of applied physics*, vol. 31, no. 9R, p. 2651, 1992. DOI: `https://doi.org/10.1143/JJAP.31.2651`.

[42] R. B. Bergmann, M. Kalms, and C. Falldorf, "Optical in-process measurement: Concepts for precise, fast and robust optical metrology for complex measurement situations", *Applied Sciences*, vol. 11, no. 22, 2021, ISSN: 2076-3417. DOI: `https://doi.org/10.3390/app112210533`.

[43] W. Osten, "Optical metrology: The long and unstoppable way to become an outstanding measuring tool", in *Speckle 2018: VII International Conference on Speckle Metrology*, SPIE, vol. 10834, 2018, p. 1 083 402. DOI: `https://doi.org/10.1117/12.2322533`.

[44] Y. Shimizu, L.-C. Chen, D. W. Kim, X. Chen, X. Li, and H. Matsukuma, "An insight into optical metrology in manufacturing", *Measurement Science and Technology*, vol. 32, no. 4, p. 042 003, 2021. DOI: `https://doi.org/10.1088/1361-6501/abc578`.

[45] P. J. De Groot, "A review of selected topics in interferometric optical metrology", *Reports on Progress in Physics*, vol. 82, no. 5, p. 056 101, 2019. DOI: `https://doi.org/10.1088/1361-6633/ab092d`.

[46] D. Hamilton and T. Wilson, "Three-dimensional surface measurement using the confocal scanning microscope", *Applied Physics B*, vol. 27, pp. 211–213, 1982. DOI: `https://doi.org/10.1007/BF00697444`.

[47] D. Pohl, "Scanning near-field optical microscopy (SNOM)", in *Advances in optical and electron microscopy*, vol. 12, Elsevier, 1991, pp. 243–312. DOI: `https://doi.org/10.1016/B978-0-12-029912-6.50009-9`.

[48] R. S. Sirohi, *Speckle metrology*. CRC Press, 2020.

[49] M. H. Madsen and P.-E. Hansen, “Scatterometry—fast and robust measurements of nano-textured surfaces”, *Surface Topography: Metrology and Properties*, vol. 4, no. 2, p. 023 003, 2016. DOI: https://doi.org/10.1088/2051-672X/4/2/023003.

[50] J. Xu and S. Zhang, “Status, challenges, and future perspectives of fringe projection profilometry”, *Optics and Lasers in Engineering*, vol. 135, p. 106 193, 2020. DOI: https://doi.org/10.1016/j.optlaseng.2020.106193.

[51] A. C. Diebold, A. Antonelli, and N. Keller, “Perspective: Optical measurement of feature dimensions and shapes by scatterometry”, *APL Materials*, vol. 6, no. 5, p. 058 201, 2018, ISSN: 2166-532X. DOI: https://doi.org/10.1063/1.5018310.

[52] C. J. Raymond, M. E. Littau, A. Chuprin, and S. Ward, “Comparison of solutions to the scatterometry inverse problem”, in *Metrology, Inspection, and Process Control for Microlithography XVIII*, SPIE, vol. 5375, 2004, pp. 564–575. DOI: https://doi.org/10.1117/12.538662.

[53] H.-T. Huang and F. L. Terry Jr, “Spectroscopic ellipsometry and reflectometry from gratings (scatterometry) for critical dimension measurement and in situ, real-time process monitoring”, *Thin Solid Films*, vol. 455-456, pp. 828–836, 2004, The 3rd International Conference on Spectroscopic Ellipsometry, ISSN: 0040-6090. DOI: https://doi.org/10.1016/j.tsf.2004.04.010.

[54] A. Fernández Herrero, F. Scholze, and G. e. a. Dai, “Analysis of line-edge roughness using EUV scatterometry”, *Nanomanuf Metrol*, vol. 5, pp. 149–58, 2022. DOI: https://doi.org/10.1007/s41871-022-00126-w.

[55] X. Dou, S. F. Pereira, C. Min, *et al.*, “Determination of steep sidewall angle using polarization-sensitive asymmetric scattering”, *Measurement Science and Technology*, vol. 32, no. 8, p. 085 201, 2021. DOI: https://doi.org/10.1088/1361-6501/abfbac.

[56] H. Fujiwara, *Spectroscopic ellipsometry: principles and applications.* John Wiley & Sons, 2007. DOI: https://doi.org/10.1002/9780470060193.

[57] J. C. Stover, “Optical scattering”, *SPIE optical engineering press, Bellingham*, vol. 1, 1995. DOI: https://doi.org/10.1117/3.203079.

[58] X. Niu, N. Jakatdar, J. Bao, and C. J. Spanos, “Specular spectroscopic scatterometry”, *IEEE Transactions on Semiconductor Manufacturing*, vol. 14, no. 2, pp. 97–111, 2001. DOI: https://doi.org/10.1109/66.920722.

[59] S. Roy, A. C. Assafrao, S. F. Pereira, and H. P. Urbach, “Coherent Fourier scatterometry for detection of nanometer-sized particles on a planar substrate surface”, *Opt. Express*, vol. 22, no. 11, pp. 13 250–13 262, 2014. DOI: https://doi.org/10.1364/OE.22.013250.

[60] S. Roy, M. Bouwens, L. Wei, S. F. Pereira, H. P. Urbach, and P. van der Walle, “High speed low power optical detection of sub-wavelength scatterer”, *Review of Scientific Instruments*, vol. 86, no. 12, p. 123 111, 2015, ISSN: 0034-6748. DOI: https://doi.org/10.1063/1.4938183.

[61] N. Kumar, P. Petrik, G. K. P. Ramanandan, *et al.*, "Reconstruction of sub-wavelength features and nano-positioning of gratings using coherent Fourier scatterometry", *Opt. Express*, vol. 22, no. 20, pp. 24 678–24 688, 2014. DOI: `https://doi.org/10.1364/OE.22.024678`.

[62] J. Rafighdoost, D. Kolenov, and S. F. Pereira, "Coherent Fourier scatterometry for detection of killer defects on Silicon Carbide samples", *IEEE Transactions on Semiconductor Manufacturing*, vol. 37, no. 1, pp. 124–128, 2024. DOI: `https://doi.org/10.1109/TSM.2023.3337720`.

[63] M. Menzel and S. F. Pereira, "Coherent Fourier scatterometry reveals nerve fiber crossings in the brain", *Biomed. Opt. Express*, vol. 11, no. 8, pp. 4735–4758, 2020. DOI: `https://doi.org/10.1364/BOE.397604`.

[64] A. Paul, R. Wever, S. Soman, and S. Pereira, "Utilizing focused field as a probe for shape determination of subwavelength structures via coherent Fourier scatterometry", English, *Physical Review Applied*, vol. 23, no. 2, 2025, ISSN: 2331-7019. DOI: `10.1103/PhysRevApplied.23.024016`.

[65] Y. K. Yong, S. O. R. Moheimani, B. J. Kenton, and K. K. Leang, "Invited review article: High-speed flexure-guided nanopositioning: Mechanical design and control issues", *Review of Scientific Instruments*, vol. 83, no. 12, p. 121 101, Dec. 2012, ISSN: 0034-6748. DOI: `https://doi.org/10.1063/1.4765048`.

[66] T. Ando, N. Kodera, E. Takai, D. Maruyama, K. Saito, and A. Toda, "A high-speed atomic force microscope for studying biological macromolecules", *Proceedings of the National Academy of Sciences*, vol. 98, no. 22, pp. 12 468–12 472, 2001. DOI: `10.1073/pnas.211400898`.

[67] R. Lane, Y. Vos, A. H. Wolters, *et al.*, "Optimization of negative stage bias potential for faster imaging in large-scale electron microscopy", *Journal of Structural Biology: X*, vol. 5, p. 100 046, 2021, ISSN: 2590-1524. DOI: `https://doi.org/10.1016/j.yjsbx.2021.100046`.

[68] TNO, 2011. [Online]. Available: `https://www.tno.nl/publish/pages/7808/tno-leaflet-rapid-nano-particle-scanner.pdf`.

[69] I. Veilleux, J. A. Spencer, D. P. Biss, D. Cote, and C. P. Lin, "In vivo cell tracking with video rate multimodality laser scanning microscopy", *IEEE Journal of Selected Topics in Quantum Electronics*, vol. 14, no. 1, pp. 10–18, 2008. DOI: `https://doi.org/10.1109/JSTQE.2007.912751`.

[70] A. Paul, M. Boonstra, and S. F. Pereira, "Near-infrared coherent fourier scatterometry for deep subsurface nanostructure metrology in silicon", *Optics and Lasers in Engineering*, vol. 195, p. 109 354, 2025. DOI: `10.1016/j.optlaseng.2025.109354`.

[71] D. Kolenov, D. Davidse, J. Le Cam, and S. Pereira, "Convolutional neural network applied for nanoparticle classification using coherent scatterometry data", *Applied Optics*, vol. 59, no. 27, pp. 8426–8433, 2020. DOI: `https://doi.org/10.1364/AO.399894`.

[72] B. J. Kenton and K. K. Leang, “Design and control of a three-axis serial-kinematic high-bandwidth nanopositioner”, *IEEE/ASME Transactions on Mechatronics*, vol. 17, no. 2, pp. 356–369, 2011. DOI: https://doi.org/10.1109/TMECH.2011.2105499.

[73] K. K. Leang and A. J. Fleming, “High-speed serial-kinematic AFM scanner: Design and drive considerations”, in *2008 American control conference*, IEEE, 2008, pp. 3188–3193. DOI: https://doi.org/10.1109/ACC.2008.4586983.

[74] F. Chen, Q. Zhang, Y. Gao, and W. Dong, “A review on the flexure-based displacement amplification mechanisms”, *IEEE Access*, vol. 8, pp. 205 919–205 937, 2020. DOI: https://doi.org/10.1109/ACCESS.2020.3037827.

[75] J. Montagu, *Handbook of optical and laser scanning*. CRC Press Boca Raton, FL, USA, 2016, ch. Galvanometric and resonant scanners, pp. 418–473. DOI: https://doi.org/10.1201/9781315218243.

[76] R. Ying, Y. Cui, J. Huang, D. Liang, and Y. Wang, “Precise measurement of surface topography with microstructures based on differential confocal and spiral scanning”, *Measurement*, vol. 184, p. 110 004, 2021, ISSN: 0263-2241. DOI: https://doi.org/10.1016/j.measurement.2021.110004.

[77] A. Ulčinas and Š. Vaitekonis, “Rotational scanning atomic force microscopy.”, *Nanotechnology*, vol. 28, no. 10, 10LT02, 2017. DOI: https://doi.org/10.1088/1361-6528/aa5af7.

[78] G. D. Reddy and P. Saggau, “Fast three-dimensional laser scanning scheme using acousto-optic deflectors”, *Journal of biomedical optics*, vol. 10, no. 6, pp. 064 038–064 038, 2005. DOI: https://doi.org/10.1117/1.2141504.

[79] Q. Lin, S. Fang, Y. Yu, *et al.*, “Optical multi-beam steering and communication using integrated acousto-optics arrays”, *Nature Communications*, vol. 16, no. 1, pp. 1–7, 2025. DOI: https://doi.org/10.1038/s41467-025-59831-x.

[80] V.-F. Duma and A. G. Podoleanu, “Polygon mirror scanners in biomedical imaging: A review”, *Optical Components and Materials X*, vol. 8621, pp. 175–183, 2013. DOI: https://doi.org/10.1117/12.2005065.

[81] D. R. Gozzard, L. E. Roberts, J. T. Spollard, P. G. Sibley, and D. A. Shaddock, “Fast beam steering with an optical phased array”, *Optics Letters*, vol. 45, no. 13, pp. 3793–3796, 2020. DOI: https://doi.org/10.1364/OL.393007.

[82] D. Dudley, W. M. Duncan, and J. Slaughter, “Emerging digital micromirror device (DMD) applications”, in *MOEMS display and imaging systems*, SPIE, vol. 4985, 2003, pp. 14–25. DOI: https://doi.org/10.1117/12.480761.

2

COHERENT FOURIER SCATTEROMETRY: THEORY

This chapter develops the theoretical foundations of coherent Fourier scatterometry (CFS), from the formation of the tightly focused probe to the modelling of its interaction with the sample and the subsequent scanning-based detection. We first describe the focal field using scalar diffraction theory for low-NA systems and a vectorial Richards–Wolf formalism for high-NA objectives, establishing analytical expressions for the probe intensity and phase distributions. Building on this, we outline forward modelling approaches based on finite-difference time-domain (FDTD) and rigorous coupled-wave analysis (RCWA) to compute the scattered field in the Fourier plane, and discuss how scanning the focused spot and recording the angle-resolved response enables construction of spatially resolved scattering maps for parameter retrieval via inverse modelling.

Coherent Fourier scatterometry (CFS) is an optical metrology technique designed for the non-destructive, high-resolution characterisation of surfaces. Its primary function is to infer the optical and/or geometric properties of a sample by analysing the light scattered from it. Unlike classical scatterometric approaches, which sequentially measure the angular response from a sample by varying either the incident or reflected angles or both within a predetermined range, CFS captures the full angular response simultaneously [1], [2]. A general schematic representation of the complete CFS workflow is provided in Figure 2.1.

The experimental implementation of CFS uses an objective lens for the simultaneous angular measurement. The lens focuses a coherent beam of light to a diffraction-limited spot, creating a highly localised optical probe to interact with the sample. It also collects the light scattered or reflected from the sample and projects it onto a detector placed either directly in the back focal plane (BFP) of the objective lens or using optical relays. This BFP is also known as the Fourier plane because, under the scalar Fresnel diffraction approximation, the objective lens performs a physical Fourier transform, establishing a direct mapping between a spatial position in this plane and a unique plane wave propagation angle [3]. The resulting intensity pattern in the BFP thus represents an angle-resolved "fingerprint" of the sample topography.

The geometric parameters of the sample are extracted from the measurement data by solving an inverse problem. The measured Fourier field is compared against a pre-computed library of fields corresponding to known sample geometries, obtained using an appropriate forward model. The model simulates the interaction between the focused spot and the scattering object by numerically solving the Maxwell equations. The accuracy of the inference depends upon the accuracy of the forward model, requiring precise characterisation of the focused spot and sufficient *a priori* information about the sample properties.

The logical starting point for a theoretical description of CFS is the optical probe itself. For systems employing low numerical aperture (NA) objectives, scalar diffraction theory provides a sufficiently accurate description of the focal field, as detailed in section 2.1. This approach can provide first-order estimates of the scanning parameters such as the spot size and depth of focus, which are key factors to consider while building a system. However, for objectives with higher NA, scalar approximations become invalid due to significant polarisation-dependent effects and the emergence of longitudinal electric field components. Consequently, vectorial diffraction theory is required for rigorous analysis. The vectorial model presented in section 2.2 follows the Richards-Wolf formalism and can provide analytical expressions for describing the focal field distribution for arbitrarily polarised beams.

With a precise description of the optical probe established, the next step is to understand its interaction with the sample. Details of two common modelling approaches are outlined briefly in section 2.3. Lastly, to achieve spatially resolved measurements across the entire sample, the focused spot is scanned over its surface. The Fourier field for each spot position is recorded and stitched together to form a scattering map of the sample. The details of the detection schemes and the detection bandwidth requirements are described in section 2.4.

Together, these sections on the probe, the forward model, and the scanning provide

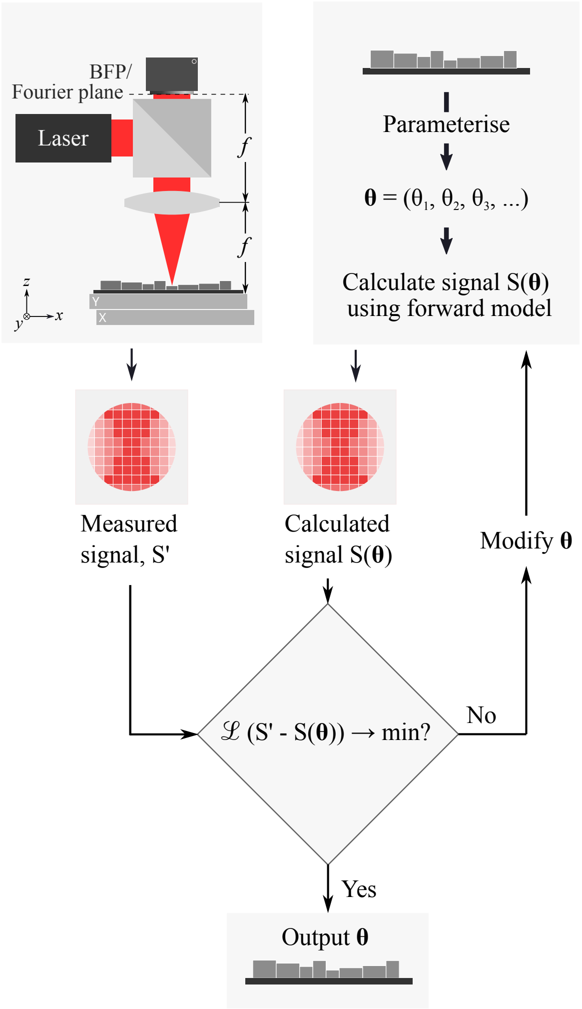

Figure 2.1: General workflow of coherent Fourier scatterometry (CFS). Light scattered from the sample under test is collected by an objective lens and measured in the back focal plane (BFP), where the angular scattering response is encoded in the field distribution. The measured signal is compared against a library of simulated responses generated from parameterised models of the sample. The set of parameters that yields the best agreement between measured and simulated signals is obtained as the reconstructed description of the sample.

building blocks for understanding and analysing the CFS systems discussed later in this work. The details are not meant to be exhaustive but provide a brief introduction to each component.

2.1. FOCUS SPOT: SCALAR

Scalar diffraction theory provides an effective method for describing the focal field distribution in optical systems without taking polarisation effects into account. Using the Fresnel approximation and the lens approximated as a quadratic phase object, the field distribution in the focal plane is proportional to the two-dimensional Fourier transform of the incident field [3].

Consider the propagation of light through a lens shown in Figure 2.2. Assuming an input field with uniform intensity that fully covers the lens aperture of radius w, the input field in the BFP can be represented by $\mathrm{circ}\left(\frac{q}{w}\right)$, where q is the radial coordinate in the BFP. If the focal length of the lens is f and the wavelength of the incident field is λ, the field distribution in the front focal plane (FFP) is given by:

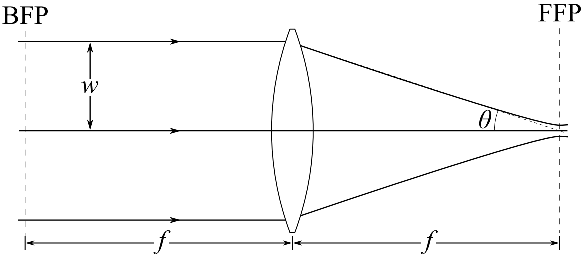

Figure 2.2: Schematic illustrating the focusing of a collimated light beam through a lens of focal length f. BFP: back focal plane, FFP: front focal plane.

$$U(r) = 2\mathrm{e}^{\mathrm{i}kf}\,\mathrm{e}^{\frac{\mathrm{i}kr^2}{2f}}\,\frac{\pi w^2}{\mathrm{i}\lambda f}\,\frac{J_1\left(\frac{kwr}{f}\right)}{\frac{kwr}{f}}, \tag{2.1}$$

where, $k = 2\pi/\lambda$, and r is the radial coordinate in the focal plane. The corresponding intensity distribution is calculated as:

$$I(r) = 4\left(\frac{\pi w^2}{\lambda f}\right)^2\left[\frac{J_1\left(\frac{kwr}{f}\right)}{\frac{kwr}{f}}\right]^2. \tag{2.2}$$

This intensity distribution is known as the Airy pattern. It is circularly symmetric, featuring a central bright lobe and concentric rings around it. The diameter of the central lobe, defining the diffraction-limited resolution, is given by:

$$d = \frac{1.22\lambda f}{w} = \frac{1.22\lambda}{\mathrm{NA}}, \tag{2.3}$$

where, NA = $\sin\theta$, under the small-angle approximation, $\tan\theta \approx \theta \approx \sin\theta$. The above derivation assumes an incident field with uniform intensity and constant phase. However, the method remains consistent for any general scalar incident field. In the following section, a more rigorous vectorial approach to compute the focal field distribution is presented.

2.2. FOCUS SPOT: VECTORIAL

In this section, a more realistic model for the transformation by the lens is detailed, following the formulation described in Novotny and Hecht [4]. Let us consider an aplanatic lens as the focusing element. The focusing due to an aplanatic lens is governed by two rules: the sine condition and the intensity law.

The sine condition dictates the refraction of optical rays at the aplanatic optical element. For a lens of focal length f, the sine condition states that each optical ray which emerges or converges to the focus of the aplanatic lens must intersect with its conjugate ray (ray parallel to optical axis) on a sphere (reference sphere) of radius f. The intensity law ensures that the total energy incident on the lens remains the same before and after refraction. If $\mathbf{E}_1$ is the electric field before refraction, the field after refraction, $\mathbf{E}_2$, must fulfill,

$$|\mathbf{E}_2| = |\mathbf{E}_1|\sqrt{\frac{n_1}{n_2}}\cos^{1/2}\theta, \tag{2.4}$$

to satisfy the energy conservation, with $n_1 = n_2 = 1$ assuming the optical system to be surrounded by air. The relation assumes the magnetic permeability of the medium before and after refraction at optical frequency to be equal to 1.

Coordinate systems at various planes are defined as illustrated in Figure 2.3. An arbitrary point on the reference sphere is described by Cartesian coordinates $(x_\infty, y_\infty, z_\infty)$ or spherical coordinates (f, θ, φ), while points near the focus are represented by (x, y, z). During refraction at the reference sphere, an incident cylindrical coordinate system with unit vectors $(\mathbf{n}_\rho, \mathbf{n}_\varphi)$ is transformed into a spherical coordinate system with unit vectors $(\mathbf{n}_\theta, \mathbf{n}_\varphi)$. These unit vectors relate to Cartesian unit vectors $(\mathbf{n}_x, \mathbf{n}_y, \mathbf{n}_z)$ as:

$$\mathbf{n}_\rho = \cos\varphi\,\mathbf{n}_x + \sin\varphi\,\mathbf{n}_y, \tag{2.5}$$

$$\mathbf{n}_\varphi = -\sin\varphi\,\mathbf{n}_x + \cos\varphi\,\mathbf{n}_y, \tag{2.6}$$

$$\mathbf{n}_\theta = \cos\theta\,\cos\varphi\,\mathbf{n}_x + \cos\theta\sin\varphi\,\mathbf{n}_y - \sin\theta\,\mathbf{n}_z. \tag{2.7}$$

Let $\mathbf{E}_\mathrm{i}$ be the incident field. Following the cylindrical coordinate system, the incident field can be divided into two polarisations $\mathbf{E}_\mathrm{i}^\mathrm{s}$ and $\mathbf{E}_\mathrm{i}^\mathrm{p}$ defined along the azimuthal $\mathbf{n}_\varphi$ and radial $\mathbf{n}_\rho$ directions respectively:

$$\mathbf{E}_\mathrm{i}^\mathrm{s} = (\mathbf{E}_\mathrm{i}\cdot\mathbf{n}_\varphi)\,\mathbf{n}_\varphi \tag{2.8}$$

$$\mathbf{E}_\mathrm{i}^\mathrm{p} = (\mathbf{E}_\mathrm{i}\cdot\mathbf{n}_\rho)\,\mathbf{n}_\rho. \tag{2.9}$$

After refraction, the azimuthal vector $\mathbf{n}_\varphi$ remains the same while the radial vector $\mathbf{n}_\rho$ gets mapped into $\mathbf{n}_\theta$. The total refracted field following the two conditions is given by:

$$\mathbf{E}_\infty(\theta, \varphi) = \left[(\mathbf{E}_\mathrm{i}\cdot\mathbf{n}_\varphi)\,\mathbf{n}_\varphi + (\mathbf{E}_\mathrm{i}\cdot\mathbf{n}_\rho)\,\mathbf{n}_\theta\right]\cos^{1/2}\theta \tag{2.10}$$

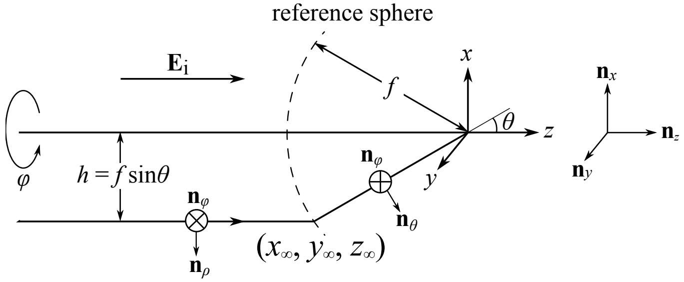

Figure 2.3: Schematic illustrating the focusing through an aplanatic lens of focal length f.

The field in the focal plane is calculated by propagating the refracted field to the focal plane using the angular spectrum method:

$$\mathbf{E}(x, y) = \frac{\mathrm{i} f \mathrm{e}^{-\mathrm{i}kf}}{2\pi} \iint_{(k_x^2+k_y^2)\leq k^2} \mathbf{E}_\infty(k_x, k_y, k_z) \mathrm{e}^{\mathrm{i}(k_x x + k_y y)} \frac{1}{k_z} \mathrm{d}k_x \mathrm{d}k_y. \tag{2.11}$$

The field at the reference sphere is expressed in terms of the spatial frequencies (k_x, k_y, k_z), where,

$$k_x = k \sin\theta \cos\varphi, \tag{2.12}$$

$$k_y = k \sin\theta \sin\varphi, \qquad 0 \leq \theta \leq \theta_\mathrm{max}, 0 \leq \varphi \leq 2\pi, \tag{2.13}$$

$$k_z = k \cos\theta, \tag{2.14}$$

θ_max is determined by the finite aperture size of the lens, with NA = $\sin\theta_\mathrm{max}$, assuming the refractive index of the lens surrounding medium to be 1. Figure 2.4 shows the amplitude and phase distributions of the electric field in the focal plane for an input field linearly polarised along the x-axis and having a wavelength of 633 nm. The NA of the system is 0.4.

Having established the structure of the focused field, we now turn our attention to the forward modelling process that simulates the interaction of this focal field with the sample.

2.3. FORWARD MODEL

To retrieve the sample parameters, it is essential to have an accurate model of the interaction between the sample and the focused spot. For a small range of samples such as periodic gratings or spherical particles on a surface, under some conditions, this can be calculated analytically [5], [6]. However, for more complex samples, different numerical modelling techniques need to be used. In this section, we detail two methods commonly used in CFS: finite-difference time-domain (FDTD) method and rigorous coupled-wave analysis (RCWA).

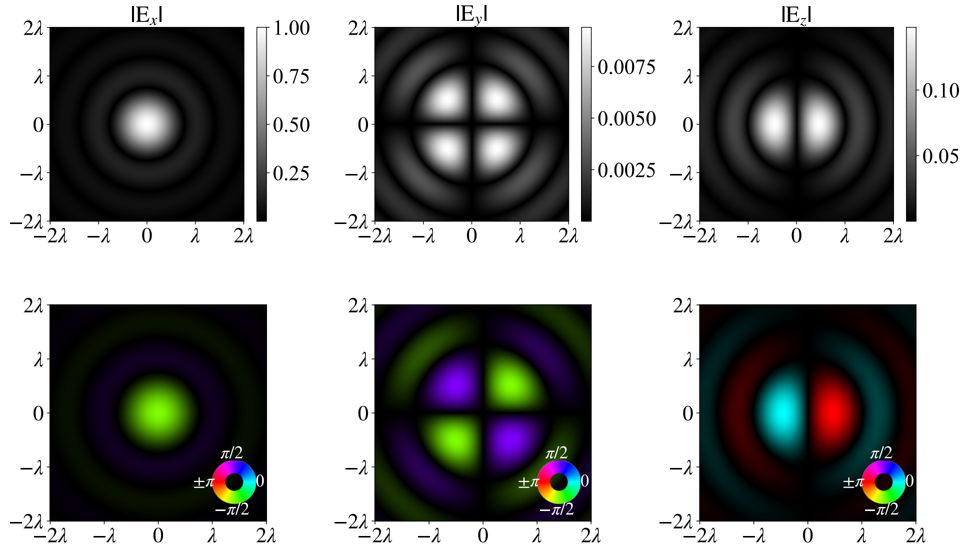

Figure 2.4: Amplitude and phase distributions of the electric field components at the focal plane: E_x (left), E_y (center), E_z (right). The simulations used an NA of 0.4, wavelength of 633 nm and input field linearly polarised along x-axis.

2.3.1. FDTD

The FDTD method is a numerical technique that directly solves the Maxwell curl equations by discretising both space and time on a staggered grid known as the Yee cell [7]. It updates electric and magnetic fields using central-difference approximations, enabling stable propagation of electromagnetic waves within a defined computational domain. In scatterometry applications, FDTD is particularly effective due to its ability to model complex interactions of incident electromagnetic waves with scatterers of arbitrary shapes and material properties.

The simulation region including the sample structure is discretised using a fine mesh and the electromagnetic fields are calculated at every point on the mesh. The material properties such as the permittivity, permeability and conductivity of each cell must also be defined. Additionally, to prevent artificial reflections from the simulation region boundaries, absorbing boundary conditions are essential. The perfectly matched layer (PML) boundary condition is widely used for this purpose due to its effectiveness [8]. It achieves near-perfect absorption of outgoing electromagnetic waves, regardless of their frequency, angle of incidence, or polarization. The PML accomplishes this by gradually matching the wave impedance of free space, causing minimal reflection and exponential decay of waves within a relatively thin layer of computational cells.

The scattered field resulting from the interaction of the probe with the surface is recorded using a two-dimensional monitor placed above the sample. Once the field on a surface is known, near-to-far field transformations can be used to calculate the field anywhere beyond that surface [7]. In this work, the commercial FDTD software Lumerical is used to compute the scattered field in the Fourier plane using the in-built near-to-far field transformation functions.

2.3.2. RCWA

RCWA is a semi-analytic method used to simulate diffraction from periodic structures [9], [10]. First, a unit cell of the repeating structure is defined. The cell can have inhomogeneities along the x- and y-directions but is assumed to be homogeneous along the z. The x- and y-directions lie in the plane of the sample surface, while the z-direction is normal to this plane. Complex structures are modelled by dividing them into thin layers (slabs) along the z-axis. The number of slabs required depends on the complexity of the structure. RCWA then solves the diffraction problem by solving the wave equation within each layer and matching the appropriate field components across interfaces at the boundary between layers to calculate the diffraction due to the complete structure.

Once a forward model is computed for a given set of sample parameters, the inverse problem consists of determining which parameters best reproduce the experimentally measured data. This typically involves comparing measured Fourier plane fields with simulated results and minimising a cost function that quantifies the mismatch. Solving the inverse problem may use direct optimisation algorithms, library search methods, or neural networks depending on the complexity and dimensionality of the parameter space [11]–[14].

To acquire spatially resolved information over the entire sample, the probe must be scanned across the surface. This introduces the next step in the CFS process.

2.4. SCANNING

So far we have described the focused spot probe as well as the interaction of the probe with different samples. The remaining component is the process of scanning. In addition to enabling large-area measurements, scanning provides a distinct advantage in improving the sensitivity for parameter retrieval of periodic structures such as gratings [15]–[17]. The gain stems from the coherent nature of the incident beam, enabling the CFS measurements to benefit from the phase information encoded in the scattered field. For diffraction gratings, as the spot scans across the surface, a constant phase shift is added to all non-zero diffraction orders. This phase shift is directly proportional to the lateral displacement of the spot relative to the grating:

$$\tilde{\mathbf{R}}_m = \mathbf{R}_m \mathrm{e}^{\left(\mathrm{i}2\pi \frac{m\Delta x}{\Lambda}\right)}, \tag{2.15}$$

where, $\mathbf{R}_m$ is the complex amplitude of the m^{th} diffraction order when the focused spot is centred with respect to the grating unit cell, and $\tilde{\mathbf{R}}_m$ is the corresponding amplitude when the spot is laterally displaced by Δx, Λ denotes the grating period. This additional phase alters the interference between diffraction orders, leading to measurable changes in the intensity distribution observed in the Fourier plane.

Figure 2.5 shows the simulated intensity distributions in the Fourier plane of a diffraction grating sample using RCWA. The grating has a period of 1200 nm, with 50% duty cycle, 150 nm height and 90° side-wall angles. The different intensity distributions correspond to different focus spot positions on the grating. The incident field is a 0.4 NA focus spot with a wavelength of 633 nm, polarised along the x-axis in the pupil

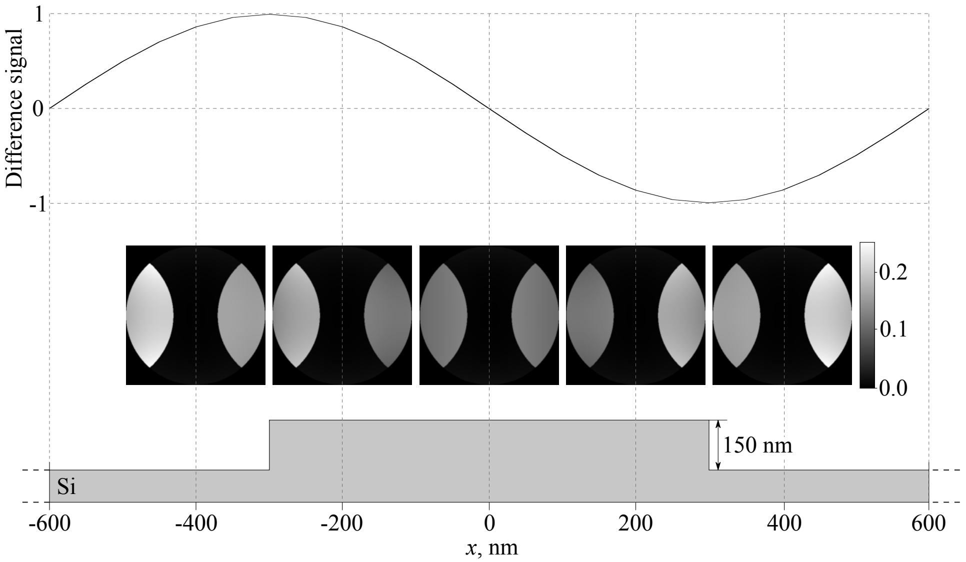

Figure 2.5: Schematic of the signal generation while scanning a grating. Bottom: the simulated Si grating with 1200 nm period, 600 nm critical dimension, 150 nm height, 90° side-wall angles. Middle: Fourier field intensity distributions while scanning a diffraction grating within one period. Top: The difference signal generated from the asymmetry in the Fourier plane intensities as a function of the spot position. The simulated incident field is a 0.4 NA focused spot with 633 nm wavelength, polarised along the x-axis in the pupil plane perpendicular to the grating lines.

plane, perpendicular to the grating lines. The changes in the Fourier field intensities are due to constructive or destructive interference between the complex amplitudes of the different diffracted orders due to the relative phase shifts.

The far field distributions when scanning an isolated sub-wavelength structure along the x-direction are shown in Figure 2.6. The distributions were calculated using a commercial FDTD-based solver, Lumerical. The structure consists of a pit of 150 nm depth and 500 nm diameter, etched in Si. The incident field consists of a 0.4 NA focus spot having a wavelength of 633 nm, polarised along the x-axis. The intensity distribution has distinct lobes along the x-axis, parallel to the polarisation direction. As the spot scans across the structure, the intensity distribution becomes asymmetric but the changes occur mainly near the edges of the pupil. The pattern asymmetry can be exploited using a differential detection scheme to improve the detection sensitivity, as is shown in the next section.

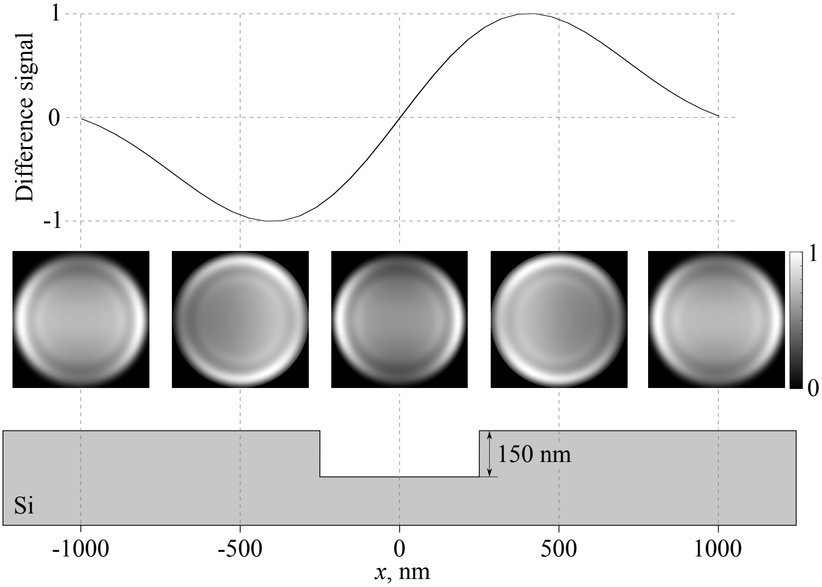

Figure 2.6: Schematic of the signal generation while scanning an isolated sub-wavelength structure. Bottom: The schematic of the structure consisting of a pit of 500 nm diameter and 150 nm depth etched in Si. Middle: Fourier field intensity distributions generated while scanning. Top: The difference signal generated from the asymmetry in the Fourier plane intensities as a function of the spot position. The simulated incident field is a 0.4 NA focused spot with 633 nm wavelength, polarised along the x-axis.

2.4.1. DIFFERENTIAL DETECTION

In certain applications, such as wafer contamination detection, the objective is to rapidly inspect large areas to identify the presence, size, and distribution of contaminants. In such cases, capturing the full Fourier field intensity at each scan position is unnecessary and can significantly slow down the inspection process. This is because full-field measurements typically require a CCD camera, which operates at limited frame rates.

A better alternative is to use a photodiode-based detection system, which offers higher bandwidth compared to conventional CCD cameras. Further improvement is made using a two-pixel differential detection scheme. In this configuration, the beam is centered on a bi-cell photodiode, and the detector measures the intensity difference between the two halves. A schematic of the detection system is shown in Figure 2.7. This scheme exploits the asymmetry in the Fourier plane intensity that appears while scanning and generates a non-zero signal only in the presence of a scatterer such as a particle contaminant. Additionally, the differential detection suppresses common-mode noise such as stray reflections or ambient light fluctuations, further improving the SNR.

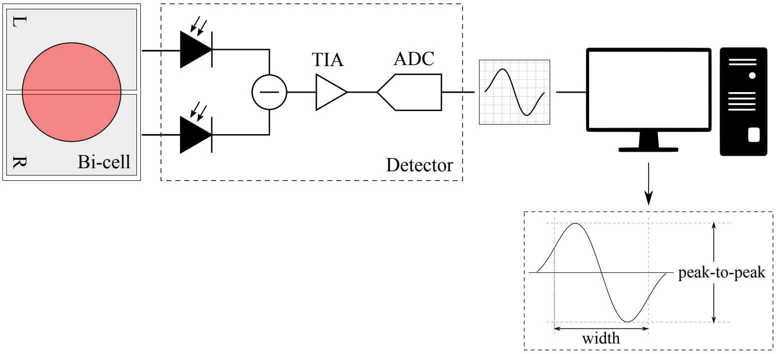

Figure 2.7: Schematic of the differential detection scheme using a bi-cell photodiode. TIA: Transimpedance amplifier, ADC: analog-to-digital converter

Figure 2.5 and Figure 2.6 show the differential signals generated while scanning a diffraction grating and an isolated sub-wavelength structure, respectively. These signals can be parametrised using metrics such as peak-to-peak amplitude or signal width, and subsequently used as input parameters to solve the inverse problem.

2.5. DISCUSSION

In this chapter, the theoretical background behind the CFS measurement technique is detailed. The technique uses a focused spot, scanned across the sample, as a measurement probe. The scattered signal is measured in the BFP of the objective lens used to generate the focused spot. The measured signal is then compared to a library of simulated responses to determine the set of sample parameters that best reproduces the experimental data. The chapter provides brief descriptions of the main components of the measurement process. The focused probe is first described using both scalar and vectorial diffraction theory, with the latter providing a more complete description for high numerical aperture systems where polarisation and longitudinal field components become significant. The forward modelling approaches used to simulate light–matter interaction are then introduced, with FDTD method and RCWA presented as complementary techniques depending on the complexity and periodicity of the sample under investigation. The role of scanning is also outlined, showing how lateral displacement of the focused spot introduces phase-dependent variations in the scattered field, which can be exploited to improve sensitivity in parameter retrieval. Finally, a differential detection scheme is discussed as a practical means of reducing the full field Fourier-plane signal to a two-pixel detection while enhancing sensitivity to asymmetries in the scattered intensity distribution. Together, these elements provide the necessary theoretical foundation for the experimental and data analysis procedures described in the upcoming chapters.

BIBLIOGRAPHY

[1] M. H. Madsen and P.-E. Hansen, "Scatterometry—fast and robust measurements of nano-textured surfaces", *Surface Topography: Metrology and Properties*, vol. 4, no. 2, p. 023 003, 2016. DOI: https://doi.org/10.1088/2051-672X/4/2/023003.

[2] S. Roy, A. C. Assafrao, S. F. Pereira, and H. P. Urbach, "Coherent Fourier scatterometry for detection of nanometer-sized particles on a planar substrate surface", *Opt. Express*, vol. 22, no. 11, pp. 13 250–13 262, 2014. DOI: https://doi.org/10.1364/OE.22.013250.

[3] J. W. Goodman, *Introduction to Fourier optics*. Roberts and Company publishers, 2005.

[4] L. Novotny and B. Hecht, *Principles of nano-optics*. Cambridge university press, 2012.

[5] P. Bobbert and J. Vlieger, "Light scattering by a sphere on a substrate", *Physica A: Statistical Mechanics and its Applications*, vol. 137, no. 1-2, pp. 209–242, 1986. DOI: https://doi.org/10.1016/0378-4371(86)90072-5.

[6] T. K. Gaylord and M. Moharam, "Analysis and applications of optical diffraction by gratings", *Proceedings of the IEEE*, vol. 73, no. 5, pp. 894–937, 2005. DOI: https://doi.org/10.1109/PROC.1985.13220.

[7] A. Taflove, S. C. Hagness, and M. Piket-May, "Computational electromagnetics: The finite-difference time-domain method", *The Electrical Engineering Handbook*, vol. 3, no. 629-670, p. 15, 2005.

[8] J.-P. Bérenger, *Perfectly matched layer (PML) for computational electromagnetics*. Springer, 2007, vol. 8. DOI: https://doi.org/10.1007/978-3-031-01696-7.

[9] M. Moharam and T. K. Gaylord, "Rigorous coupled-wave analysis of planar-grating diffraction", *Journal of the Optical Society of America*, vol. 71, no. 7, pp. 811–818, 1981. DOI: https://doi.org/10.1364/JOSA.71.000811.

[10] M. Moharam, E. B. Grann, D. A. Pommet, and T. Gaylord, "Formulation for stable and efficient implementation of the rigorous coupled-wave analysis of binary gratings", *Journal of the Optical Society of America A*, vol. 12, no. 5, pp. 1068–1076, 1995. DOI: https://doi.org/10.1364/JOSAA.12.001068.

[11] R. Storn and K. Price, "Differential evolution - a simple and efficient heuristic for global optimization over continuous spaces", *Journal of global optimization*, vol. 11, no. 4, pp. 341–359, 1997. DOI: https://doi.org/10.1023/A:1008202821328.

[12] C. J. Raymond, M. E. Littau, A. Chuprin, and S. Ward, "Comparison of solutions to the scatterometry inverse problem", in *Metrology, Inspection, and Process Control for Microlithography XVIII*, SPIE, vol. 5375, 2004, pp. 564–575. DOI: https://doi.org/10.1117/12.538662.

[13] X. Chen, S. Liu, C. Zhang, and J. Zhu, "Improved measurement accuracy in optical scatterometry using fitting error interpolation based library search", *Measurement*, vol. 46, no. 8, pp. 2638–2646, 2013. DOI: https://doi.org/10.1364/AO.52.006726.

[14] I. Kallioniemi, J. Saarinen, and E. Oja, "Optical scatterometry of subwavelength diffraction gratings: Neural-network approach", *Applied optics*, vol. 37, no. 25, pp. 5830–5835, 1998. DOI: https://doi.org/10.1364/AO.37.005830.

[15] O. El Gawhary, N. Kumar, S. Pereira, W. Coene, and H. Urbach, "Performance analysis of coherent optical scatterometry", *Applied Physics B*, vol. 105, no. 4, pp. 775–781, 2011. DOI: https://doi.org/10.1007/s00340-011-4794-7.

[16] N. Kumar, O. El Gawhary, S. Roy, *et al.*, "Coherent Fourier scatterometry: Tool for improved sensitivity in semiconductor metrology", in *Metrology, Inspection, and Process Control for Microlithography XXVI*, SPIE, vol. 8324, 2012, pp. 279–286. DOI: https://doi.org/10.1117/12.916357.

[17] N. Kumar, O. El Gawhary, S. Roy, S. Pereira, and H. Urbach, "Phase retrieval between overlapping orders in coherent Fourier scatterometry using scanning", *Journal of the European Optical Society-Rapid Publications*, vol. 8, p. 13 048, 2013. DOI: https://doi.org/10.2971/jeos.2013.13048.

3

PRACTICAL LIMITS TO DETECTABILITY

This chapter quantifies the practical detection limits of CFS set by optical aberrations, electronic bandwidth, and available optical power. Using controlled Zernike modes applied with a spatial light modulator, we measure how aberrations reshape the Fourier plane intensity and the corresponding difference signal, and derive the minimum detector bandwidth from the optical cutoff and scan trajectories.

Parts of this chapter have been published in Optical Measurement Systems for Industrial Inspection XIV. **13567**, (2025) [1].

The CFS signal arises from the interaction of a tightly focused beam with the sample. In practice, the smallest detectable structure is determined by the peak-to-peak of the difference signal compared to the noise floor. In this chapter, we analyse three common issues that can affect the detectability in CFS: (i) optical aberrations, (ii) the electronic bandwidth implied by the scan trajectory, and (iii) the available optical power.

Optical aberrations, particularly low-order terms such as defocus (C_2^0), astigmatism ($C_2^{\pm 2}$), coma ($C_3^{\pm 1}$), and spherical aberration (C_4^0), distort the focal plane intensity distribution and, in turn, the scattered field recorded in the Fourier plane, typically reducing the peak-to-peak difference signal and altering the Fourier-plane intensity distribution.

The detector bandwidth must be sufficient to cover the temporal frequency spectrum of the CFS signal, which in turn depends on the scanning trajectory. This chapter details the calculation of the minimum bandwidth requirements as a function of both the scanning strategy and the optical cutoff frequency.

Finally, optical power sets the overall signal level and the dominant noise regime. Within safe operating limits the difference signal generally scales approximately linearly with power, while the noise transitions from electronics-limited at low power to laser relative-intensity noise (RIN) at higher power.

3.1. OPTICAL ABERRATIONS

In this section, we study how low-order optical aberrations affect the CFS signal measured with a two-pixel difference detector. Specific aberrations are introduced using a spatial light modulator (SLM).

3.1.1. ZERNIKE POLYNOMIALS

Zernike polynomials form an orthogonal basis on the unit disk and are widely used to describe optical aberrations. Any wavefront defined on a circular pupil can be expanded as [2],

$$W(\rho,\varphi) = \sum_{n,m} C_n^m Z_n^m(\rho,\varphi) \tag{3.1}$$

where, C_n^m is the coefficient corresponding to each Zernike polynomial Z_n^m in the decomposition of the general wavefront W defined on a unit circle ($0 \le \rho \le 1$, $0 \le \varphi \le 2\pi$). Following this definition, each coefficient, C_n^m, gives the peak-valley (PV) wavefront error of the corresponding polynomial:

$$Z_n^m(\rho,\varphi) = R_n^m(\rho)\cdot\left\{\begin{array}{ll} \cos m\varphi & m \ge 0 \\ \sin m\varphi & m < 0 \end{array}\right\}. \tag{3.2}$$

The radial function $R_n^m(\rho)$ is defined as,

$$R_n^m(\rho) = \sum_{k=0}^{(n-m)/2} (-1)^k \frac{(n-k)!}{k!(\frac{n+m}{2}-k)!(\frac{n-m}{2}-k)!}\rho^{n-2k}. \tag{3.3}$$

where, $n = 0,1,2$, etc. is the radial index and $m = -n, -n+2, \ldots, n-2, n$ is the azimuthal index.

In this study, we limit our focus to low-order aberrations: defocus (Z_2^0), astigmatism (Z_2^2), oblique astigmatism (Z_2^{-2}), horizontal coma (Z_3^1), vertical coma (Z_3^{-1}), and spherical (Z_4^0) aberrations. Figure 3.1 shows the different Zernike aberrations (each with 0.4λ PV error) alongside their corresponding focal-plane intensity patterns, calculated using the Richards–Wolf vectorial diffraction integral [3]. For each mode, the simulated two-dimensional difference signal for a Si sample with a 400 nm diameter, 150 nm deep etched pit (input field linearly polarised along x in the pupil plane, NA = 0.4, $\lambda = 632.8\,\text{nm}$) is also shown.

3.1.2. EXPERIMENTAL SETUP

The influence of individual aberrations on the CFS scan signal was studied by introducing controlled amounts of each aberration into the Fourier plane of the objective using an SLM. The modified CFS setup, including the SLM (Holoeye Pluto VIS), is shown in Figure 3.2.

The experimental setup consists of a HeNe laser followed by a linear polariser (P) and a rotatable half-wave plate (HWP) to align the input polarisation, and then a beam expander constructed using lenses L1 ($f = 10\,\text{mm}$) and L2 ($f = 250\,\text{mm}$) forming a telescopic system. The expanded beam is then incident on the SLM for phase modulation. The modified wavefront is relayed to the back focal plane (BFP) of the objective (N PLAN L 20x/0,40 NA, Leica) using another telescope system formed using lenses L3 ($f = 200\,\text{mm}$) and L4 ($f = 250\,\text{mm}$). The objective focuses the light on the sample and collects the scattered field. The field in the BFP after reflection is relayed to the difference detector (SD 113-24-21-02) and camera using telescopic pairs L5-L6 ($f = 40\,\text{mm}$) and L5-L7 ($f = 50\,\text{mm}$). A flipping mirror is used to switch the beam path between the detector and camera.

A beam splitter separates the incident and reflected beams at the SLM while maintaining normal incidence on the device. Although this configuration incurs higher power loss compared to using a small tilt on the SLM, it simplifies the process of applying and projecting aberrations without requiring tilt correction. The power incident on the sample is 85 µW.

The sample is mounted on a stack of piezo stages: an x-y translator (P-625.2 CD, Physik Instrumente) for 2D raster scanning and a z-piezo (PI-753.3, Physik Instrumente) for fine focus adjustments. The piezo stages have different in-built sensors that can provide positional information for feedback. These feedback signals are used to assign x and y coordinate information to the difference signal, enabling us to create a 2D differential scattering map. The difference signal along with the feedback signals is recorded using an ADC (NI 5734, National Instruments).

3.1.3. INFLUENCE ON THE DIFFERENCE SIGNAL

The point spread function (PSF) of an optical system describes its response to a point source. In microscopy, fluorescent microspheres embedded in a homogeneous medium are commonly used to estimate the PSF experimentally [4]. Similarly, the 2D difference signal of the CFS system for a sub-wavelength scatterer provides a useful proxy for the optical response. The differential maps do not correspond exactly to the PSF, but they do provide a good qualitative approximation. The sample used here consists of pits of

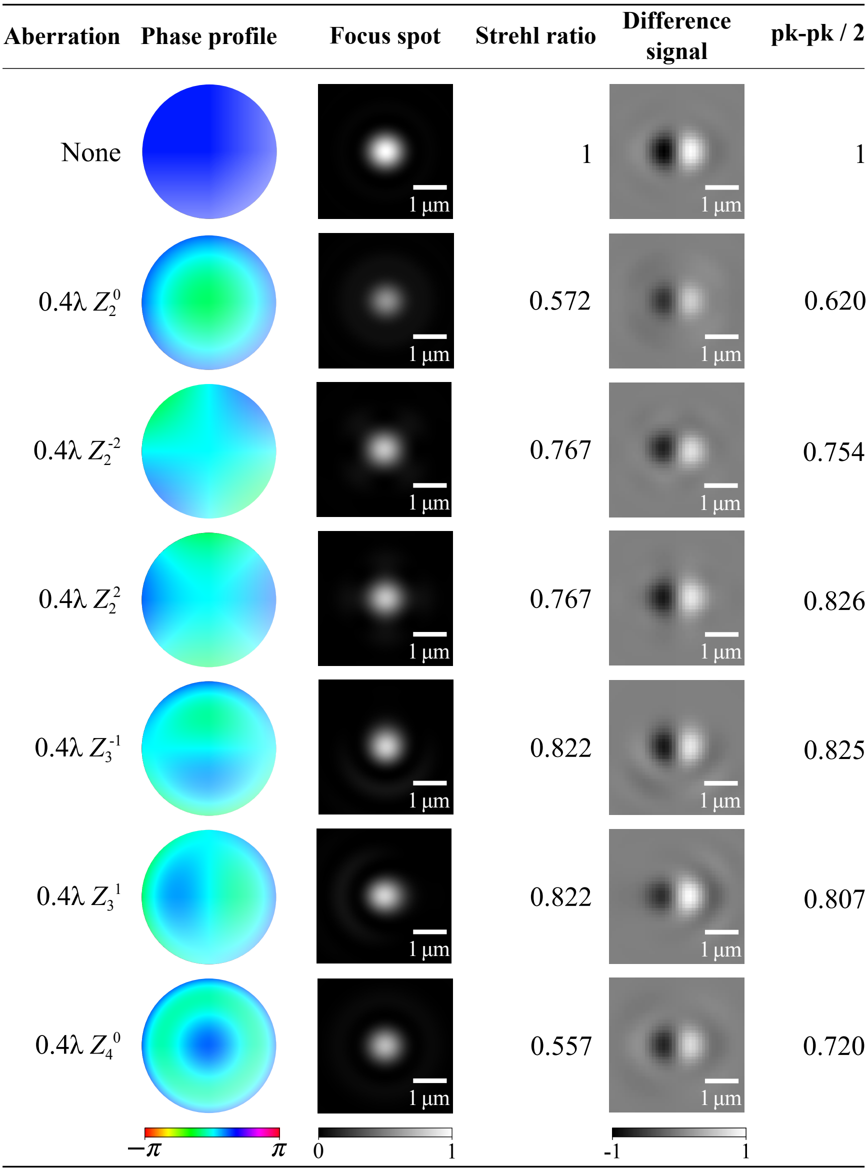

Figure 3.1: Theoretical point spread function intensities of 0.4 NA focusing system with different Zernike aberrations in the sample plane along with the input phase distribution in the Fourier plane. The field is polarised along the x-direction in the Fourier plane. The coefficients correspond to PV error for each wavefront.

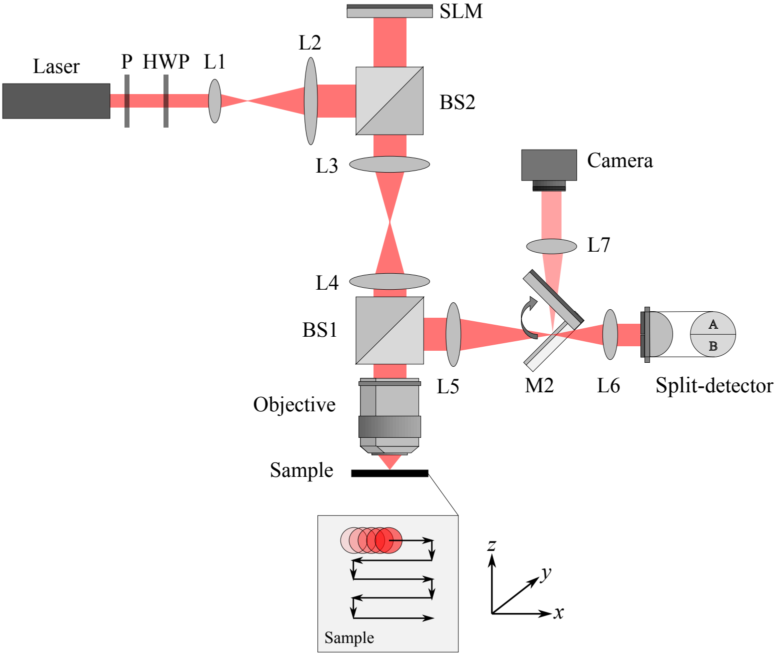

Figure 3.2: Schematic of the CFS setup including the SLM for calibration. Lenses L1 - 10 mm, L2 - 250 mm, L3 - 200 mm, L4 - 250 mm, L5 - 200 mm, L6 - 40 mm, L7 - 50 mm, beam splitters - BS1, BS2, Objective - 0.4 NA objective lens, M1 - flipping mirror, SLM - spatial light modulator (Holoeye Pluto VIS), P - polariser, HWP - half-wave plate. The system uses a HeNe laser with 632.8 nm wavelength.

425 nm diameter and 150 nm depth etched into silicon. The theoretical size of an unaberrated focused spot for NA = 0.40 is 1.93 µm [5].

Figure 3.3 shows the normalised 2D difference signals of a single etched pit when scanned using focused spots with different aberrations. The rows correspond to scans made at different axial (z) planes: -5 µm, -2 µm, 0 µm, and 2 µm, with $z = 0$ µm corresponding to the plane yielding the highest peak-to-peak. Each column corresponds to a distinct aberration: (a) no added aberration (baseline/defocus Z_2^0 at its optimum), (b) spherical (Z_4^0), (c) astigmatism (Z_2^2), (d) oblique astigmatism (Z_2^{-2}), and (e) vertical coma (Z_3^{-1}).

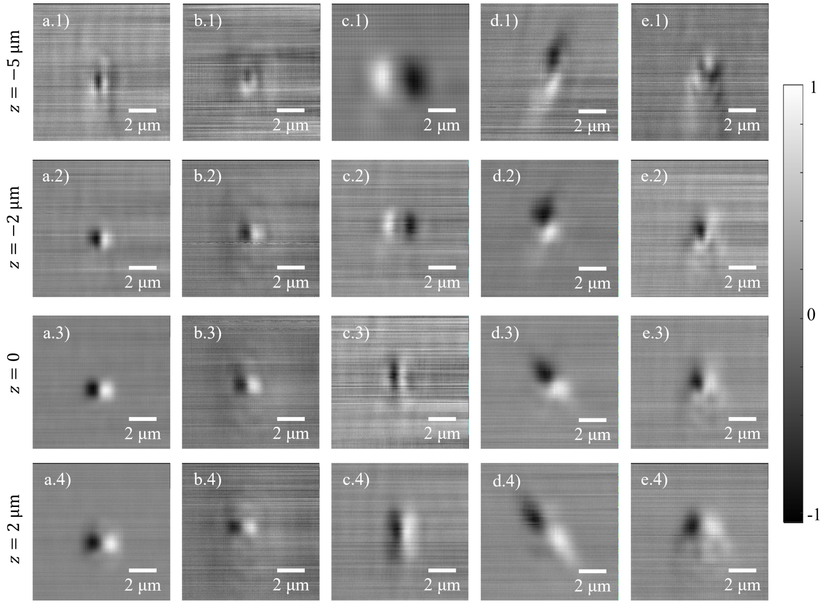

Figure 3.3: Optical response of the CFS setup to a sub-wavelength scatterer. Shown are 2D scans of a pit of 425 nm diameter etched in Si with 150 nm depth. Scans were acquired at 632.8 nm using a 0.40 NA objective. Columns correspond to specific aberrations, rows correspond to different z-planes. Panels: a.1–a.4 no added aberration; b.1–b.4 1λ spherical; c.1–c.4 0.8λ astigmatism; d.1–d.4 0.8λ oblique astigmatism; e.1–e.4 1λ vertical coma.

The scans look similar to familiar aberrated PSFs in lensed systems. For the astigmatic spot, the difference signal is elongated horizontally in the $z = -2$ µm plane and vertically in the $z = 2$ µm plane. In the presence of oblique astigmatism, the lobes rotate by approximately ±45° with respect to the scan direction (x-axis) and are stretched along those diagonals as z varies. For spherical and coma aberrations, additional ring-like structures appear around the central lobes, although their visibility is limited by the SNR. The response for horizontal coma is similar to that for vertical coma, rotated by 90°.

3.1.4. INFLUENCE ON PEAK-TO-PEAK

In many applications, the peak-to-peak value of the difference signal serves as the measurand to characterise nanostructure geometry. For example, it can be used to estimate the diameter of particulate contamination on a Si wafer. It is therefore important to quantify how optical aberrations affect this metric. To that end, for each aberration the Zernike coefficient was swept over a PV range from -1λ to $+1\lambda$, and the resulting peak-to-peak value was extracted from the corresponding scans. The sample consisted of an array of pits of 425 nm diameter and 150 nm depth etched in Si. Figure 3.4 shows the peak-to-peak difference signal as a function of the aberration coefficient for each mode. Each data point is the mean of five independent measurements.

We quantify the influence of each aberration by the coefficient required to reduce the peak-to-peak difference signal to 50% of its unaberrated value. Let C_{50} denote this PV wavefront error in waves. Defocus has the strongest effect ($C_{50} \approx 0.27\lambda$), followed by spherical aberration ($C_{50} \approx 0.32\lambda$) and horizontal coma ($C_{50} \approx 0.40\lambda$). Oblique astigmatism is the least influential, requiring $\approx 0.62\lambda$ to halve the signal. In practice, defocus is also the most readily corrected when the sample is mounted on a z-adjustable stage: a 50% reduction corresponds experimentally to moving the sample by $\Delta z = 3.75\,\mu\text{m}$ from the plane of maximum peak-to-peak.

3.1.5. DISTINCTION BETWEEN MAXIMUM PEAK-TO-PEAK SIGNAL PLANE AND FOCAL PLANE

The peak-to-peak of the difference signal attains its maximum at a z-plane that is offset from best focus. Under small even aberrations (e.g., defocus), the first-order correction term to the difference signal is real and odd in the scan coordinates, so the peak-to-peak difference signal shifts away from best focus and varies linearly with small defocus (its sign set by the defocus coefficient and the sample spectrum) (see Appendix B for the detailed derivation). By contrast, the sum (integrating) channel remains even in scan and therefore peaks near the focal plane.

The shift is evident in both experiment Figure 3.5a and simulation Figure 3.5b. The peak of the sum signal aligns closely with the focal position, while the peak of the difference signal is displaced along z by about $1.25\,\mu\text{m}$ in simulation and $1.3\,\mu\text{m}$ in measurement ($\text{NA} = 0.40$, $\lambda = 632.8\,\text{nm}$, pit diameter 425 nm, depth 150 nm). The simulations were performed using the commercial FDTD solver, Lumerical and the scattering object consisted of a pit of 400 nm diameter and 150 nm depth etched in Si. The z separation is not constant and it changes with the sample properties. Figure 3.5c shows the 2D difference maps for another sample measured at different z-planes. The sample consisted again of a pit of 425 nm diameter etched in Si but with a larger etch depth.

3.1.6. INFLUENCE ON THE FOURIER PLANE

For applications requiring the full Fourier field information for parameter inference, it is important to understand the influence of different optical aberrations on the reflected field measured as the Fourier field intensity. Figure 3.6a shows the simulated intensity distributions when the centre of the focused spot with different aberrations is coincident with the centre of the nanostructure. The structure consists of an etched pit of 400 nm diameter and 150 nm etch depth in a Si substrate. The simulations were performed us-

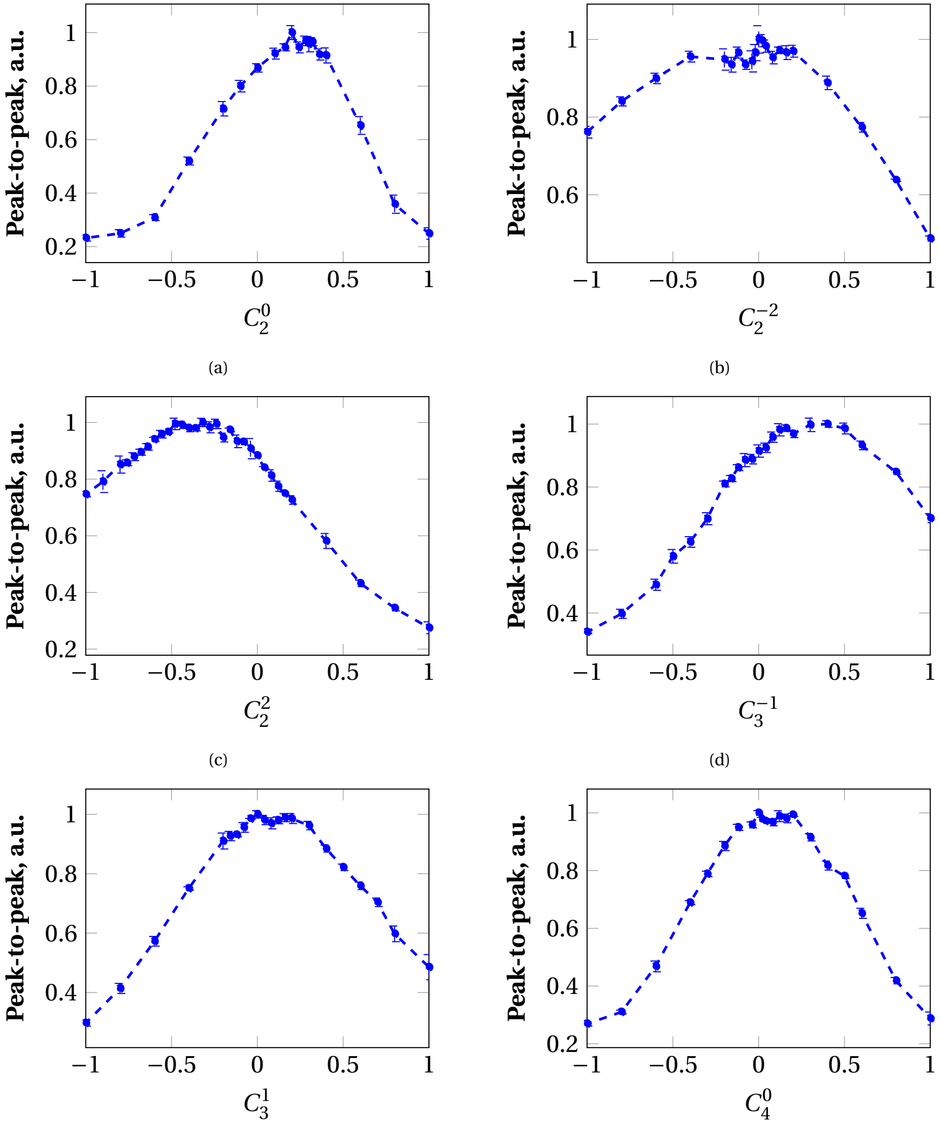

(a) (b) (c) (d) (e) (f)

Figure 3.4: Peak-to-peak difference signal versus Zernike coefficient for (a) defocus (Z_2^0), (b) oblique astigmatism (Z_2^{-2}), (c) astigmatism (Z_2^2), (d) vertical coma (Z_3^{-1}), (e) horizontal coma (Z_3^1), and (f) spherical aberration (Z_4^0). The sample is an array of pits of 425 nm diameter and 150 nm depth etched in silicon. Measurements were taken with NA = 0.40 at $\lambda = 632.8$ nm. Zernike coefficients were swept over $\pm 1\lambda$ (PV). Each point is the mean of five repeats, error bars denote the standard deviation.

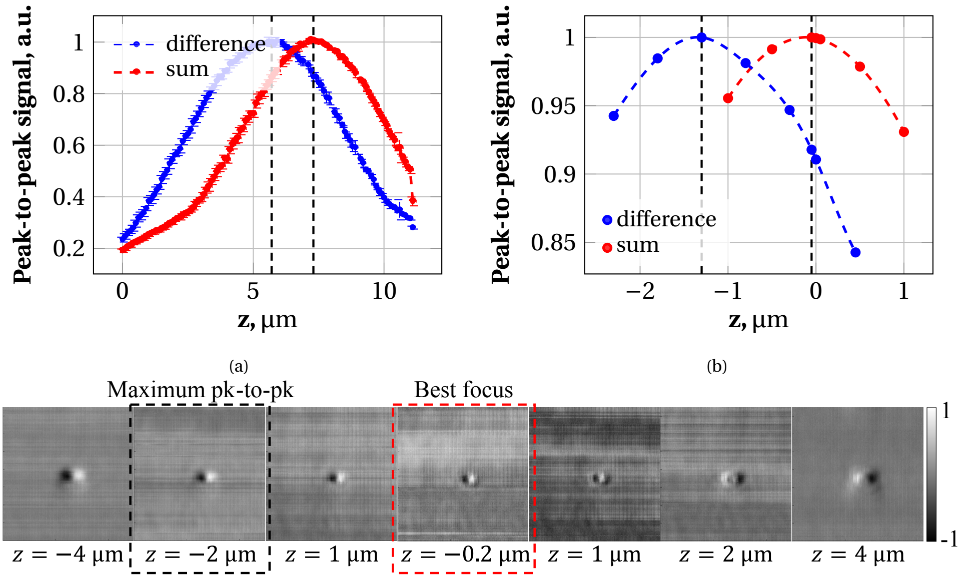

(a)

(b)

(c)

Figure 3.5: Peak-to-peak vs. defocus. (a) Experimental data and (b) simulations. The z position of the maximum peak-to-peak is displaced by about 1.3 µm (measurement) and 1.25 µm (simulation) for NA = 0.40, $\lambda = 632.8$ nm, pit diameter 425 nm, depth 150 nm. Dashed vertical lines mark the peak locations. (c) Through-focus 2D difference maps for different z. The sample for the 2D scans consists of an etched pit with 425 nm diameter and etch depth larger than 150 nm.

ing the commercial FDTD solver (Lumerical). It is not easy to recognise the influence of different aberrations from the distributions visually. However, when the Fourier field intensity of the unaberrated case is subtracted from that of the aberrated case (aberrated − unaberrated), the difference resembles the phase of the aberrated input field. This is especially evident from the experimental Fourier field intensity data shown in Figure 3.6b. The plots show the Fourier field intensities when no aberration is added, when 0.4λ astigmatism is added, and the difference between the two. Figure 3.6c shows the Fourier-field intensity patterns simulated in the presence of different optical aberrations using RCWA. The grating parameters are: 1200 nm period, 50 % duty cycle, 150 nm height, and 90° side-wall angle. The optical parameters are: NA = 0.40, $\lambda = 633$ nm, and input x-polarised in the pupil plane. The influence of the aberrations is seen most clearly in the overlap region between the zeroth and first diffraction orders.

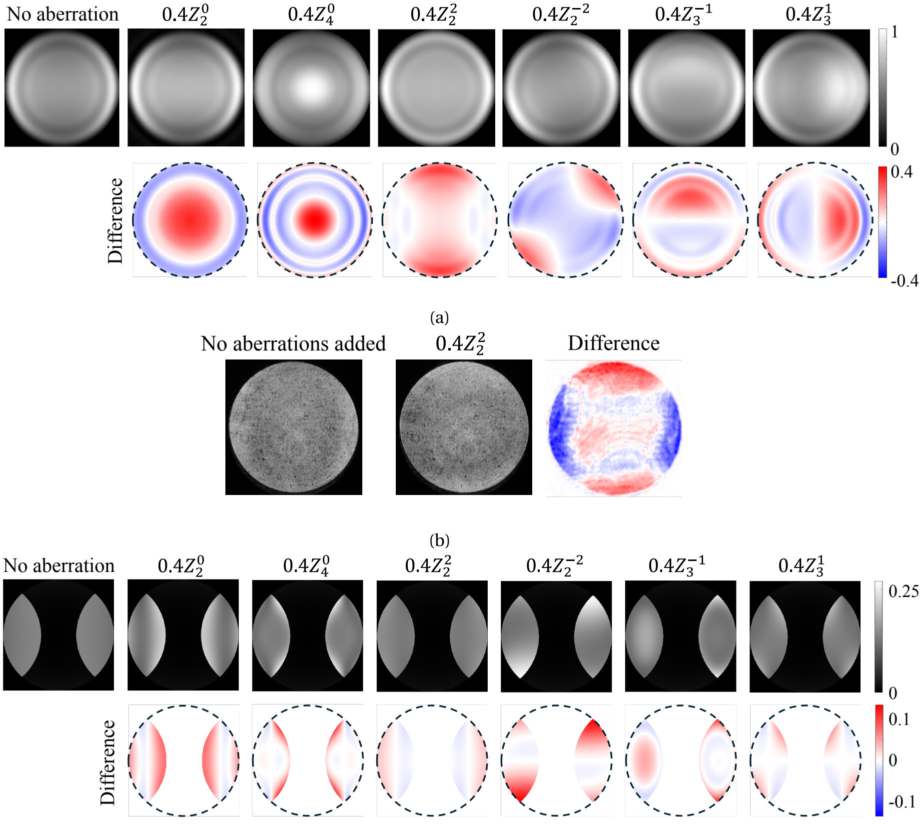

(a)

(b)

(c)

Figure 3.6: a) Simulated Fourier plane intensities for aberrated focused spots centred on a 400 nm-diameter, 150 nm-deep etched pit in Si (FDTD, Lumerical) along with the difference images (aberrated – unaberrated). b) Experimental validation using a focused spot with 0.4λ astigmatic aberration. c) Simulated Fourier plane intensities from a grating sample of 1200 nm period, 50% duty cycle, 150 nm height, 90° side-wall angles. The optical parameters are : 0.4 NA, $\lambda = 633$ nm, x-polarised in the pupil plane.

3.2. ELECTRONIC BANDWIDTH

For a general sample surface, let the spatial measurement be $s(x)$, where x is the lateral position. With constant scan speed v (so $x = vt$), the time-domain signal is

$$s_t(t) \equiv s(vt). \tag{3.4}$$

Using Fourier transform,

$$S(f_x) = \int_{-\infty}^{\infty} s(x) \exp\left[-i2\pi(xf_x)\right] dx, \tag{3.5}$$

we obtain the scaling relation,

$$\mathscr{F}\{s(x)\} = S\left(f_x\right) \tag{3.6}$$

$$\mathscr{F}\{s(vt)\} = \frac{1}{|v|} S'\left(\frac{f}{v}\right), \tag{3.7}$$

where, f_x and f are the spatial and temporal frequencies, related by $f = vf_x$. The relation shows that the temporal frequency spectrum stretches with the scanning speed. The higher the scanning speed, the larger the spectrum. To accurately represent the measurement signal, the detection bandwidth must be sufficient to cover the signal spectrum, making the maximum scanning speed of the measurement dependent on the detection bandwidth as shown in Figure 3.7. The area in gray shows the detector bandwidth. The curves show the spectrum of the measurement signal measured at two different scanning speeds: v (red) and $2v$ (blue). The red curve fits completely the gray area indicating that the detector can accurately represent the measurement signal. The blue curve extends outside the detector bandwidth and the corresponding measurement signal can no longer be accurately represented.

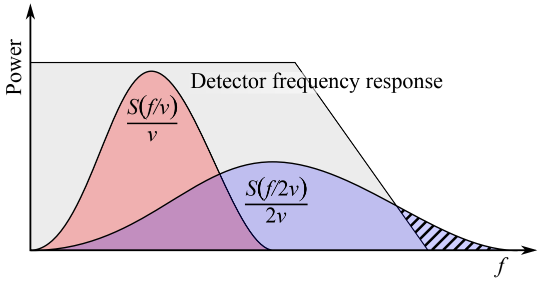

Figure 3.7: Schematic of the frequency spectrum of the measurement signal measured at two scanning speeds: v, shown in red, and $2v$, shown in blue.

3.2.1. MINIMUM BANDWIDTH

There are two factors to consider when computing the minimum detection bandwidth: (i) the scanning velocity, which maps spatial frequencies to temporal frequencies via $f = vf_x$, and (ii) the optical cutoff frequency of the imaging system, which sets the highest spatial frequency that can pass.

The optical cutoff frequency is the highest spatial frequency that the optical system can pass. Any object can be expressed as a sum of sinusoidal gratings at different angles. Therefore, the optical cutoff frequency of the system is the highest grating frequency that can be measured. Assuming no non-linear effects are present in the interaction of the spot with the grating, the largest spatial frequency that can be detected is [6]–[8]:

$$f_{\text{cutoff}} = \frac{2\text{NA}}{\lambda}, \tag{3.8}$$

where λ is the wavelength of the coherent source and NA is the numerical aperture of the focusing lens.

For a grating with period $1/f_{\text{cutoff}}$, the difference signal at a scan position x is,

$$s(x) = \frac{\text{V}_{\text{pp}}}{2}\sin\left(2\pi f_{\text{cutoff}}\, x\right), \tag{3.9}$$

where V_{pp} is the peak-to-peak of the differential signal. With a scan trajectory $x = g(t)$, the measured time signal is,

$$s'(t) = s(g(t)) = \frac{\text{V}_{\text{pp}}}{2}\sin\left(2\pi f_{\text{cutoff}}\, g(t)\right). \tag{3.10}$$

The bandwidth depends on the scanning strategy [9]. For band-limited spectrum, the detection bandwidth can be determined based on the largest frequency content present. For non-band-limited spectrum, a good strategy would be to choose the detector bandwidth that covers 99% of the power. Let us consider a few examples of different scanning strategies but with uniform sampling in the time domain. The optical system in all cases uses a wavelength of 632.8 nm and an objective of 0.4 NA. The optical cutoff frequency, $f_{\text{cutoff}} = 1.264$ cycles/µm.

3.2.2. INFLUENCE OF SCANNING TRAJECTORY

Constant linear velocity: $x = vt$, where v is the velocity,

$$s'(t) = \frac{\text{V}_{\text{pp}}}{2}\sin\left(2\pi f_{\text{cutoff}}\, vt\right). \tag{3.11}$$

$$S(f) = \frac{1}{2i}\left[\delta(f - v f_{\text{cutoff}}) + \delta(f + v f_{\text{cutoff}})\right] \tag{3.12}$$

The largest signal frequency is $|v| f_{\text{cutoff}}$. Figure 3.8a shows the simulated differential scan signal for a grating with period $1/f_{\text{cutoff}}$ measured with a constant scan velocity, $v = 300\,\mu\text{m/s}$. The corresponding frequency spectrum is shown in Figure 3.8b. The spectrum is band-limited with the highest frequency peak at 379.2 Hz.

Sinusoidal scanning: $x = \frac{w}{2}\sin\left(2\pi f_{\text{scan}}\, t\right)$, where, w is the total scan width, f_{scan} is the scan frequency in Hz,

$$s'(t) = \frac{\text{V}_{\text{pp}}}{2}\sin\left[2\pi f_{\text{cutoff}}\left(\frac{w}{2}\sin\left(2\pi f_{\text{scan}}\, t\right)\right)\right] \tag{3.13}$$

$$= \frac{\text{V}_{\text{pp}}}{2}\sin\left(\beta\sin(2\pi f_{\text{scan}}\, t)\right), \quad \beta = \pi w f_{\text{cutoff}}, \tag{3.14}$$

$$= \frac{\text{V}_{\text{pp}}}{2}\left[2\sum_{n=1}^{\infty} J_{2n-1}(\beta)\sin\left((2n-1)2\pi f_{\text{scan}}\, t\right)\right] \tag{3.15}$$

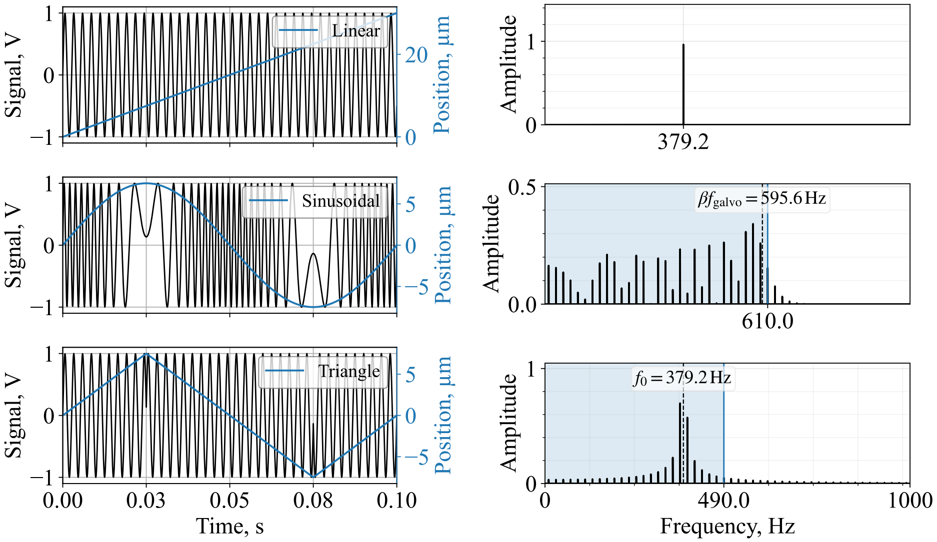

(a) (b)

Figure 3.8: Effect of scanning strategies on the measured differential signal and its spectrum. (a) Time-domain signals $s'(t)$ (black, left axis) with the corresponding scan position $x(t)$ (blue, right axis) for constant linear velocity, sinusoidal, and triangular trajectories. (b) One-sided amplitude spectra $|S'(f)|$ for the same cases. Parameters: $\lambda = 632.8\,\text{nm}$, NA = 0.4, $f_{\text{cutoff}} = 1.264\,\text{cycles/µm}$; $f_{\text{scan}} = 10\,\text{Hz}$, $w = 15\,\text{µm}$, and (linear) $v = 300\,\text{µm}\,\text{s}^{-1}$. The linear/triangular scans concentrate the power near $f_0 = v\,f_{\text{cutoff}} = 379.2\,\text{Hz}$; the sinusoidal scan produces odd harmonics of f_{scan} with most of the energy within $\beta f_{\text{scan}} = 595.6\,\text{Hz}$, $\beta = \pi w f_{\text{cutoff}}$. In (b), the shaded region marks the area below which 99% of the spectral power is contained. Dashed markers indicate βf_{scan} (sinusoid) and f_0 (triangle).

The signal expression is expanded using Jacobi-Anger expansion. The signal spectrum can be computed by taking the Fourier transform,

$$S'(f) = \frac{\mathrm{V_{pp}}}{2i}\left[\sum_{n=1}^{\infty} J_{2n-1}(\beta)\left[\delta(f-(2n-1)f_{\mathrm{scan}})+\delta(f+(2n-1)f_{\mathrm{scan}})\right]\right]. \tag{3.16}$$

The spectrum contains only the odd harmonics of f_{scan} with the magnitude determined by $J_{(2n-1)}(\beta)$. For a quick approximation, the required detection bandwidth $\approx \beta f_{\mathrm{scan}} = \pi w f_{\mathrm{cutoff}} f_{\mathrm{scan}}$, as the values of $J_{(2n-1)}(\beta)$ decay rapidly after $2n-1 > \beta$. Figure 3.8a shows the differential signal acquired during one period of the scan using a sinusoidal input with $f_{\mathrm{scan}} = 10\,\mathrm{Hz}$, $w = 15\,\mu\mathrm{m}$. Figure 3.8b shows the corresponding frequency spectrum: $\beta f_{\mathrm{scan}} = 595.6\,\mathrm{Hz}$, 99% of the power in the spectrum is contained in the frequencies $\leq$ 610 Hz.

Triangular scanning: $x(t) = \frac{w}{\pi}\arcsin(\sin 2\pi f_{\mathrm{scan}} t)$. The time signal is

$$s'(t) = \frac{V_{\mathrm{pp}}}{2}\sin\left[2 w f_{\mathrm{cutoff}}\left(\arcsin(\sin 2\pi f_{\mathrm{scan}} t)\right)\right]. \tag{3.17}$$

A triangular scan moves at constant speed on each half-period and reverses at the turning points. The turnarounds (slope reversals every $1/2 f_{\mathrm{scan}}$) impose a periodic phase discontinuity that generates a line comb around $f_0 = 2 w f_{\mathrm{scan}} f_{\mathrm{cutoff}}$ at odd multiples of f_{scan}. For the scan parameters, $w = 15\,\mu\mathrm{m}$, $f_{\mathrm{scan}} = 10\,\mathrm{Hz}$, a detector bandwidth of $f =$ 490 Hz captures ≥99% of the signal power. Figure 3.8 shows the differential signal generated when scanning using a triangular waveform as well as the corresponding frequency spectrum. For a quick rule of thumb calculation, using $f_0 + c f_{\mathrm{scan}}$, where $c \approx 5-10$ should suffice. Smoothening the turnarounds will reduce the energy in the sidebands, lowering the required bandwidth. A sinusoidal waveform thus puts higher requirements on the detection bandwidth compared to the linear strategies.

3.3. OPTICAL POWER

Understanding the relation between the input laser power and the output signal is important for setting the detector gain and power budget. Over the range tested, the response is linear: the peak-to-peak value of the difference signal scales linearly with the incident power. Figure 3.9 plots V_{pp} versus input power together with a linear least-squares fit. The sample measured consisted of 400 nm PSL particles on a Si wafer. The objective used has a 0.1 NA and the incident wavelength is 632.8 nm. The power at the sample plane was measured using a power meter placed directly in the focal plane.

3.4. DISCUSSION

In this chapter, the practical limits for CFS measurements in terms of optical aberrations, electronic bandwidth and optical power is discussed.

The influence of optical aberrations on the CFS signal was characterised by introducing controlled wavefront errors to a CFS setup using an SLM. The effect of the aberrations in the 2D differential scan maps were found to be similar to the influence of aberrated PSFs in microscopy systems. Among the aberrations studied, defocus has the

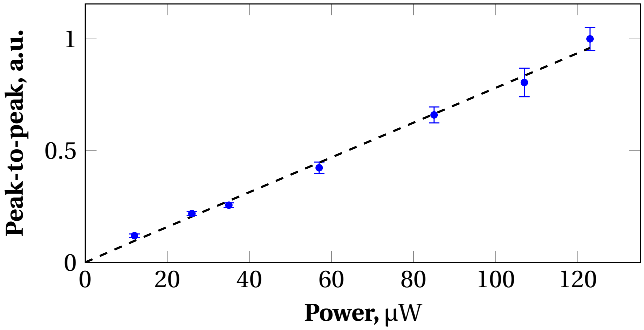

Figure 3.9: Variation in peak-to-peak of difference signal as a function of the incident power: measured data (blue markers), linear fit (black dashed).

strongest impact, followed by spherical aberration and coma, while astigmatic modes are less detrimental.

While defocus can be readily corrected with axial adjustment, higher-order aberrations require careful optical design or correction. Understanding how these aberrations influence CFS performance is crucial not only for understanding the performance of current CFS systems but also for designing future setups. For example, substituting piezo stages with beam-scanning galvo mirrors for high-throughput scanning, could introduce significant astigmatism and coma aberrations, affecting overall system performance. The current study can be used to determine the range of scan angles that can be used without significantly affecting the performance of the system.

The electronic bandwidth requirement is determined by both the optical cutoff frequency and the scan trajectory. Linear and triangular scans concentrate power near a carrier frequency and are bandwidth-efficient, whereas sinusoidal scans distribute power across harmonics, increasing bandwidth requirements. Finally, the peak-to-peak signal scales linearly with optical power within the tested range, indicating that SNR can be improved by increasing power until laser noise or detector limits dominate.

BIBLIOGRAPHY

[1] S. Soman and S. F. Pereira, "Aberration characterisation in coherent Fourier scatterometry", in *Optical Measurement Systems for Industrial Inspection XIV*, SPIE, vol. 13567, 2025, pp. 557–564. DOI: https://doi.org/10.1117/12.3062562.

[2] ISO 21457:2008(E), "Ophthalmic optics and instruments — Reporting aberrations of the human eye", International Organization for Standardization, Standard, 2008.

[3] I. Herrera and P. A. Quinto-Su, *Simple computer program to calculate arbitrary tightly focused (propagating and evanescent) vector light fields*, https://arxiv.org/abs/2211.06725, 2022. arXiv: 2211.06725 [physics.optics].

[4] R. W. Cole, T. Jinadasa, and C. M. Brown, "Measuring and interpreting point spread functions to determine confocal microscope resolution and ensure quality control", *Nature Protocols*, vol. 6, no. 12, pp. 1929–1941, 2011.

[5] J. W. Goodman, *Introduction to Fourier optics*. Roberts and Company publishers, 2005.

[6] N. Fukutake, "A general theory of far-field optical microscopy image formation and resolution limit using double-sided feynman diagrams", *Scientific reports*, vol. 10, no. 1, p. 17 644, 2020. DOI: https://doi.org/10.1038/s41598-020-73584-1.

[7] C. Sheppard and C. Cogswell, "Three-dimensional image formation in confocal microscopy", *Journal of microscopy*, vol. 159, no. 2, pp. 179–194, 1990. DOI: https://doi.org/10.1111/j.1365-2818.1990.tb04774.x.

[8] G. Bouwhuis and J. Spruit, "Optical storage read-out of nonlinear disks", *Applied optics*, vol. 29, no. 26, pp. 3766–3768, 1990. DOI: https://doi.org/10.1364/AO.29.003766.

[9] Y. R. Teo, Y. Yong, and A. J. Fleming, "A comparison of scanning methods and the vertical control implications for scanning probe microscopy", *Asian Journal of Control*, vol. 20, no. 4, pp. 1352–1366, 2018. DOI: https://doi.org/10.1002/asjc.1422.

4

MULTI-BEAM COHERENT FOURIER SCATTEROMETRY

This chapter describes the design and implementation of a multi-beam coherent Fourier scatterometry (CFS) system. By using a diffraction grating to generate multiple beams and a photodiode array for parallel signal acquisition, this method enables faster surface inspection compared to single-beam CFS.

Parts of this chapter have been published in Meas. Sci. Technol. **35**, 075905 (2024) [1].

This chapter outlines a parallelisation strategy for coherent Fourier scatterometry (CFS) that uses multiple probes to reduce overall scan time. Comparable approaches have been adopted in fields such as optical data storage, scanning electron microscopy (SEM), and confocal microscopy, where throughput is typically constrained by scanning processes [2]–[6]. In the system described here, a diffraction grating is used to generate multiple spatially separated optical beams, while an array of split detectors facilitates parallel signal acquisition, thereby improving measurement throughput.

The remainder of this chapter is organised as follows. section 4.1 details the experimental setup—beam generation with a 1D diffraction grating, relay optics to the objective BFP, and parallel detection with a photodiode array and microlens array. section 4.2 analyses inter-focal separation at the sample and beam placement at the detector to minimise cross-talk and offset bias. section 4.3 verifies independent detection across beams on test samples. section 4.4 presents phase-correlation tiling and required overlap. section 4.5 demonstrates calibration on etched pits of varying diameters. Finally, section 4.6 summarises limitations, scalability, and alternative architectures.

4.1. EXPERIMENTAL SETUP

Figure 4.1 shows the experimental setup of the multi-beam CFS. Light from a HeNe (λ = 632.8 nm) laser is collimated and magnified using lenses L1 (f = 8 mm) and L2 (f = 250 mm) in a telescopic arrangement. A 1D beam-splitter (TS-280-P-Y-A_1D, HoloOR) is then used to split the incident beam into three beams of similar intensities. The off-axis beams suffer from higher optical aberrations compared to the on-axis beam. Defocus and astigmatic aberrations, in particular, can cause a reduction in the signal peak-to-peak voltage measured at the detector. Thus, it is important to have optical elements that can correct for these aberrations for the off-axis beams. The coefficients for the defocus and astigmatic aberrations for each beam are measured at the back focal plane (BFP) of the objective using a Shack-Hartmann sensor and are shown in Table 4.1 along with the corresponding laser power and angular separation from the optical axis.

Table 4.1: Optical properties of the three beams generated using the 1D beam-splitter. The wavefront aberrations were measured using a Shack-Hartmann wavefront sensor in the BFP of the objective.

Beam	Power (µW)	Angle (°)	Defocus (λ)	Ast 0° (λ)	Ast 45° (λ)
Beam 1	29.0	−1.22	-0.0072	0.0195	-0.0211
Beam 2	33.8	0	-0.0081	0.0283	-0.0023
Beam 3	29.6	1.22	0.0059	0.0197	-0.0223

The beams after generation from the 1D beam-splitter are relayed to the objective BFP using lenses. The relay consists of a scan lens (L3, f = 39 mm) and a tube lens (L4, f = 165 mm) in a telescopic arrangement. The scan lens is used to flatten the focal plane curvature for the off-axis beams before the objective. This ensures that the beams after the objective have the best focus in the same plane. The objective (Leica, N PLAN L 20x/0,40) used in the setup has an NA of 0.4. The beams, after reflection from the sample, are collected using the same objective. They are relayed from the objective BFP to the detector using the lenses L5 ($f = 410$ mm) and a micro-lens array (MLA, model: MLA1M1, Thorlabs) in yet another telescopic arrangement. The MLA collimates each beam separately before the beams are incident on the detector. A photograph of the setup on the optical table is shown in Figure 4.2.

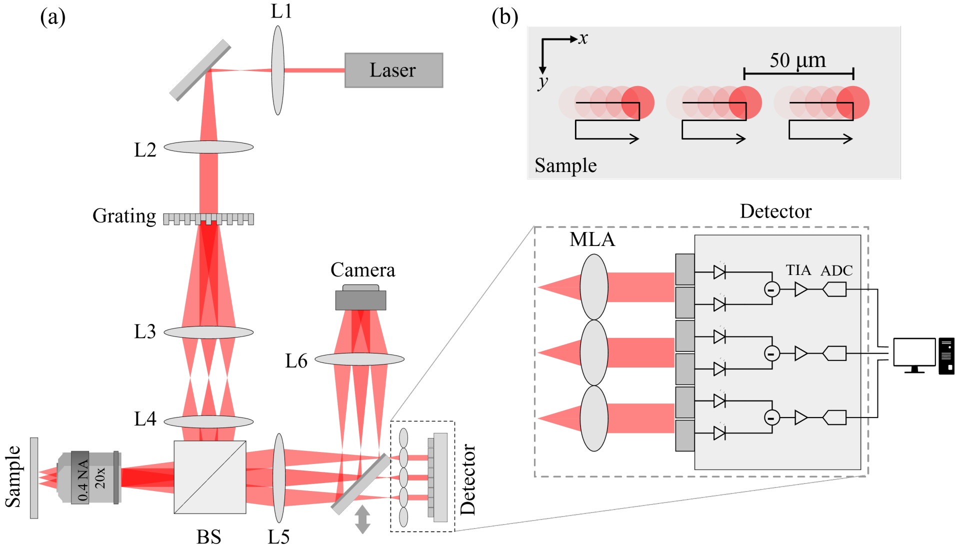

Figure 4.1: a) Schematic diagram of the setup. Objective of 0.4 NA, camera for locating features, grating to generate three beams, MLA microlens array to collimate beams individually before the detector and photodiode array for detecting each beam separately, L1 - 8 mm, L2 - 250 mm, L3 (scan lens) - 39 mm, L4 (tube lens) - 165 mm, L5 - 410 mm, L6 - 200 mm. (b) Raster scan schematic using the three beams.

The detector consists of an array of Si photodiodes (S4111-16R, Hamamatsu) with every two photodiodes working as a differential detector. The light incident on each diode generates a photocurrent and a difference signal is generated by subtracting one from the other. The MLA was chosen such that the separation between two micro lenses was equal to the separation between two differential detectors. This ensures that each beam can be made to be incident exactly in the middle of two photodiodes. The difference signal generated from each pair of photodiodes is amplified, sampled using an ADC and represented as 2D data using the position feedback signal of the scan stage measured synchronously with the detector signal. The 2D mechanical scanning is performed by raster scanning the sample in the x and y-directions using a piezo stage (P-625.2 CD, Physik Instrumente). An additional z-piezo (S-316.10H, Physik Instrumente) is used to position the sample in the focal plane of the objective. A camera is also added to locate areas of interest on the sample.

4.2. DESIGN CONSIDERATIONS

Compared to a single beam CFS using a single on-axis beam to generate a focused spot, the multi-beam design has more parameters that can influence the output signal. Let us

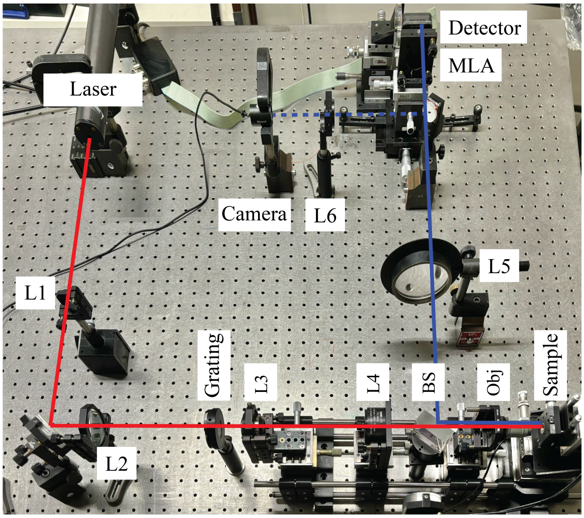

Figure 4.2: Photograph of the setup on the optical table.

consider two such parameters in detail, namely, the inter-focal separation and the beam separation at the detector plane.

4.2.1. INTER-FOCAL SEPARATION

The spot separation at the focal plane depends on the angular separation of the beams, the magnification provided by the relay lenses, and the NA of the objective. The field in the BFP has a top-hat intensity profile with the beam diameter limited by the lens aperture. Although the size of a focused spot theoretically extends infinitely, its practical area of influence is limited by the detector noise floor. Thus, we define the effective spot diameter as twice the maximum separation between the spot center and a scatterer, beyond which the generated signal falls below the detection threshold.

From the calculations detailed in Appendix C, the effective diameter of the focused spot is calculated to be 1.6 times the focused spot diameter. The value is a function of the noise floor of the measurement system including the electronic noise, laser intensity fluctuations, and the positioning uncertainty of the scanning stages. For an NA of 0.4 at 632.8 nm wavelength the effective spot diameter is then 2.954 µm. To ensure that there is no detectable cross-talk between the two adjacent beams, the inter-focal separation is set to be greater than this value by a safety factor of 10. The probability of cross-talk decreases as the separation increases, but larger separations can lead to higher optical aberrations for the beams at higher angles.

Additionally, sample thickness must also be considered, particularly for transparent samples or those with transparent layers. Cross-talk from sample thickness is negligible when thickness is less than the calculated depth of focus, which for our setup is 3.95 µm [7]. While highly reflective surfaces such as metals or Si wafers typically present no issues, transparent samples with lower reflectivity might require additional design modifications, such as increasing physical detector separation or incorporating a pinhole array ahead of the MLA.

4.2.2. BEAM SEPARATION AT THE DETECTOR

The position of the beams at the detector is crucial for obtaining consistent measurements. At the detector, each beam is incident exactly in the middle of two photodiodes such that when the beam is symmetric, the output signal is zero. The same target can result in different output signals depending on the offset of the beam with respect to this balanced position. Figure 4.3 shows the change in output signal when the beam is offset by different amounts with respect to the bi-cell. The output signals are numerically calculated for a pit with a diameter of 400 nm and depth of 150 nm etched in a Si substrate illuminated with a focus spot of 0.4 NA at a wavelength of 632.8 nm using the commercial FDTD solver, Lumerical. Offset errors can lead to misinterpretation of the collected data impacting the measurement quality. Thus, it is important that the beam separation at the detector matches the pitch of the detector array to within a few micrometers. While strict alignment tolerances are demanding, they ensure uniform output signals across all beams for identical targets.

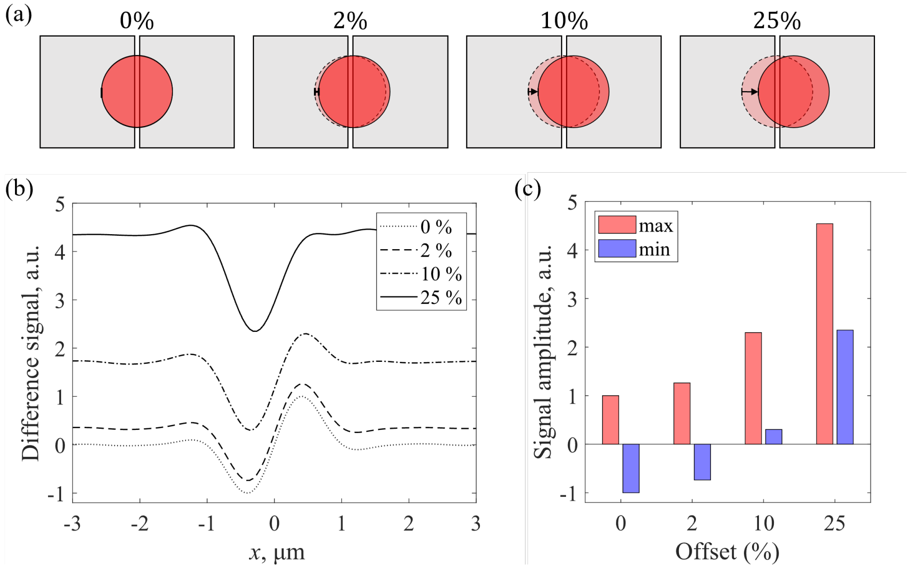

Figure 4.3: Influence of beam offset at detector on the difference signal. a) Schematic of different beam offsets at the detector. b) Difference signals from scans with different offsets. c) The maximum and minimum values of the difference signals. The signals are generated by simulating different offsets as a percentage of the beam diameter (detector size $\gg$ beam diameter). The scan signal was simulated for a sample consisting of a pit of 400 nm diameter and 150 nm depth etched in Si.

After addressing the detector alignment, it is essential to verify that each beam independently detects scatterers without cross-talk. This verification is detailed in the following section.

4.3. VERIFICATION OF INDEPENDENT DETECTION

Ensuring independent detection among beams is fundamental to the functioning of the parallel probe system. Initial experiments were performed to verify that the detection was independent across the beams, i.e. when one beam interacts with a target, the other two beams are not affected. A snapshot of the signal from the three beams is shown in Figure 4.4. The beams are arranged horizontally and allowed to scan over the surface of a Si wafer containing spherical polystyrene latex (PSL) particles. The scan range is 100 µm, scanned at a speed of 0.33 mm/s with a sampling rate of 50 kHz. The scan range is larger than the separation between the beams and the signals from the overlapping areas can be seen repeating across multiple beams. It is also evident that there is no discernible cross-talk between the beams.

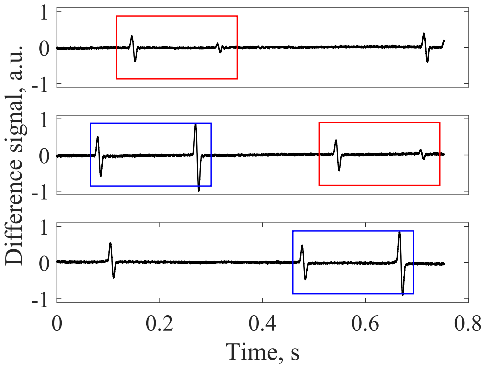

Figure 4.4: Differential signal from the detector array. The beams are arranged horizontally and scanned over PSL particles. The separation between two adjacent spots is 50 µm. The rectangles show repeating signals as adjacent beams scan the same region. The scan range for each beam is 100 µm. The signal is sampled at 50 kHz sampling rate.

Once independent detection is established, the next stage involves combining individual 2D data from each beam into a combined 2D plot, as explained in the following section on data stitching.

4.4. DATA STITCHING

Tiling scans from the different beams is implemented using phase-correlation algorithm [8]. The pseudocode for the algorithm is included in Algorithm 1. A slight overlap between individual beam scans is useful for accurate data stitching, particularly when exact beam separations are unknown. An example of the separate scans from each beam and the composite stitched image is shown in Figure 4.5. The sample consists of a Si wafer with etched structures. The scan area per beam is 100 µm x 100 µm. The separation between the lines is 200 nm. The scan speed for the fast axis is 0.33 mm/s. The sampling rate is 50 kHz. A minimum overlap of 15% between individual beam scans was required for stitching. While effective for sparse samples, the algorithm may require modifications for highly periodic targets, such as diffraction gratings.

Algorithm 1 Phase-Correlation Algorithm

```
    **Input:** $I_1$, $I_2$
    **Output:** (x, y): Translation coordinates
procedure PHASECORRELATION($I_1, I_2$)
    $F_1 \leftarrow \mathrm{FFT}(I_1)$                              ▷ 2D Fourier transform
    $F_2 \leftarrow \mathrm{FFT}(I_2)$
    $\mathrm{NCC} \leftarrow (F_1 .* \bar{F}_2) ./ \mathrm{abs}(F_1 .* \bar{F}_2)$   ▷ Calculate normalised cross-correlation
    $\mathrm{PCM} \leftarrow \mathrm{IFFT}(\mathrm{NCC})$                  ▷ Calculate phase-correlation matrix
    $(x, y) \leftarrow \mathrm{argmax}(\mathrm{PCM})$
end procedure
```

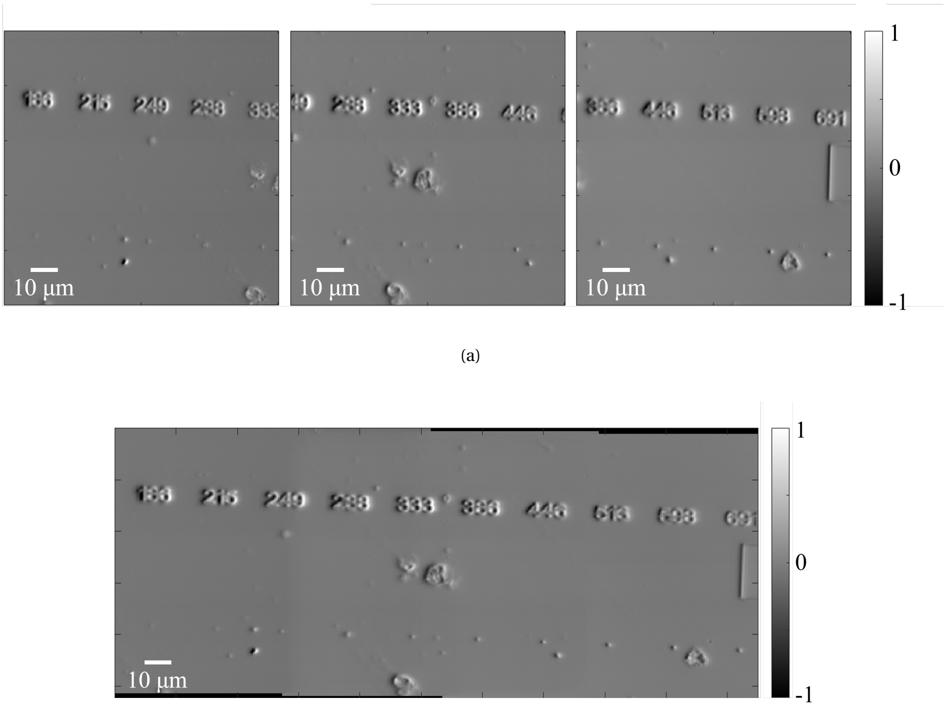

(a)

(b)

Figure 4.5: a) Scans from three independent beams before stitching. b) Composite scan after stitching using the phase-correlation algorithm. Scan parameters for each beam: scan area = 100 µm × 100 µm, scan speed (fast axis) = 0.33 mm/s, line separation in the y-direction = 200 nm, sampling rate = 50 kHz.

4.5. APPLICATION: CALIBRATION OF ETCHED PITS WITH DIFFERENT DIAMETERS

The setup was used to measure the signal from a sample of known characteristics for validation of the parallel scanning strategy. The measurement sample consists of an array of pits etched into a Si substrate. The pit diameters are exponentially distributed from 50 to 800 nm. The etch depth for all the structures is 150 nm. The separation between individual structures is 20 µm. A schematic of the sample is shown in Figure 4.6a. The signal strength corresponding to each pit is defined as the average of the absolute value of the maximum and minimum peaks of the signal. The scans were done at a speed of 0.3 mm/s and sampled at 50 kHz. Calibration measurements in Figure 4.6b show that the overall trend is identical across the three beams but is scaled due to the power difference across the three beams.

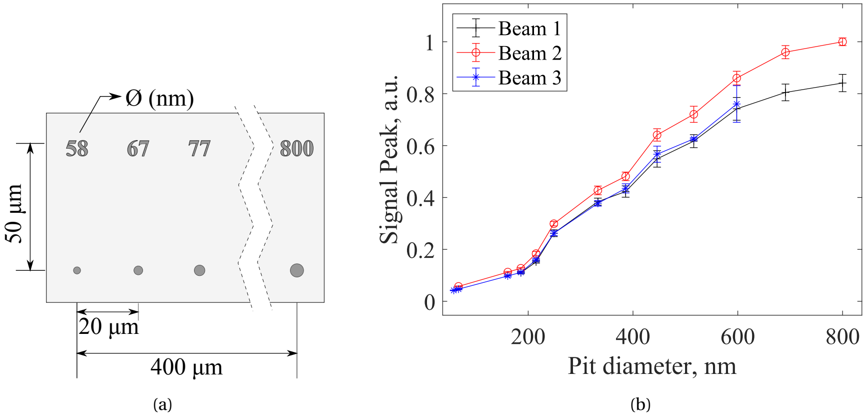

Figure 4.6: a) Sample schematic. The sample consists of an array of holes of diameters distributed exponentially from 50 to 800 nm etched on a Si wafer. The etch depth is 150 nm. b) Calibration curve for different beams. Scan is performed using 0.4 NA objective with 632.8 nm wavelength.

4.6. DISCUSSION

In summary, this chapter details a parallelised CFS setup using multiple beams. The detection was shown to be independent across the beams by scanning a Si wafer sample with 1 µm PSL particles. The output signal was measured to be identical for all the beams using a calibration target consisting of an array of pits of different diameters etched in Si. The peak signal amplitude varies across the beams due to the differences in the input beam power. A data stitching algorithm to generate a composite image from the individual scans has also been implemented. The total reduction in scan time for a specific scan area is proportional to the number of beams, 3 in this case.

The system can be scaled to use a higher number of beams generated using a 2D beam-splitter, a MLA, or an array of laser diodes combined with a 2D MLA and photodiode array for detection. The maximum number of spots would be limited by the higher field curvature and distortion for the beams at larger angles, equivalent to the field of view in microscopy. Other design variations to overcome this problem would include the use of a high-NA MLA to generate multiple spots on the sample instead of a single objective and a suitable telescopic system to relay the respective Fourier planes to the detector array.

Electronic complexity increases as the number of probes increases. The current scan speed is still limited by the use of piezo-based translation stages. This makes the system in its current design a few orders of magnitude slower than other commercial surface metrology tools such as dark-field microscopy or white-light interferometry. For even faster scan speeds, other forms of scanning such as using a galvo mirror, digital micromirror device or acousto-optic deflectors in place of the piezo-scanners can be investigated. These strategies are discussed in detail in the following chapters.

BIBLIOGRAPHY

[1] S. Soman, R. Horsten, T. Scholte, and S. Pereira, "Multi-beam coherent fourier scatterometry", *Measurement Science and Technology*, vol. 35, no. 7, p. 075 905, 2024. DOI: `https://doi.org/10.1088/1361-6501/ad3b2a`.

[2] D. B. Carlin, J. P. Bednarz, C. J. Kaiser, J. C. Connolly, and M. G. Harvey, "Multichannel optical recording using monolithic arrays of diode lasers", *Appl. Opt.*, vol. 23, no. 22, pp. 3994–4000, Nov. 1984. DOI: `https://doi.org/10.1364/AO.23.003994`.

[3] M. Ishihara and H. Sasaki, "High-speed surface measurement using a non-scanning multiple-beam confocal microscope", *Optical Engineering*, vol. 38, no. 6, pp. 1035–1040, 1999. DOI: `https://doi.org/10.1117/1.602155`.

[4] H. J. Tiziani and H.-M. Uhde, "Three-dimensional analysis by a microlens-array confocal arrangement", *Appl. Opt.*, vol. 33, no. 4, pp. 567–572, Feb. 1994. DOI: `https://doi.org/10.1364/AO.33.000567`.

[5] R. Katayama, K. Yoshihara, Y. Yamanaka, M. Tsunekane, K. Kubota, and K. Yoshida, "Multi-beam magneto-optical disk drive for parallel read/write operation", in *Optical Data Storage*, Optica Publishing Group, 1989, WA3. DOI: `https://doi.org/10.1364/ODS.1989.WA3`.

[6] A. L. Eberle, S. Mikula, R. Schalek, J. Lichtman, M. L. K. Tate, and D. Zeidler, "High-resolution, high-throughput imaging with a multibeam scanning electron microscope", *J Microsc.*, 2015. DOI: `https://doi.org/10.1111/jmi.12224.`.

[7] A. Egner, V. Andresen, and S. W. Hell, "Comparison of the axial resolution of practical Nipkow-disk confocal fluorescence microscopy with that of multifocal multiphoton microscopy: Theory and experiment", *Journal of Microscopy*, vol. 206, no. 1, pp. 24–32, 2002. DOI: `https://doi.org/10.1046/j.1365-2818.2002.01001.x`.

[8] S. Preibisch, S. Saalfeld, and P. Tomancak, "Globally optimal stitching of tiled 3D microscopic image acquisitions", *Bioinformatics*, 2009. DOI: `https://doi.org/10.1093/bioinformatics/btp184`.

5

GALVO-BASED COHERENT FOURIER SCATTEROMETRY

This chapter investigates the implementation of a galvo mirror for rapid beam scanning in a coherent Fourier scatterometry (CFS) system. The chapter examines key considerations such as off-axis aberrations and angle-dependent beam shifts introduced by the galvo mirror, and proposes alignment strategies to mitigate their effects. Experimental measurements using a Shack-Hartmann wavefront sensor are used to characterise aberrations across scan angles, and the impact on measurement signal quality is evaluated. The system performance is validated through the measurement of calibrated targets, and a detailed uncertainty analysis is presented to quantify the contributions from optical and electronic sources.

Parts of this chapter have been published in Measurement **258**, 119294 (2026) [1].

In chapter 4, a parallelised scanning approach was used to reduce the scanning time required for a given inspection area. This reduction was directly proportional to the number of beams used. However, the scanning mechanism continued to rely on piezo-based stages, limiting further improvements in scanning speed. To achieve further increases in scan speed, alternative mechanical scanning systems must be considered.

This chapter explores the use of a galvo mirror for rapid beam scanning in a CFS setup. Galvo mirrors offer precise and high-speed beam positioning and are commonly used in fields such as laser cutting, LIDAR, and microscopy to facilitate rapid and controlled beam movement [2]–[5]. The galvo mirror investigated here replaces the piezo stage previously used for fast-axis scanning, significantly reducing the total scanning time.

Several factors must be addressed when integrating a galvo mirror into a CFS setup. A notable drawback of employing galvo mirrors as pre-objective beam scanners is the introduction of off-axis beam aberrations [6]. This inherent limitation can only be mitigated through the use of well-corrected objective lenses or other compensation techniques [7], [8]. In addition to the optical aberrations, there can also be an angle-dependent beam shift at the detector [9], [10]. To limit the influence of optical aberrations, the acceptable angular range of the galvo mirror is experimentally determined based on the cumulative impact of various aberrations on the measured signal. Regarding beam shifts at the detector, the beam offset at the detector is calculated as a function of the galvo mirror position, and an alignment protocol is designed to minimise these offsets in the setup.

Finally, the application and performance of the galvo-based CFS system are demonstrated through the calibration of etched pits of varying diameters in a silicon wafer. Additionally, the chapter includes a comprehensive analysis of measurement uncertainty contributions from various system components.

5.1. EXPERIMENTAL SETUP

The schematic of the setup is shown in Figure 5.1a. The laser beam from a 632.8 nm HeNe laser is expanded using lenses L1 ($f = 10$ mm) and L2 ($f = 250$ mm) in a telescopic arrangement. The expanded beam is scanned using a single-axis galvo mirror (GVS211/M, Thorlabs), M2, driven by a sinusoidal signal with maximum frequency of 1 kHz. The beam reflected from M2 is relayed to the back focal plane (BFP) of the objective using lenses L3 (LSM03-VIS, Thorlabs) and L4 (TTL165-A, Thorlabs) also in a telescopic arrangement. The objective (N PLAN L 20x/0,40 NA, Leica) focuses the beam on the sample. The laser power at the focal plane was measured to be 68 µW.

The light after reflection from the sample is captured by the same objective and demagnified using lenses L5 ($f = 275$ mm) and L6 ($f = 40$ mm) in yet another telescopic arrangement. The lens pair relays the demagnified beam to the middle of the differential detector. The detector consists of a bi-cell photodiode (SD 113-24-21-021). Lenses L5 and L7 ($f = 100$ mm) are used similarly to demagnify and relay the reflected beam to a CCD camera. A flipping mirror, M3, is used to switch between the detector and camera arm. The camera is used only to locate areas of interest on the sample.

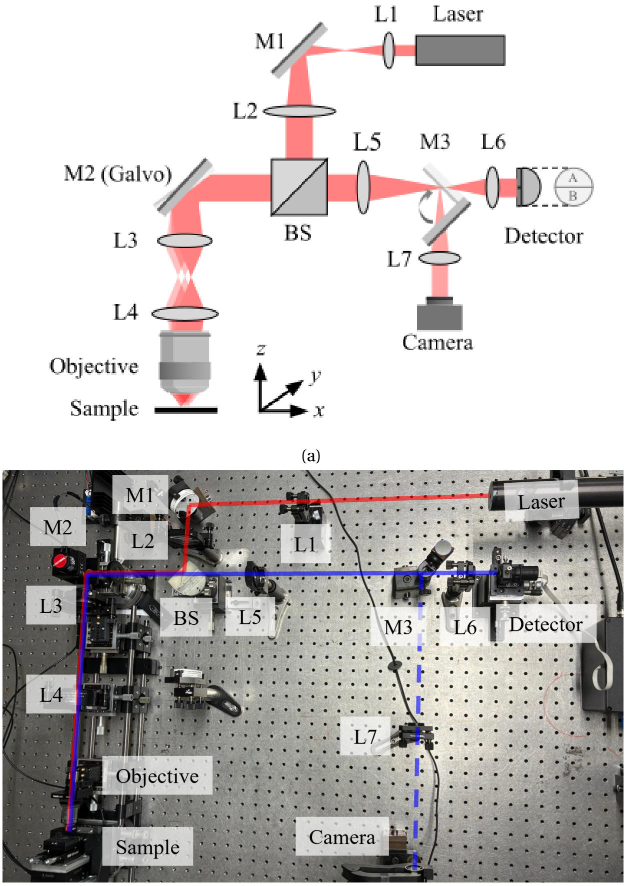

(a)

(b)

Figure 5.1: a) Schematic of the optical setup, b) photo of the setup on the optical table: red lines indicate the light path to the sample and blue the path of the light after reflection from the sample to the detector. Dotted blue line indicates the reflected path to the camera. Lenses L1 - 10 mm, L2 - 250 mm, L3 - scan lens (LSM03-VIS, Thorlabs), L4 - tube lens (TTL165-A, Thorlabs), L5 - 275 mm, L6 - 40 mm, and L7 - 100 mm. Obj - 0.4 NA (N PLAN L 20x/0,40, Leica) objective lens, BS - beam splitter, M1 - mirror to fold light path, M2 - galvo mirror (GVS211/M, Thorlabs), M3 - flipping mirror to switch between camera and split-detection path, laser - 632.8 nm HeNe.

5.1.1. SCANNING AND SYNCHRONISATION

The sample is raster-scanned in 2D using the galvo mirror in the fast axis (x) and a piezo stage (P-625 CD, Physik Instrumente) for the slow axis (y). The galvo mirror is driven using a sinusoidal wave of amplitude V_0 and frequency f. The amplitude determines the width of the scan in the x-direction. The galvo angle is related to the applied voltage as 0.5 V/deg. The extent in the y-direction is limited by the piezo range to 500 µm. The piezo stage is controlled such that the piezo in the slow-axis steps by Δy after one period of the galvo oscillation. An additional piezo stage (PI-753.3, Physik Instrumente) is used for fine focus adjustments along the z-axis. There are also manual translational stages in three axes for coarse alignment.

Both the galvo mirror and the y-piezo stage have different in-built sensors that can provide positional information for feedback. The difference signal along with the feedback signals are recorded using an ADC (NI 5734, National Instruments). These feedback signals are used to assign x and y-coordinate information to the difference signal enabling us to create a 2D differential scattering map. Figure 5.2 shows an example of the different feedback signals of the galvo mirror and the y-piezo translator along with the difference signal as a function of time. The scan parameters for this example are: V_0 - 800 mV, f - 100 Hz, Δy - 100 nm, sampling rate - 1 MHz. The measurement sample consists of a Si wafer with PSL (polystyrene latex) particles of 400 nm diameter.

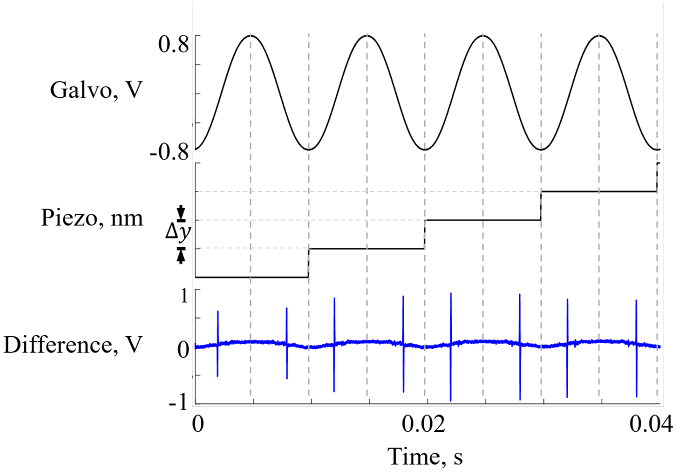

Figure 5.2: Voltage signals recorded from multiple channels: Galvo - feedback signal from the galvo mirror (x-axis), Piezo - feedback from the piezo used in the slow axis (y-axis), Difference - signal from the split-detector obtained by subtracting the output signals from the two photodiodes and normalised. The dotted lines are used to separate each scan line. The scan parameters used were: galvo frequency - 100 Hz, galvo amplitude - 800 mV, line separation - 100 nm, all signals sampled at 1 MHz. The sample consists of a Si wafer with 400 nm PSL (polystyrene latex) particles.

5.2. INFLUENCE OF THE GALVO MIRROR POSITION

There are two main considerations when choosing the position of the galvo mirror within the setup: 1. After the deflection from the galvo mirror, the light after reflection from the sample must be de-scanned so that the light beam remains parallel to the optical axis, 2. the position of the beam should not change relative to the difference detector.

The first issue can be solved by having the galvo mirror positioned along the common optical path shared by both the incident and reflected beams. This configuration allows the galvo mirror to perform both scanning and de-scanning functions. When the galvo mirror rotates by an angle θ about its axis, it deflects the incident beam by an angle 2θ relative to the optical axis (see Figure Figure D.1 in Appendix D). After interacting with the sample, the reflected beam travels back toward the galvo mirror at an angle of -2θ with respect to the optical axis. The galvo mirror then introduces an additional 2θ deflection in the reflected path, realigning the beam to be parallel to the optical axis. Thus, by being located in the shared path of both incident and reflected beams, the galvo mirror effectively cancels out its initial deflection in the return path.

For the second issue, let us first calculate the beam shift analytically using the Fourier transforming property of an objective lens. The BFP is related to the image plane by a Fourier transformation. The tilts in the BFP are transformed to shifts in the image plane. We use this property to scan the focused spot across the sample in the image plane. If the galvo mirror is not placed in the BFP conjugate plane, the beam in the BFP gets shifted in addition to the tilt from the mirror. The shift at the BFP after extrapolation is calculated to be,

$$\delta = (dz + d\tan\theta)\tan 2\theta, \tag{5.1}$$

where θ is the angle of rotation of the galvo mirror, dz is the distance from the rotational axis of the galvo mirror to the BFP, and d is the distance from the rotational axis to the point of incidence of the beam on the galvo mirror, measured along the optical axis. A schematic of the beam shift is shown in Figure 5.3a. The detailed calculations are included in Appendix D. The beam at the BFP thus has a shift of δ and tilt of 2θ with respect to the optical axis.

At the image plane, in addition to the shift caused by the beam tilt in the BFP, the beam is also tilted by an angle α, a function of the shift in the BFP. After reflection from the sample, the angle changes from α to $-\alpha$. The field in the BFP, after Fourier transformation, is then shifted by $-\delta$.

The lateral shift is demagnified by lenses L5 and L6, which relay the BFP to the differential detector. The beam position at the detector is thus shifted if the galvo mirror is shifted from the BFP. When the beam is shifted with respect to the middle of the detector, left and right halves of the bi-cell have unequal amounts of light incident on them. The shift thus creates an asymmetry causing the differential detector to act as a position sensor. Since the shift is a function of the galvo angle, the signal generated due to the shift follows the galvo motion with the same frequency and with an amplitude proportional to δ. If g(t) is the signal generated from the beam shift and d(t) is the differential signal from the sample scan, the total output signal is, s(t) = g(t) + d(t). The contribution from the beam shift, g(t), is minimised when the galvo is in the BFP. Figure 5.3b and Figure 5.3c show the output signal from the detector when the galvo mirror is placed at the BFP and slightly shifted from the BFP, respectively.

Furthermore, the shift can also introduce vignetting unless the beam diameter is significantly larger than the exit pupil diameter. However, increasing the beam diameter beyond the exit pupil diameter results in poor utilisation of the laser power.

Thus, the galvo mirror is placed in a plane conjugate to the BFP of the objective and in a double-pass configuration. This ensures the beam at the split-detector is neither tilted nor shifted. In the next section, the more fundamental issue of off-axis aberrations is tackled.

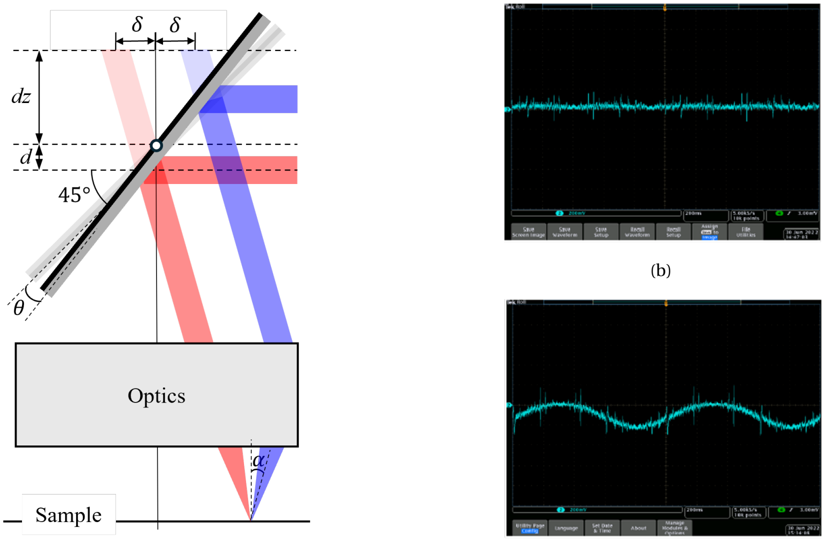

(a)

(b)

(c)

Figure 5.3: a) Schematic illustration of a beam shift at the back focal plane (BFP) due to the displacement of the galvo mirror from the ideal BFP position (red - incident beam, blue - reflected beam, solid black line - optical axis), where δ is the shift of the beam after reflection with respect to the optical axis, dz is the distance between the BFP and the rotational axis of the galvo mirror, d is the distance from the rotational axis to the point of incidence of the beam on the galvo mirror. Screenshot of the differential signal from the detector generated with the galvo mirror b) positioned exactly at the BFP and c) slightly shifted from the BFP.

5.3. OFF-AXIS ABERRATIONS

As the galvo mirror scans the beam through a range of angles, the optical path varies slightly for each angle. Depending on the optical path, the beam experiences different aberrations. To quantify the change in aberrations for different beam angles, a Shack-Hartmann wavefront sensor (SHSCam SHR-150-CL, Optocraft) was used to experimentally measure the amount of optical aberrations in the far field. The aberrations are described using Zernike polynomials. In theory, any general wavefront defined on a circular pupil can be decomposed in terms of Zernike polynomials as [11]:

$$W(\rho,\varphi) = \sum_{n,m} C_n^m Z_n^m(\rho,\varphi) \tag{5.2}$$

where, C_n^m is the coefficient corresponding to each Zernike polynomial Z_n^m in the decomposition of the general wavefront W. Each polynomial is defined on a unit circle with $0 \le \rho \le 1$, $0 \le \varphi \le 2\pi$ and

$$Z_n^m(\rho,\varphi) = R_n^m(\rho) \cdot \left\{ \begin{array}{ll} \cos m\varphi & m \ge 0 \\ \sin m\varphi & m < 0 \end{array} \right\} \tag{5.3}$$

The radial function $R_n^m(\rho)$ is defined as,

$$R_n^m(\rho) = \sum_{k=0}^{(n-m)/2} (-1)^k \frac{(n-k)!}{k!(\frac{n+m}{2}-k)!(\frac{n-m}{2}-k)!} \rho^{n-2k}. \tag{5.4}$$

where, $n = 0,1,2$, etc. is the radial index and $m = -n, -n+2, ..., n-2, n$ is the azimuthal index.

During the measurements, the beam angle was varied from −10° to +10°. These angles correspond to twice the galvo mirror angles. Beyond this range, the beams suffered from clipping due to the finite aperture size of the scan lens. The aberrations were measured in the back focal plane of the objective before the beam is focused on the sample. For each angle, only the low-order Zernike aberrations were measured, namely, defocus, spherical, astigmatism, oblique astigmatism, horizontal and vertical coma aberrations. The wavefront sensor measures the coefficient corresponding to each aberration in units of wavelength of the incident light. Figure 5.4 shows the plots for the amounts of different aberrations as a function of the beam angle. Astigmatism, oblique astigmatism, and vertical coma exhibit the most variation with the beam angle. This is logical, as one of the primary contributors to astigmatism in an optical system is the presence of off-axis beams. The larger the off-axis angle, the greater the asymmetry in the wavefront, resulting in more pronounced non-axisymmetric aberrations such as astigmatism and coma.

Next, the combined influence of these aberrations on the peak-to-peak voltage of the difference signal was studied. For this study, the galvo is held fixed at a certain angle using a DC voltage while the sample is scanned using a 2D piezo stage (P-625.2 CD). A 2D scan map using the piezo stage with the galvo mirror at 0° is shown in Figure 5.5b. The sample consisted of an array of 90 pits etched into a silicon wafer. Each pit has a nominal diameter and etch depth of 200 nm and 150 nm respectively. There might be small variations in the actual values due to the fabrication process. To study the variation in the peak-to-peak voltage as a function of the galvo angle, the peak-to-peak voltages are averaged across all the pits. The scan parameters were: x-speed - 500 µm/s, Δy - 200 nm, sampling rate - 50 kHz. Figure 5.5a shows the variation in the signal peak-to-peak as a function of the galvo angle. The signal peak is highest at 0° and reduces for larger angles. The asymmetry observed around 0° is likely due to a misalignment of one or more components in the optical setup. For angles of ±1.6°, the mean signal remains within 90% of the peak value measured at 0°. Beyond these angles, it is advisable to apply post-processing corrections to account for the signal reduction. It is worth mentioning that

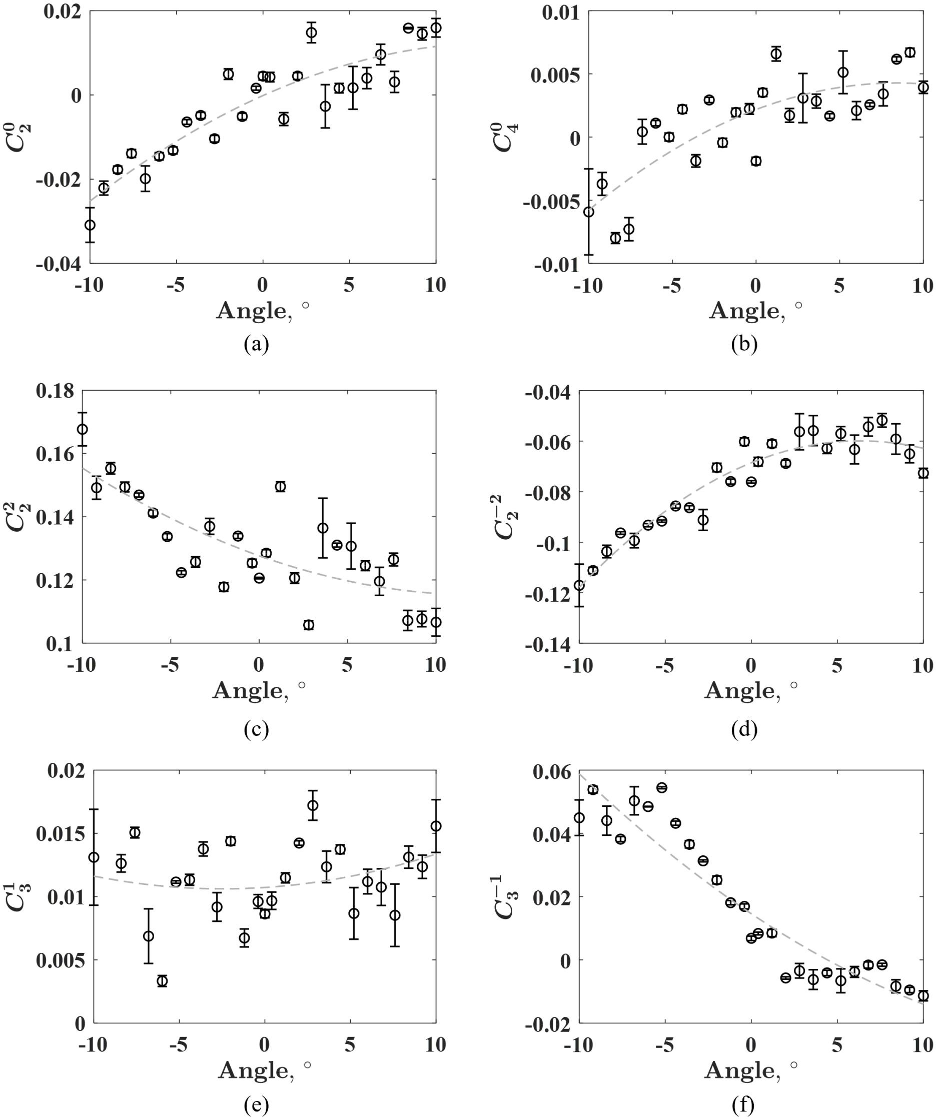

(a) (b)

(c) (d)

(e) (f)

Figure 5.4: Zernike coefficients as a function of the beam angle for a) defocus, b) spherical, c) astigmatism, d) oblique astigmatism, e) horizontal coma, f) vertical coma aberrations. The coefficients were measured using a Shack-Hartmann wavefront sensor (SHSCam SHR-150-CL, Optocraft) in the back focal plane. Each data point is an average of five independent measurements with a coverage factor, $k = 1$.

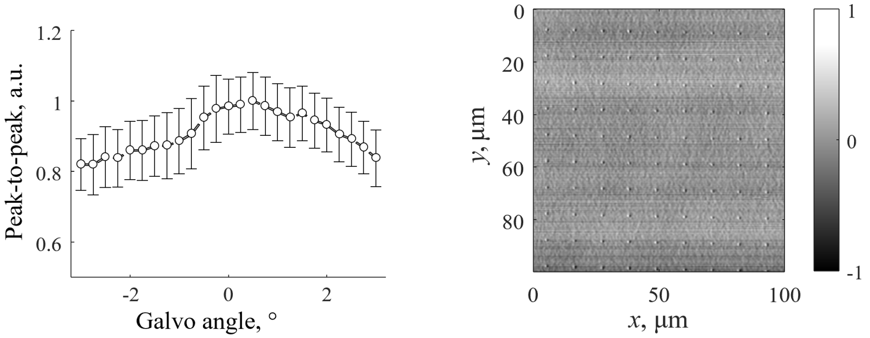

(a) (b)

Figure 5.5: a) Peak-to-peak of the differential signal corresponding to the detection of one pit plotted as a function of galvo mirror angle. b) The 2D differential scattering map, obtained using a 2D piezo stage, of an array of circular pits of 200 nm diameter and etched to a depth of 150 nm in silicon at a galvo angle of 0°. Each data point in (a) is an average (coverage factor, $k = 1$) of the peak-to-peaks for the entire array with each pit measured twice.

this range of acceptable angles is determined uniquely for the optical system detailed in Figure 5.1 and may differ depending on the optical components used.

We now have an optical system with specific ranges of scan parameters that have been experimentally defined. The next step is to evaluate the system requirements for high-speed scanning, focusing specifically on the minimum bandwidth needed for the detector to accurately track the optical signal.

5.4. APPLICATION: CALIBRATION OF ETCHED PITS WITH DIFFERENT DIAMETERS

The performance of the CFS setup with the galvo mirror is evaluated by using the setup to create a calibration curve for etched circular pits with varying diameters. The calibration sample consisted of an array of circular pits etched into a Si substrate, with diameters ranging uniformly from 325 nm to 925 nm in 100 nm increments and a constant depth of 150 nm. The pits were spaced 10 µm apart and fabricated using e-beam lithography followed by dry etching. The scan parameters were: f_{galvo} - 10 Hz, Δy - 200 nm, sampling rate - 1 MHz. The resulting calibration curve, shown in Figure 5.6, plots the peak-to-peak signal as a function of the pit diameter. Each data point is an average of 12 independent measurements with a coverage factor of $k = 1$. This curve demonstrates the system's ability to correlate the measured signal with specific pit sizes. The calibration curve can then be used to infer pit diameters within this range, or to measure deviations from a nominal diameter value during the manufacturing process.

5.5. UNCERTAINTY ASSESSMENT

In CFS, the asymmetry in the far-field generated while scanning a focused spot across a sample is converted from an optical signal to an electronic signal using photo-detectors

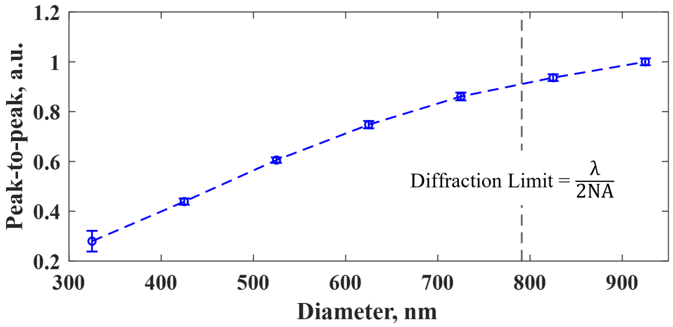

Figure 5.6: Peak-to-peak of the differential signal plotted as a function of the etched hole diameter. The system uses a 0.4 NA objective and laser source of 632.8 nm.

and amplifying circuits. In earlier sections, the contribution of the optical aberrations to the measurement uncertainty was discussed. Apart from these systematic errors, the primary sources of uncertainty include noise from the detection circuit and ADC (analog-to-digital converter), laser power fluctuations, substrate surface roughness, and vibrations from mechanical or environmental components. All measurements were conducted at a controlled temperature of 21°C with fluctuations limited to 0.1°C. The contribution to measurement uncertainty due to thermal expansions is assumed to be minimal. The contributions of various uncertainty sources, expressed as fractions of the ADC's maximum input signal of 2V_{pp} are reviewed below. The power at the sample is measured to be 68 µW.

The uncertainty contributions from different sources are as follows:

1. **ADC**. The noise from the ADC can be classified into two parts: quantisation and thermal noise. The root mean square (RMS) quantisation noise is 8.8 µV [12]. The RMS value of the thermal noise measured by shorting the input channels is 197.6 µV.

2. **Detector**. The noise from the detector measured when no light is incident on the photodiodes is 881.4 µV, given a measured detection bandwidth of 560 kHz.

3. **Laser**. The peak-to-peak of the difference signal varies linearly as a function of input laser power. Any fluctuations in the laser intensity can thus directly influence the output signal. The HeNe laser has low-frequency power fluctuations and has minimal influence if the measurement lasts only for a few seconds. However, for longer measurements using an intensity-stabilised laser would be preferred. The RMS noise contribution due to the laser fluctuation for a 5-minute measurement is 1.342 mV. The measurement was done two hours after the laser is switched on.

4. **Piezo**. The z-piezo is used for positioning the sample in the right plane to get the maximum peak-to-peak signal. The peak-to-peak drops as a function of distance from the optimal plane. Positioning inaccuracies of the piezo system can lead to a shift of the sample position from this optimal measurement plane contributing to

measurement uncertainties. The positioning error for the z-stage was measured using the built-in sensor used for closed-loop feedback. The standard deviation of the positioning error set at half its travel range, i.e. 19 µm is 0.11 nm. The effect of such a small displacement cannot be measured experimentally using the current setup. The contribution to the measurement uncertainty from the z-stage can thus be entirely neglected.

5. **Galvo mirror**. The contribution from the galvo mirror was measured by repeatedly scanning the same line on a sample. The focus spot was first centred on a nanoparticle on the sample and several line scans were made using the galvo mirror. Any wobble or other galvo errors cause deviations in the peak-to-peak signal. Assuming other errors listed above are independent, the error in the galvo motion introduces an uncertainty of 2.422 mV.

6. **Surface roughness**. Surface roughness does not contribute directly to the noise floor of the detection but it does raise the background signal level considerably. Especially for particle detection, it often limits the size of the smallest detectable particle [13]. For a blank single-side polished Si wafer with $h_{\mathrm{RMS}} < 0.5$ nm, the RMS value for the difference signal is 1.605 mV.

The above error sources, with the exception of surface roughness, are both uncorrelated and sample-independent. Sample roughness varies with the sample and cannot be generalised. The sample-independent combined standard uncertainty (with coverage factor $k = 1$) in the peak-to-peak signal is 2.788 mV. Photon shot noise can be neglected in the present measurement regime because the corresponding shot-noise-limited fluctuation at the detector output is orders of magnitude smaller than the other error source due to the large relatively large input power.

5.6. DISCUSSION

In this chapter, a novel beam-scanning CFS system employing a 1D galvo mirror for high-throughput metrology applications is presented. The impact of the galvo mirror position relative to the Fourier plane is examined, alongside the effects of beam angle on the peak-to-peak signal obtained from sub-wavelength nanostructures. Optical aberrations are shown to decrease the peak-to-peak signal and distort the optical impulse response of the system, with off-axis beams experiencing significantly greater aberrations compared to on-axis beams. In practice, this limits the range of angles that can be used for scanning. In the current setup using a 0.4 NA objective, the signal peak-to-peak drops to 90% for galvo angles ±1.6°.

Previous CFS configurations using piezo-based scanning stages for both x and y-axes required approximately 300 ms per 100 µm line, leading to a total scan duration of around 5 minutes for an area of 100 µm × 100 µm, using steps of 0.1 µm in the y-direction. Using a galvo mirror for identical scan parameters, this total scan time is reduced significantly to about 1 s.

BIBLIOGRAPHY

[1] S. Soman, R. C. Horsten, and S. F. Pereira, “High-speed coherent fourier scatterometry: Galvo mirror integration for fast surface inspection”, *Measurement*, vol. 258, p. 119 294, 2026, ISSN: 0263-2241. DOI: https://doi.org/10.1016/j.measurement.2025.119294.

[2] C. J. Sheppard, “Scanning confocal microscopy”, *Encyclopedia of Optical Engineering*, pp. 2525–2544, 2003. DOI: https://doi.org/10.1081/E-EOE120009630.

[3] C. Leone, S. Genna, and V. Tagliaferri, “Fibre laser cutting of CFRP thin sheets by multi-passes scan technique”, *Optics and Lasers in Engineering*, vol. 53, pp. 43–50, 2014, ISSN: 0143-8166. DOI: https://doi.org/10.1016/j.optlaseng.2013.07.027.

[4] X. T. Nguyen, V. L. Dinh, H.-J. Lee, and H. Kim, “A high-definition lidar system based on two-mirror deflection scanners”, *IEEE Sensors Journal*, vol. 18, no. 2, pp. 559–568, 2018. DOI: https://doi.org/10.1109/JSEN.2017.2777500.

[5] V.-F. Duma, K.-S. Lee, P. Meemon, and J. P. Rolland, “Experimental investigations of the scanning functions of galvanometer-based scanners with applications in OCT”, *Appl. Opt.*, vol. 50, no. 29, pp. 5735–5749, Oct. 2011. DOI: https://doi.org/10.1364/AO.50.005735.

[6] J. Montagu, *Handbook of optical and laser scanning*. CRC Press Boca Raton, FL, USA, 2016, ch. Galvanometric and resonant scanners, pp. 418–473. DOI: https://doi.org/10.1201/9781315218243.

[7] P. E. Verboven, “Distortion correction formulas for pre-objective dual galvanometer laser scanning”, *Applied optics*, vol. 27, no. 20, pp. 4172–4173, 1988. DOI: https://doi.org/10.1364/AO.27.004172.

[8] J. S. Ehrmann, “Optics for vector scanning”, in *Beam Deflection and Scanning Technologies*, L. Beiser and G. F. Marshall, Eds., International Society for Optics and Photonics, vol. 1454, SPIE, 1991, pp. 245–256. DOI: 10.1117/12.28036. [Online]. Available: https://doi.org/10.1117/12.28036.

[9] K. Carlsson, “Scanning and detection techniques used in a confocal scanning laser microscope”, *Journal of Microscopy*, vol. 157, no. 1, pp. 21–27, 1990. DOI: https://doi.org/10.1111/j.1365-2818.1990.tb02943.x.

[10] M. Kumar and Y. Kozorovitskiy, “Tilt-invariant scanned oblique plane illumination microscopy for large-scale volumetric imaging”, *Opt. Lett.*, vol. 44, no. 7, pp. 1706–1709, Apr. 2019. DOI: https://doi.org/10.1364/OL.44.001706.

[11] ISO 21457:2008(E), “Ophthalmic optics and instruments — Reporting aberrations of the human eye”, International Organization for Standardization, Standard, 2008.

[12] S. W. Smith, *The scientist and engineer's guide to digital signal processing*. USA: California Technical Publishing, 1997, ISBN: 0966017633.

[13] D. Kolenov, I. E. Zadeh, R. C. Horsten, and S. F. Pereira, “Direct detection of polystyrene equivalent nanoparticles with a diameter of 21 nm using coherent fourier scatterometry”, *Opt. Express*, vol. 29, no. 11, pp. 16 487–16 505, May 2021. DOI: `https://doi.org/10.1364/OE.421145`.

6

ROTATION-BASED COHERENT FOURIER SCATTEROMETRY

A rotation-based CFS system is presented, replacing fast-axis piezo scanning with continuous rotation for improved throughput. A frequency-spread minimisation technique is introduced to correct probe centering without reference structures. Axial wobble is quantified using depth-dependent signal variations, achieving sub-micrometer precision. The system demonstrates high-resolution, high-speed metrology suitable for nanostructure calibration and contamination detection.

Parts of this chapter have been published in Optical Engineering **64**, 074106 (2025) [1].

Raster scanning traditionally employs two piezo-stages: one along the fast-axis and another along the slow-axis to create a 2D map. The piezo stage along the fast-axis, following a triangular waveform, must accelerate, decelerate and reverse the motion for each line, while the slow-axis stage moves incrementally following a staircase or slow ramp signal [2]. This repeated start-stop motion limits scan speed and throughput. Each reversal requires settling time, slowing the process for large-area scans [2]. High speeds can also excite mechanical resonances in the system, causing vibrations that reduce positional accuracy [3]. To avoid this, systems must operate below resonance limits, further reducing speed.

Rotational scanning avoids these problems by using a rotation stage that moves at constant angular velocity [4]–[7]. This eliminates the start–stop motion and the associated vibration shocks, while vibrations due to the rotation itself can still be present. In the proposed solution, the fast-axis motion is replaced by the rotation stage, while the slow-axis is handled by a piezo stage stepping outward in concentric circles. The result is smoother motion, higher scan speeds, and better throughput. Additionally, this approach is cost-effective and simplifies the control system while being able to scan large areas with high resolution. In this setup, we use a staircase waveform for the slow-axis motion leading to a concentric circle scan pattern. Using a slow ramp signal instead generates a spiral scan pattern.

Despite its advantages, rotational scanning presents new challenges. One of the primary concerns is the centering deviation of the probe [8]–[11]. When the probe, i.e., the focused spot, is misaligned with respect to the rotational axis of the stage, it introduces distortions in the reconstructed scan. To address this, a simple and general solution to minimise this deviation without requiring additional sensors or calibrated targets is proposed. The method uses the spread in the frequency spectrum of the scan signal at different radial distances to minimise the centering error.

Non-uniform sampling is another potential challenge. Scanning speed increases as a linear function of the scan radius. This means that, at constant sampling frequency, as the scan radius increases, the sampling becomes increasingly sparse and can also influence the measurement accuracy. Possible solutions are either to vary the angular velocity of the rotation stage inversely with the scan radius or to adaptively increase the sampling rate. For the limited scanning range in our setup, neither option was necessary, and both the sampling rate and the angular velocity were kept fixed. However, for larger radial distances, different solutions should be implemented.

Finally, the error motions of the rotation stage can also introduce challenges. The axial and radial runout errors of the rotation stage can distort the sample scan signal [12]–[14]. Depending on the mechanical precision of the rotating stage, additional servos might be required to compensate focusing and tracking errors [15]. This was not considered necessary for the rotation stage used in our setup. Nonetheless, we detail a method to estimate the axial wobble of the system using the CFS scan signal.

6.1. EXPERIMENTAL SETUP

The experimental setup is shown in Figure 6.1. The CFS scan head consists of the following: laser (FP-D-635-1P-C-C, Laser Components) generating 1 mW, 635 nm wavelength collimated light, lens L1, an aspheric lens of 0.65 NA with focal length of 2 mm and lens

L2 with focal length of 25 mm. Beam splitters BS1 and BS2. Split detector SD, consisting of a bi-cell (SD 113-24-21-021) for generating the difference signal, and CCD camera for localising areas of interest. The collimated light from the laser is focused on the sample using L1. The scattered light after reflection is captured using the same lens. L2 images the Fourier plane or the back focal plane of lens L1 onto the detector. BS2 splits the reflected light onto a camera and a split detector.

The entire setup is enclosed in a custom-made, 3D-printed housing and mounted on a piezo x-y-z translator (P-611.3S NanoCube, Physik Instrumente) for slow-axis movements and focus positioning. There are additional manual translators for coarse adjustments. The rotating stage (Precilec 36SMOP-17, VDL) is a DC torque motor controlled by an external voltage supply.

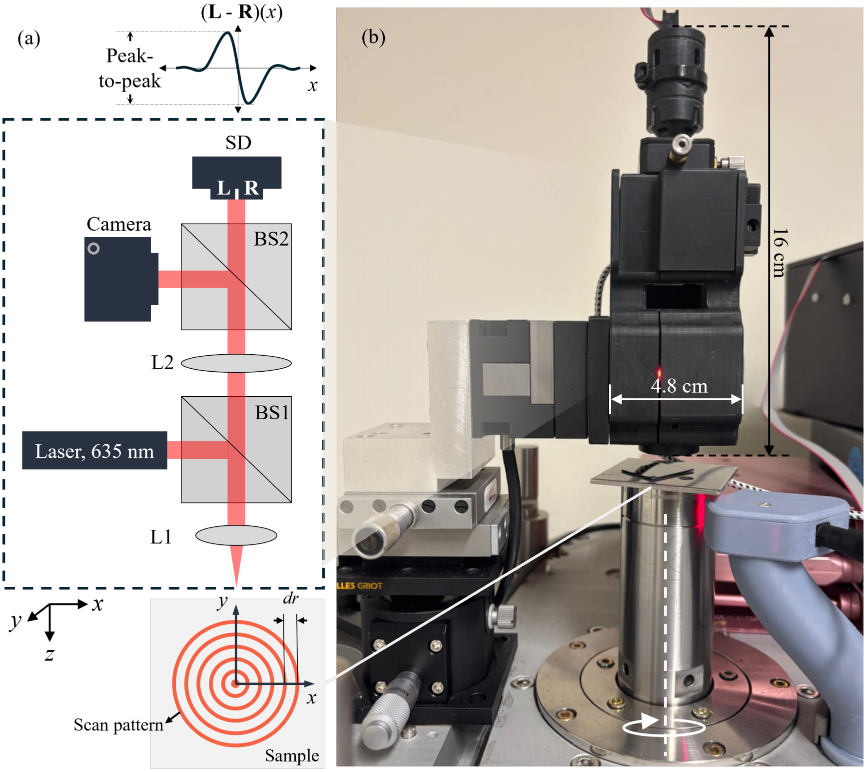

Figure 6.1: a) Schematic of the CFS setup used for scanning with L1, L2 - lenses with 2 mm and 25 mm focal lengths respectively, BS1, BS2 - beam-splitters, SD - split-detector, 635 nm laser and a camera to localise areas of interest on the sample. b) Photo of the setup on the optical table.

6.1.1. SCANNING AND SYNCHRONISATION

The sample is scanned using a combination of the rotation stage and the x or y piezo translator. The sample is mounted on the rotation stage, which rotates continuously at a frequency of f_{rotation}. The CFS scan head is moved radially using the piezo translator.

The resulting scan pattern consists of concentric circles with increasing radii. The piezo stage steps by a predefined amount, $dr <$ spot size, as the rotation stage completes one rotation or after every $1/f_{\text{rotation}}$ seconds.

Due to the absence of a rotation stage encoder, a simplified rotation counter was built to synchronise the piezo stage with the rotation cycles. The rotation sensor consists of a laser, photodiode, and a scattering object fixed on the rotating cylinder. As the scattering object passes through the laser beam, it reduces the reflected light received by the photodiode, creating dips in the recorded signal. These dips are used as markers to count rotation. Figure 6.2a shows an example of the rotation sensor, piezo (x-axis) and difference signals acquired during a sample scan (1 µm polystyrene latex (PSL) particle on Si). The dips from the rotation sensor are used to trigger the piezo to step in the radial direction while the difference signal is acquired continuously. The split-detector, rotation sensor and piezo feedback data are digitised by a data acquisition card (NI 9222, National Instruments) and recorded by the computer.

Figure 6.2b shows a schematic of the signal generation during the scanning of a particle on a flat substrate. The red lines follow the scan lines across the sample surface. The difference signal plotted in black illustrates the variation in peak-to-peak amplitude of the difference signal as a function of the offset between the particle centre and scan line. A similar trend can also be seen in the example difference signal shown in Figure 6.2a.

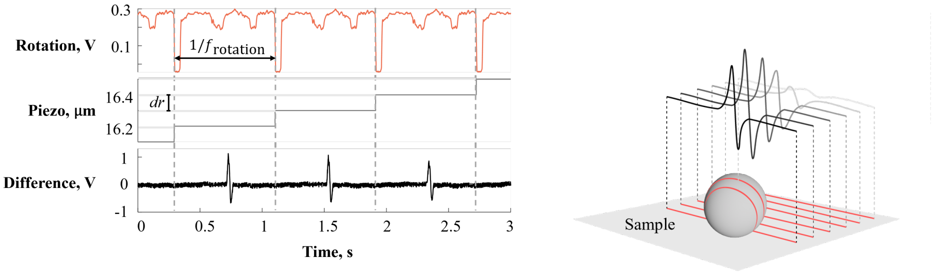

(a) (b)

Figure 6.2: a) Data recorded from multiple channels during a typical sample scan: rotation - data from the rotation sensor with the dips denoting the completion of one rotation, piezo - feedback signal from the in-built position sensor, difference - difference signal generated using the split-detector. Dotted lines are used to denote different rotations. The scan parameters are: $f_{\text{rotation}} = 1.23$ Hz, $dr = 0.1$ µm. The sample consists of a Si wafer with 1 µm PSL particles. b) Schematic of the scanning process over a particle: red lines indicate scan paths; black traces show corresponding difference signals.

6.2. SURFACE TOPOGRAPHY RECONSTRUCTION

Feedback signals, generated by the rotation sensor and piezo-stage, provide real-time positional data that correlates the scanned signal to specific sample locations. The information on the radial coordinate is given by the piezo feedback and the azimuthal position is calculated from the rotation counter sensor. Assuming uniform sampling, the azimuthal position of i^{th} data sample is $2\pi i/N$, where N is the total number of samples per rotation. Figure 6.3.a shows the polar 2D representation of the scan signal. The sample is a 3-line Si grating. Polar to Cartesian coordinate transformations follow the simple relation:

$$x_i = r_i \cos\theta_i, \tag{6.1}$$

$$y_i = r_i \sin\theta_i, \tag{6.2}$$

where, r_i and θ_i refer to the radial and azimuthal coordinates of the i^{th} data sample and x_i and y_i refer to the corresponding Cartesian coordinates. Figure 6.3.b shows the 2D reconstruction in Cartesian coordinates.

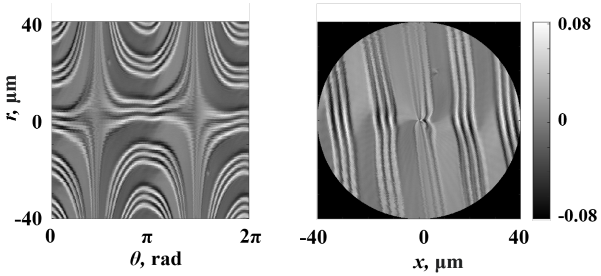

(a) (b)

Figure 6.3: 2D reconstruction of the scan sample surface, a) polar representation and b) Cartesian representation. The probe is a 0.65 NA focused spot with 635 nm wavelength. The sample consists of a 3-line Si grating scanned with $f_{\text{rotation}} = 1.64$ Hz and radial step size, $dr = 0.1\,\mu$m.

We now consider some nuances involved in the 2D reconstruction process. The first is the variation in rotation speed. In an ideal system, the rotational speed remains constant over time. However, in practice, the speed tends to drift due to mechanical properties of the rotation stage. As a result, the number of data points per rotation, N, is not uniform across different rotations. To ensure accurate 2D reconstruction, the acquired data points must first be resampled so that each rotation contains the same number of data points. For the data shown in Figure 6.3, the data points are first resampled using linear interpolation before the 2D reconstruction.

The second issue is that of the probe centering deviation. During the scan, the CFS scan head which is mounted on the piezo stage, steps along the radial direction while the sample mounted on the rotation stage is rotated continuously. The intention is of course that the piezo movement starts from the centre of rotation or the rotation axis and then steps outward. However, the piezo and the rotation stages are independent systems and their movements are not coupled. It is therefore hard to determine the position of the rotation axis with the accuracy required for nanostructure measurements. The result is that the beginning of the piezo movement may not coincide with the rotation axis. The influence of the piezo offset on the 2D reconstruction as well as the proposed solution to minimise this offset is detailed in the following subsections.

6.3. PROBE-CENTERING DEVIATION

For accurate 2D reconstruction, it is assumed that the centre of rotation coincides with the starting point of the piezo scan range. However, if there is an unknown offset between these two, the reconstructed data may exhibit distortions that vary based on both the magnitude and direction of the offset. Figure 6.4 shows a schematic of the spot offset with respect to the rotation axis. The figure shows a general case with non-zero offsets along both the x and y-directions.

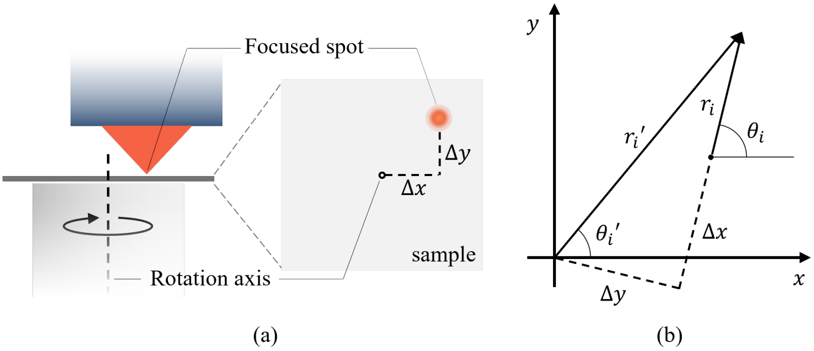

Figure 6.4: a) Schematic of the probe centering offset with respect to the rotation axis and b) polar coordinate of the i^{th} data point in the polar coordinate system with and without offset correction.

To correct the influence of the offset on the reconstruction, the corrected position coordinates need to be derived. Let the true offset of the probe relative to the rotation axis be $(\Delta x, \Delta y)$ (see Figure 6.4). The uncorrected polar coordinates of a data point are (r_i, θ_i), while the corrected coordinates are (r_i', θ_i'). The polar coordinates after correcting for the offset are [5],

$$\begin{aligned} r_i' &= \sqrt{(r_i + \Delta x)^2 + (\Delta y)^2}, \\ \theta_i' &= \theta_i - \arctan \frac{\Delta y}{r_i + \Delta x} \end{aligned} \tag{6.3}$$

The offset causes non-linear distortions in the reconstructed data. These distortions are most pronounced at small values of r_i (near the centre of the scan) and gradually diminish as r_i becomes significantly larger than the offset ($r_i \gg \Delta x, \Delta y$). As a result, the central region of the scan area is the most affected. This is evident in the scan example shown in Figure 6.3. The grating lines are no longer straight but are distorted, especially in the centre. The centering deviation introduces two major issues. First, the system fails to capture any information within a circular region of radius $\sqrt{\Delta x^2 + \Delta y^2}$ around the true rotation centre, leading to a missing data region in the reconstruction. Second, the reconstructed data no longer accurately represent the sample surface topography. The impact of these distortions depends on the specific application. For example, in contamination detection, ensuring that all particles are detected is more critical than achieving a perfectly accurate sample topography. In contrast, applications requiring precise surface profiling, such as semiconductor metrology, demand minimal distortions.

6.3.1. MINIMISING PROBE-CENTERING DEVIATION

The process of minimising the probe offset begins with the determination of the position of the rotation axis with respect to the piezo stage. A frequency spread minimisation method is used to achieve this accurately. As detailed in section 3.2, the temporal frequency of the scan signal scales with the scanning speed. For a rotating stage moving at a constant angular velocity ω, the speed, v, with which the focused spot scans the sample is a function of the distance r between the focused spot and the rotation axis: $v = \omega \cdot r$. The frequency spread of the scan signal is thus a linear function of r. We use this frequency spread variation to determine the exact position of the rotation axis in piezo coordinates.

To quantify the variation in frequency spread with the piezo position, we define the following metric:

$$S(x) = \sum_{f_i > n f_{\text{rotation}}} |D(f_i)|^2, \quad \text{with } D(f) = \mathscr{F}\{d(x)\}, \tag{6.4}$$

where, x is the piezo position, $d(x)$ is the difference signal recorded during one full rotation of the sample, $\mathscr{F}$ is the Fourier transform operator, and $f_{\text{rotation}} = \omega/2\pi$ is the fundamental rotation frequency. The parameter n is an integer greater than 1 that helps to filter out low-frequency components. The piezo position where $S(x)$ reaches its minimum corresponds to the point closest to the rotation axis:

$$x_{\text{rotation axis}} = \underset{x}{\operatorname{argmin}}\, S(x). \tag{6.5}$$

Figure 6.5 shows the variation of $S(x)$ as a function of the piezo position along the x and y-directions. A value of $n = 5$ is used for the calculation of $S(x)$ (see Appendix E). The minima, marked by dotted lines, indicate the coordinates of the rotation axis. For this scan, we determine an offset of 23.0 µm along the x-direction and 17.9 µm along the y-direction. The sample consists of a three-line Si grating fabricated on a Si wafer.

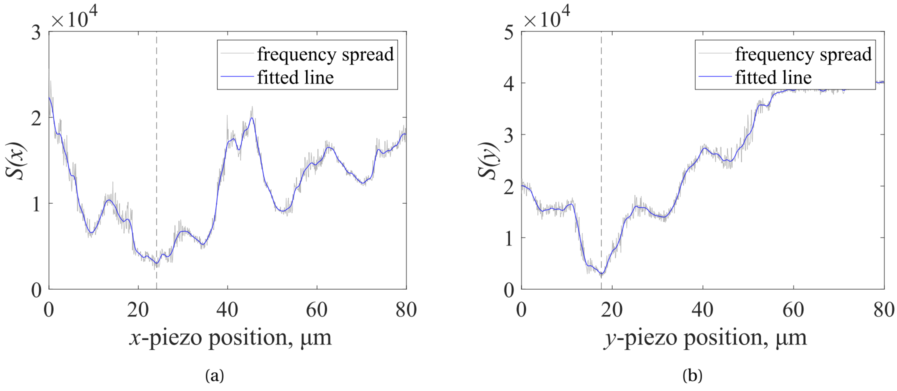

Figure 6.5: Frequency spread as a function of the piezo position along a) x-direction and b) y-direction. The dotted lines correspond to the coordinates of the rotation axis. A Savitzky-Golay filter is used to obtain the fitted line (shown in solid blue).

After the offset is calculated, the coordinates assigned to the data points can be corrected using Equation 6.3. Figure 6.6 shows the 2D reconstruction of the scan signal before and after correcting for the probe offset. The figure shows a clear reduction in the distortion near the centre of the scan. The remaining distortion could possibly be due to the radial wobble intrinsic to the rotation stage.

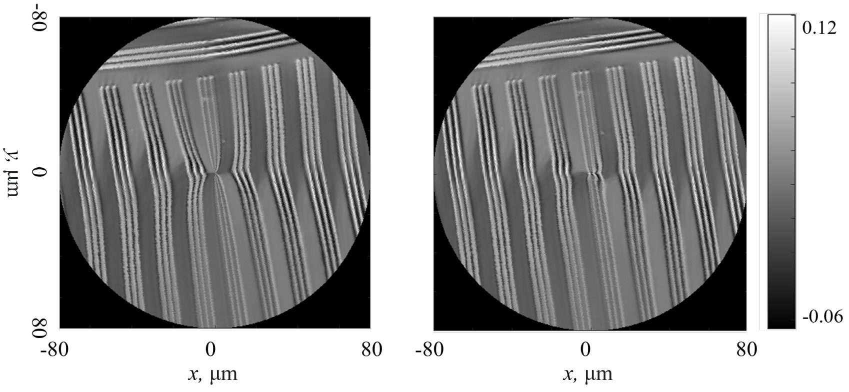

(a)

(b)

Figure 6.6: Scan surface reconstruction a) before and b) after offset correction. The offset correction is 23.0 µm along the x-direction and 17.9 µm along the y-direction. The sample consists of a 3-line grating scanned with $f_{\mathrm{rotation}} = 1.1$ Hz and $dr = 0.1$ µm.

The advantage of using the frequency-spread minimisation method to minimise the probe offset is that it does not require any prior knowledge about the geometric dimensions of the sample features or any special components such as wedges [5], [9]. However, it does require a sample with structures in the scan area and a detector with sufficient bandwidth to capture all the high frequency signal generated during the scanning process.

A rotation stage exhibits both axial and radial runout errors during its motion. Radial runout refers to deviations perpendicular to the axis of rotation, while axial runout involves tilting of the rotation axis relative to its ideal alignment. The influence of radial error is evident in the residual distortion observed near the scan centre after offset correction. Although the exact magnitude of the radial error is not quantified here, the frequency spread minimisation method could be adapted to enable more precise calculations.

So far, the focus has been on minimising probe offset by analysing the frequency spectrum of the scan signal. However, axial wobble, defined as displacement along the height direction during rotation, remains another critical source of error. In the next section, the axial wobble of the rotation stage is addressed by examining amplitude variations of the scan signal in the time domain, thereby offering a complementary strategy to improve rotational accuracy.

6.4. AXIAL WOBBLE MEASUREMENT

In this section, the depth response of the CFS scan signal is used to measure the axial wobble of the rotation stage. The difference signal in a CFS scan varies depending on the measurement plane relative to the focused spot. Since the spot has an intensity distribution that changes along the axial direction, its interaction with the sample at different depths alters the scan signal. By analysing these variations, we can generate a depth response curve that maps the signal changes to axial positions. Using the depth response curve, a signal measured at an unknown axial distance can be used to estimate the axial position of the sample. When measuring the sample position mounted on a rotation stage, the scan signal can serve as a proxy for the axial movements of the stage. Two kinds of axial wobble measurements can be made using CFS signals:

1. Height variations along one rotation - The axial position of the stage changes as it rotates. This variation depends on the mechanical properties of the rotation stage.
2. Height variations at a single point across multiple rotations - The axial position is measured at a fixed point during multiple rotations. This can give a measure of repeatability.

Both types of axial wobble can be measured using the CFS scan signal. Since the measurement is based on the variation in scan signal as a function of axial position, it is important to have multiple identical structures along one rotation to measure the axial wobble along one rotation. No such requirement is necessary to measure wobble at a specific position. For simplicity, we measure only the axial movement of the stage at a single position across multiple rotations in this study. For both, it is recommended to use a sample with extended structures, such as lines or gratings, to eliminate the influence of radial wobble, as radial wobble can shift the position of the spot relative to the scanning structure. If the structure is smaller than the combined size of the spot and wobble, it can also cause variations in the amplitude of the scan signal.

6.4.1. CREATING A DEPTH-RESPONSE CURVE

The first step in measuring axial wobble is to create a depth response curve using a sample with extended structures. Since the goal is to measure the axial wobble of the rotation stage, the same stage cannot be used to create the curve. Instead, the piezo stages along the x, y, and z axes are used to create a 3D stack of CFS scan signals. Piezo stages allow the sample to be scanned independently with sub-nanometer accuracy. Once the scan signal is obtained, the signal can be quantified by calculating the peak-to-peak value of the difference signal. The variation of this peak-to-peak value is then plotted as a function of the z-axis (axial position).

Figure 6.7a presents the normalised peak-to-peak signal as a function of the axial position. The sample consisted of a Si wafer with 10 µm-wide grating lines. The curve is asymmetric about the peak possibly due to asymmetric optical aberrations. The left and right slopes of the curve are linear and can be used as calibration curves. The right slope is chosen as it provides a steeper, more sensitive calibration curve. The slope is calculated to be $-0.149 \pm 0.010\,\mathrm{V/\mu m}$ with a confidence interval (CI) of 95%. This relation is further used to measure the axial wobble of the stage. The slope is independent of the sample properties and depends only on the optical characteristics of the focused spot.

6.4.2. MEASUREMENT USING DEPTH-RESPONSE CURVE

To measure the axial wobble at a specific position, the CFS scan head mounted on the piezo stage, was first positioned at a z-position in the linear range. The sample with the

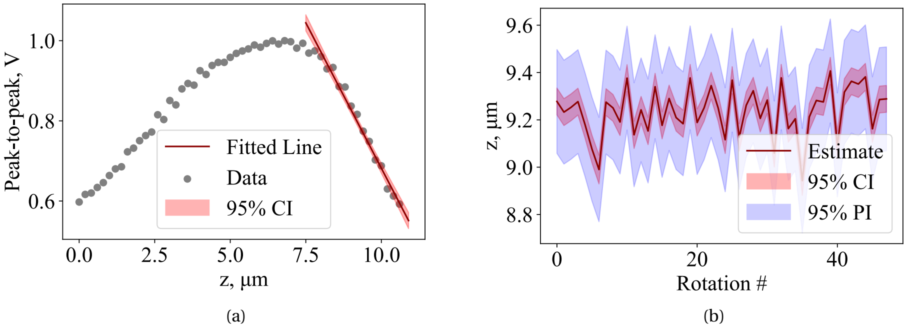

Figure 6.7: a) Depth response curve of the CFS signal. A line is fitted through the linear region of the curve (shown in red) to be used as a calibration curve to measure the axial wobble of the rotation stage. b) Axial wobble of the rotation stage measured at 80 µm from the centre of rotation. CI - confidence interval, PI - prediction interval. The sample used for measurement consists of a Si wafer with grating lines of 10 µm width fabricated on it.

line structure is then scanned at a constant radius through a number of rotations. The signal peak-to-peak is retrieved and the corresponding z-position is calculated.

Figure 6.7b shows the calculated z-values for 50 rotations. During the measurements, the CFS scan head traces a circle with a constant 80 µm radius on the sample. The sample mounted on the rotation stage was rotated at a frequency of 3.16 Hz. The measured axial wobble at a point is less than 0.9 µm with a prediction interval (PI) of 95%. The prediction interval accounts for both measurement uncertainty and inherent variations in the wobble, making it more comprehensive than the confidence interval. A similar process using a sample with repeating structures can be used to measure the axial wobble during one rotation.

The axial wobble can impact the repeatability of the CFS measurements as the signal amplitude varies with the axial position. The influence is minimal when the sample is placed in the plane with the largest signal amplitude. This is evident from Figure 6.7a where the slope is the least at the maximum. Depending on the applications, a feedback system can be employed to ensure that the scan head is in focus throughout the scan. Another solution would be to use a lens with a longer depth of focus such that the signal peak-to-peak remains the same for a longer range of motion along the z-direction but comes at the cost of the system resolution.

6.5. APPLICATIONS

In this section, two possible applications of the rotation-based CFS system are discussed: particle detection on a Si wafer and calibration of etched pits with different diameters.

6.5.1. PARTICLE DETECTION ON SI WAFER

The effectiveness of the system was demonstrated by measuring PSL particles that are randomly deposited on a Si wafer. PSL particles are widely used as metrology standards to test the sensitivity of contamination detection systems. Their scattering properties also mimic those of insulating contaminants (e.g., silicon dioxide, organic residues), commonly found on wafers. Two examples are presented: Si wafers with 1 µm and 0.4 µm PSL particles. Figure 6.8a and Figure 6.8b show the 2D differential scan map of the sample surface with 1 µm and 0.4 µm PSL particles respectively. The scan parameters were as follows: f_{rotation} - 1.1 Hz, dr - 100 nm, sampling rate - 10 kS/s. The peak-to-peak of the difference signal generated from the 1 µm and 0.4 µm PSL particles are 0.731 ± 0.167 V and 0.256 ± 0.058 V respectively. The values are presented with a confidence interval of 95%.

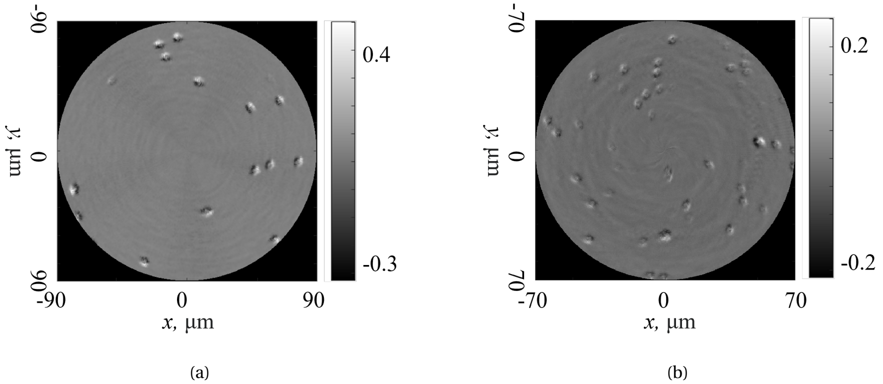

(a) (b)

Figure 6.8: 2D difference map of PSL particles on Si wafer with a) 1 µm and b) 0.4 µm diameters. The samples are scanned with $f_{\text{rotation}} = 1.1$ Hz, and minimum radial step size, $dr = 0.1$ µm.

6.5.2. CALIBRATION OF ETCHED PITS WITH DIFFERENT DIAMETERS

Another application of the setup is to measure the geometrical parameters of different nanostructures. In this example, we use the CFS setup to measure and calibrate the diameters of pits etched into a Silicon wafer. Etched structures are interesting targets due to their lower scattering signal compared to raised structures of similar dimensions, making precise measurement more challenging. The calibration sample consisted of an array of circular pits etched into a Si substrate, with diameters ranging uniformly from 225 nm to 1125 nm in 100 nm increments, spaced 10 µm apart and having constant depth of 150 nm. The samples were fabricated using e-beam lithography followed by reactive-ion etching.

Figure 6.9 shows the plot with the variation in the peak-to-peak of the difference signal from the detector as a function of the pit diameter. Each data point is an average of 8 separate measurements with an error bar of one standard deviation. The scan parameters were as follows: f_{rotation} - 1 Hz, dr - 100 nm, sampling rate - 10 kS/s. The plot demonstrates a monotonic increase in the peak-to-peak of the difference signal with the pit diameter. Furthermore, it can be used as a calibration curve to estimate an unknown pit diameter. In terms of signal-to-noise ratio (SNR), the etched pit with the smallest diameter of 225 nm (much smaller than the wavelength of 633 nm) exhibits an SNR of 17.94 dB, calculated using $\text{SNR} = 20\log_{10}\left(\frac{V_{\text{signal}}}{V_{\text{noise}}}\right)$.

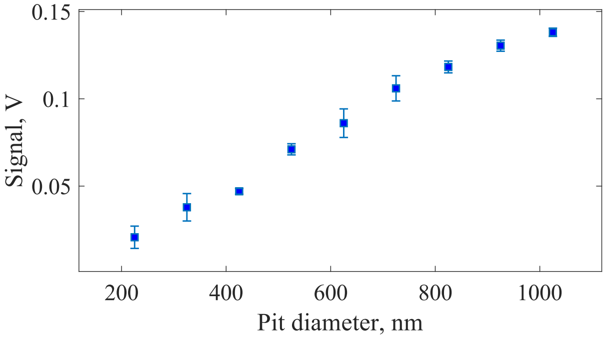

Figure 6.9: Peak-to-peak of the differential signal from the split-detector plotted as a function of the etched pit diameter. The pits are etched into a Si wafer with diameters varying from 225 nm to 1125 nm with a constant etch depth of 150 nm. Each data point is an average of 8 independent measurements.

6.6. UNCERTAINTY ASSESSMENT

In this section, we detail the contributions to the measurement uncertainty from different components of the system. The maximum input voltage range of the ADC is ±10 V.

- Detector: The dark noise of the detector is measured with the detector switched on but no light incident on the bi-cell. The measured value is 0.97 mV. This includes the noise from the ADC (analog-to-digital converter) as well.
- Laser: The laser used in the scan head is not intensity stabilised and may have fluctuations in the output power. The mean laser power was measured to be 1.019 W with a root mean square error of 0.006 W. The value was calculated from a five minute measurement using a power meter, two hours after the laser is switched on. The duration of the measurement corresponds to the duration of a typical scan. The signal varies linearly as a function of laser intensity and can differ by 0.6% from the mean value.
- Piezo: The piezo is used to step between concentric circles during the scanning. The rotational cross-talk during travel along the x-axis for a maximum radius of 80 µm is 0.8 nm in the z-direction. The influence of the motion error on the peak-to-peak of the signal depends on the position of the sample. Assuming the sample to be in the linear region of the calibration curve shown in Figure 6.7a, the signal can change by 0.01% of the original value.
- Rotation stage: The axial and radial wobble from the rotation stage contribute significantly to the measurement uncertainty. The amount of radial wobble present in the system was not quantified but its influence was evident from the remaining distortions in the reconstructions. The axial wobble was quantified to be less than 0.9 µm. The influence on the signal peak-to-peak again depends on the axial position of the sample following the curve shown in Figure 6.7a, with the signal varying between 0.31% and 11.25%.

6.7. DISCUSSION

In this study, a rotation-based coherent Fourier scatterometry (CFS) system was introduced, replacing the piezo stage in the fast-axis with a rotation stage while retaining a piezo stage in the slow-axis for stepping across concentric circles on the sample. This configuration, reminiscent of optical data storage systems, eliminates the start-stop motion characteristic of raster scans, enabling faster, continuous scanning and rendering the system suitable for high-throughput metrology applications.

Key challenges associated with rotational scanning, such as probe centring offset and axial wobble, were addressed. A frequency-spread minimisation approach was implemented to correct probe alignment errors without requiring reference targets. Additionally, the axial wobble of the rotation stage was estimated to be less than 0.9 µm using the depth-dependent response of the CFS signal.

System performance was validated through the detection of low-contrast PSL particles on silicon and calibration of nanoscale etched pits with diameters ranging from 225 to 1125 nm. These results highlight the system's potential for applications in subwavelength contamination monitoring and nanostructure metrology. Although the current implementation was designed as a proof-of-principle system, it demonstrates the feasibility of using rotational scanning for CFS to achieve rapid scanning. The system is compact, low-power, and features a simple optical design that can be easily multiplexed for scanning large areas.

BIBLIOGRAPHY

[1] S. Soman, B. I. Velt, R. Horsten, and S. F. Pereira, “Coherent Fourier scatterometry using rotational scanning”, *Optical Engineering*, vol. 64, no. 7, p. 074 106, 2025. DOI: https://doi.org/10.1117/1.OE.64.7.074106.

[2] Y. R. Teo, Y. Yong, and A. J. Fleming, “A comparison of scanning methods and the vertical control implications for scanning probe microscopy”, *Asian Journal of Control*, vol. 20, no. 4, pp. 1352–1366, 2018. DOI: https://doi.org/10.1002/asjc.1422.

[3] Y. K. Yong, S. O. R. Moheimani, B. J. Kenton, and K. K. Leang, “Invited review article: High-speed flexure-guided nanopositioning: Mechanical design and control issues”, *Review of Scientific Instruments*, vol. 83, no. 12, p. 121 101, Dec. 2012. DOI: https://doi.org/10.1063/1.4765048.

[4] X. Du and B. Anthony, “Concentric circle scanning system for large-area and high-precision imaging”, *Opt. Express*, vol. 23, no. 15, pp. 20 014–20 029, Jul. 2015. DOI: https://doi.org/10.1364/OE.23.020014.

[5] R. Ying, Y. Cui, J. Huang, D. Liang, and Y. Wang, “Precise measurement of surface topography with microstructures based on differential confocal and spiral scanning”, *Measurement*, vol. 184, p. 110 004, 2021, ISSN: 0263-2241. DOI: https://doi.org/10.1016/j.measurement.2021.110004.

[6] A. Ulčinas and Š. Vaitekonis, “Rotational scanning atomic force microscopy.”, *Nanotechnology*, vol. 28, no. 10, 10LT02, 2017. DOI: https://doi.org/10.1088/1361-6528/aa5af7.

[7] J. Peek, J. Bergmans, J. Haaren, van, F. Toolenaar, and S. Stan, *Origins and successors of the compact disc : contributions of Philips to optical storage* (Philips Research book series), English. Germany: Springer, 2009, ISBN: 978-1-4020-9552-8. DOI: https://doi.org/10.1007/978-1-4020-9553-5.

[8] H.-L. Du, P.-Y. Zeng, B.-F. Ju, Z.-Z. Zhou, S. Xu, and A. Sun, “A new centering method of the measuring probe for spiral scanning-based surface profile measurement systems”, *Measurement Science and Technology*, vol. 28, p. 025 006, 2 Dec. 2016. DOI: https://doi.org/10.1088/1361-6501/aa512b.

[9] J. Huang, Y. Cui, D. Liang, J. Xiang, and R. Ying, “Differential confocal measurement of microstructure surface topography based on centering error optimization and wavelet threshold denoising”, *Optics and Laser Technology*, vol. 160, p. 109 098, 2023, ISSN: 0030-3992. DOI: https://doi.org/10.1016/j.optlastec.2022.109098.

[10] Y. Cui, G. He, Y. Arai, and W. Gao, “Effects of centering error of probe tip in spiral scanning AFM for large-area measurement on measuring results”, in *2010 International Conference on Mechanic Automation and Control Engineering*, 2010, pp. 3024–3027. DOI: `https://doi.org/10.1109/MACE.2010.5536040`.

[11] M. Buhmann, E. Carelli, C. Egger, R. Roth, and T. Liebrich, “Investigation on probe positioning errors affecting on-machine measurements on ultra-precision turning machines”, *Procedia CIRP*, vol. 101, pp. 242–245, 2021, 9th CIRP Conference on High Performance Cutting, ISSN: 2212-8271. DOI: `https://doi.org/10.1016/j.procir.2020.10.004`.

[12] Y. Geng, X. Zhao, Y. Yan, and Z. Hu, “An AFM-based methodology for measuring axial and radial error motions of spindles”, *Measurement Science and Technology*, vol. 25, no. 5, p. 055 007, Apr. 2014. DOI: `https://dx.doi.org/10.1088/0957-0233/25/5/055007`.

[13] W. Xu, K. Lauer, Y. Chu, and E. Nazaretski, “A high-precision instrument for mapping of rotational errors in rotary stages”, *Journal of Synchrotron Radiation*, vol. 21, no. 6, pp. 1367–1369, Nov. 2014. DOI: `10.1107/S160057751401618X`. [Online]. Available: `https://doi.org/10.1107/S160057751401618X`.

[14] H. Cui, D. Lei, X. Zhang, H. Lan, Z. Jiang, and L. Kong, “Measurement and analysis of the radial motion error of aerostatic ultra-precision spindle”, *Measurement*, vol. 137, pp. 624–635, 2019, ISSN: 0263-2241. DOI: `https://doi.org/10.1016/j.measurement.2019.01.089`.

[15] R. Bartolini, “Optical recording: High-density information storage and retrieval”, *Proceedings of the IEEE*, vol. 70, no. 6, pp. 589–597, 1982. DOI: `https://doi.org/10.1109/PROC.1982.12357`.

7

SCANNING USING DIGITAL MICROMIRROR DEVICE

A digital micro-mirror device (DMD)-enabled scan head for CFS that performs lateral scanning without macroscopic moving parts, while maintaining a diffraction-limited probe is presented. A binary Fresnel zone plate (FZP) is displayed and translated on the DMD to steer a single focused spot across the sample, providing an electronically programmable alternative to scanning using piezo-based translation devices. Furthermore, the DMD programmability is used to compensate for the scan-position-dependent aberrations using an iterative optimisation algorithm. Across a 400 × 200 *DMD-pixel scan area, the peak-intensity coefficient of variation improves from 39.4% (uncorrected) to 16.1% (after correction) and to 4.47% with additional power normalisation, demonstrating substantially improved probe uniformity. Finally, particle detection on a Si wafer is demonstrated using* 1 µm *PSL particles, achieving an SNR of* 16.04 ± 1.11 *dB.*

Parts of this chapter have been published in Measurement Science and Technology **37**, 155002 (2026) [1].

7.1. INTRODUCTION

In recent decades, micro-electromechanical systems (MEMS) [2] have found widespread use as dynamic scanners in different fields including optical imaging [3], [4], display technology [5], [6], fingerprint sensing [7], [8] and for automotive LiDAR, where MEMS scanners steer the beam for time-of-flight ranging and obstacle detection [9], [10]. A prominent MEMS example is the digital micro-mirror device (DMD), which contains a 2D array of individually addressable, bistable micro-mirrors that switch within microseconds and occupy only a few square centimetres [11]. Because every micro-mirror functions as a binary "pixel", a DMD can project arbitrary intensity patterns enabling optical beam steering when incorporated into an appropriate imaging relay. This programmability makes the device a compact, low-cost alternative to galvanometric mirrors or acousto-optic deflectors for high-speed ($\approx 10-20$ kHz) lateral scanning with no macroscopic moving parts. These properties have encouraged adoption of DMDs for imaging and metrology purposes across techniques such as scanning microscopy [12]–[14], structured illumination microscopy [15], [16], light detection and ranging (LiDAR) [17], [18], compressed sensing [19], [20] and ptychography [21], [22].

This chapter details the use of a DMD for lateral scanning in a coherent Fourier scatterometry (CFS) system. Its high refresh rate, proven beam-steering precision, and scalability to parallel multi-probe operation make the DMD a compelling choice for CFS.

7.2. SCANNING STRATEGIES

In general, the scanning strategies can be categorised into three groups: i) single pixel or sub-array scanning [13], [14], [23], ii) grating projection [24], and iii) Fresnel zone plate (FZP) projection [25]–[27]. A schematic illustrating the three approaches is shown in Figure 7.1. Each approach has significant advantages and disadvantages.

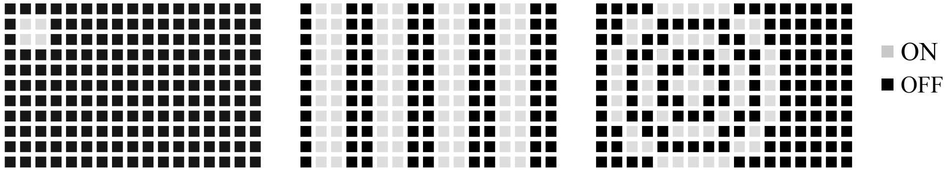

(a) (b) (c)

Figure 7.1: Schematic of different beam steering strategies: a) single-pixel/sub-array scanning, b) beam steering with different grating periods, c) translating FZP.

7.2.1. SUB-ARRAY SCANNING

In the first approach, a single micro-mirror or a small cluster of micro-mirrors on the DMD is sequentially switched on. The cluster is then re-imaged onto the sample to achieve diffraction-limited spots. The approach is easy to implement and can be multiplexed to generate multiple parallel beams but suffers from considerable power loss. Disregarding the loss of light due to the blazed grating nature of the DMD surface or fill factor, the light used per sub-array is N/N_{total}, where N is the number of pixels in the sub-array and N_{total} is the total number of illuminated pixels in the DMD. This corresponds to an efficiency of just 0.0002% for $N = 4$ using a DMD having 1920 × 1080 pixels (assuming the entire DMD is illuminated). A CFS implementation using sub-array scanning was realised by Özdemir (2025).

7.2.2. GRATING PROJECTION

The second approach involves displaying a series of binary gratings with varying spatial periods. The advantage is that a larger fraction of the beam power is used reaching up to 7% of the incident power [24]. However, it provides only coarse angular sampling and the intensity at the scan spot is not constant with steering angle: as the grating period changes, the first-order power varies because the DMD window transmission and the first-order efficiency of the grating depend on angle and polarization (Fresnel reflections and fill-factor effects) [24].

7.2.3. FZP PROJECTION SCANNING

In the third approach, an FZP translated on the DMD converts a collimated input beam into a movable focal spot, retaining a higher percentage of the input power compared to the first approach with the efficiency reaching 3.8% [25] while having angle-independent intensity. For the CFS system, the FZP scanning approach was chosen as it balances the power utilisation with better scan parameter control.

Some residual intensity variation due to the input beam profile and optical vignetting is expected and is quantified later. The minimum lateral step size during scanning is determined by the effective magnification between the DMD plane (where the FZP is displayed) and the sample/image plane. The exact value is determined experimentally using a pre-calibrated measurement target.

As we have seen in chapter 5, steering the focus off-axis inevitably introduces field-dependent aberrations that degrade focus spot quality and introduce position-dependent signal for identical samples in different parts of the field of view. Sensor-less adaptive-optics wavefront correction using DMD has been successfully implemented for imaging [28]–[36]. The same DMD that generates the FZP can thus simultaneously correct position-dependent aberrations.

The rest of this chapter is organised as follows: section 7.3 describes the experimental setup and scanning parameters, section 7.4 quantifies the system performance, including minimum step size, intensity uniformity and aberrations, section 7.5 presents scan examples of contamination detection and calibration of nanopillar diameters obtained with the setup, section 7.6 analyses the uncertainty contributions from the main system components, and section 7.7 concludes with a general discussion of the results.

7.3. EXPERIMENTAL SETUP

The schematic of the experimental setup is shown in Figure 7.2. A 632.8 nm HeNe laser (nominal output power 30 mW) is expanded using lenses L1 (f = 10 mm) and L2 (f = 250 mm) in a telescopic arrangement, providing a magnification of 25×. The expanded beam is incident on the DMD (DLP9500, Texas Instruments). Light reflected from the DMD is collimated by L3 (f = 300 mm) and then focused onto the sample by the microscope objective (N PLAN L 20×/0.40 NA, Leica). The reflected light from the sample is collected by the same objective. The back focal plane (BFP) of the objective is relayed to a differential detector (SD 085-23-21-021, Advanced Photonix) using lenses L4 ($f = 250\,\mathrm{mm}$) and L5 ($f = 50\,\mathrm{mm}$) forming a 0.2× telescope. An additional CCD camera (MER2-160-227U3M, Daheng Imaging) is used to locate areas of interest on the sample. Lenses L4 and L6 ($f = 100\,\mathrm{mm}$) demagnify the BFP by 0.4× before relaying it to the camera. A flip mirror is used to switch between the detector and camera paths. Fine focus along the z-axis is controlled using a piezo stage (M-110.12S, Physik Instrumente). Coarse alignment is provided by manual translation stages along the $x-$, $y-$, and $z-$axes.

7.3.1. DMD

The DMD chip (DLP9500, Texas Instruments, USA) has a diagonal of 0.95 inch and contains a rectangular array of 1920 × 1080 micro-mirrors with a pitch of 10.8 µm, resulting in an active area of 20.7 mm × 11.7 mm. The chip is driven by a controller board (V-9501, Vialux GmbH, Germany) capable of frame rates up to 17 857 Hz for 1-bit images. Each mirror consists of a highly reflective aluminium surface attached via a post to compliant torsion hinges that define the rotation axis. With an applied voltage, the mirror rotates and latches electrostatically into one of two stable tilt states. In the ON state the mirror tilts by $+12°$ with respect to the substrate normal, in the OFF state it tilts by $-12°$. With no voltage, the mirror remains parallel to the substrate (“PARKED”). Figure 7.2a schematically illustrates the mirror states.

In the configuration of Figure 7.2a, the input beam is incident on the DMD at 24° relative to the substrate normal so that light from ON pixels is directed along the optical axis of the system. The DMD package is mounted with its substrate normal parallel to the optical axis. Because the torsion hinge lies along the mirror diagonal, the ON/OFF deflections occur in a plane rotated by 45° about the optical axis. Accordingly, the entire DMD is rotated by 45° during mounting so that the reflected beams lie in the horizontal plane of the optical table.

7.3.2. SCANNING

Following the discussion in section 7.2, scanning is performed by sequentially projecting binary FZP patterns on the DMD. An FZP consists of a series of concentric circular rings with increasing radius, designed to focus an incident plane wave to focal length f at wavelength λ. The radius of the n^{th} zone boundary is given by [37],

$$r_n = \sqrt{n\lambda f + \frac{n^2\lambda^2}{4}}, \tag{7.1}$$

which reduces to

$$r_n \approx \sqrt{n\lambda f}, \qquad \text{when } f \gg n\lambda/4. \tag{7.2}$$

Let p denote the DMD micromirror pitch. The outermost zone index n is chosen such that the width of the outermost ring equals one micromirror pitch, i.e. $r_n - r_{n-1} = p$.

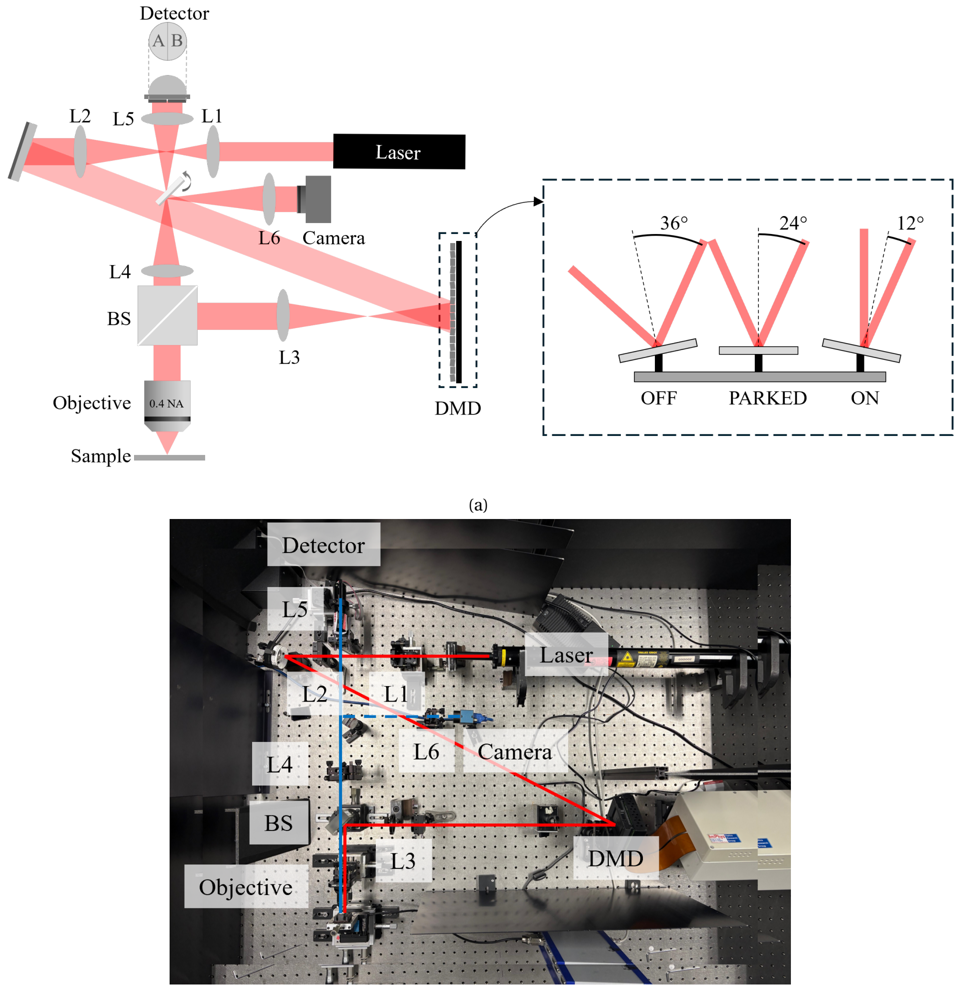

(a)

(b)

Figure 7.2: a) Schematic of the optical setup, b) photo of the setup on the optical table: Red lines indicate the light path to the sample and blue the path of the light after reflection from the sample to the detector. Dotted blue line indicates the reflected path to the camera. Lenses L1 - 10 mm, L2 - 250 mm, L3 - 300 mm, L4 - 250 mm, L5 - 50 mm, L6 - 100 mm, Objective - 0.4 NA (N PLAN L 20x/0.40, Leica) objective lens, BS - beam splitter, DMD - digital micro-mirror device (DLP9500, Texas Instruments), laser - 632.8 nm HeNe.

Using $r_n^2 - r_{n-1}^2 = \lambda f$ and $r_n + r_{n-1} \approx 2r_n$ gives

$$r_n = \frac{\lambda f}{2p}, \qquad n = \frac{\lambda f}{(2p)^2}. \tag{7.3}$$

For $f = 150\,\mathrm{mm}$, $\lambda = 632.8\,\mathrm{nm}$, and $p = 10.8\,\mu\mathrm{m}$, $r_n = 4.39\,\mathrm{mm}$, corresponding to the last zone diameter of 813 micromirrors at $n = 203$.

Figure 7.3 shows the schematic of the FZP scanning on the DMD. The scanning consists of displaying FZP patterns centred at different (x_c, y_c) positions on the DMD. The amount of lateral shift along x and y-directions are programmed by Δx and Δy, with a minimum DMD-plane step equal to one micromirror, $\Delta x_{\mathrm{min}} = \Delta y_{\mathrm{min}} = p$. If M is the magnification of the relay between the FZP focal plane and the sample plane, the minimum step-size in the sample plane, $\Delta x_{\mathrm{s,min}}$, is Mp. To avoid cropping the FZP at the device edges, the admissible FZP-centre window is reduced to $(1920-813) \times (1080-813) = 1107 \times 267$ micromirrors on a 1920×1080 DMD. While scanning, each FZP pattern is projected on the DMD for a duration of $1/f_{\mathrm{DMD}}$, where f_{DMD} corresponds to the refresh rate of the DMD. The unwanted higher diffraction orders are blocked using an aperture placed in the focal plane of the FZP.

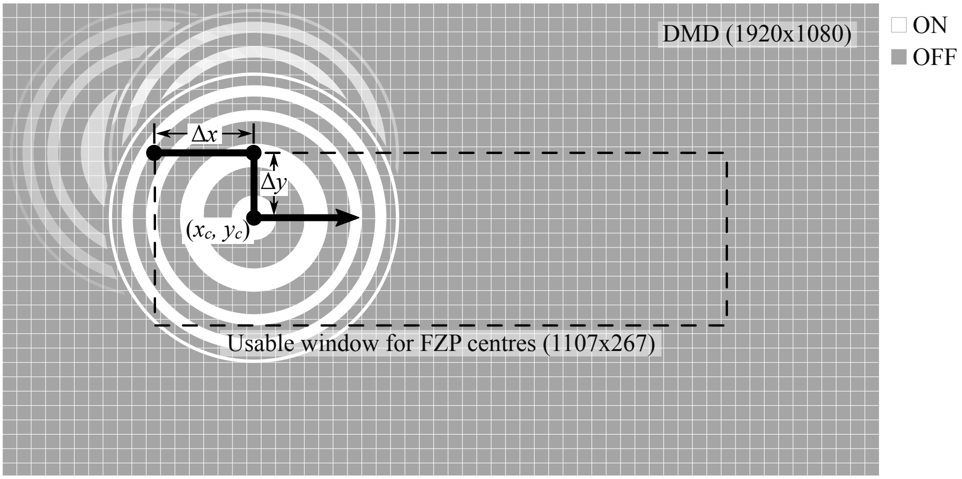

Figure 7.3: Schematic of the FZP pattern scanning on the DMD. The pattern is centred at (x_c, y_c) and the offset steps along the x and y-directions are denoted by Δx and Δy respectively.

Differential signals are recorded continuously with the quadrant detector. The four photodiode outputs (A, B, C, D) are digitised simultaneously (NI 9215, ±10V). Two differential detector signals along two orthogonal directions can be calculated as,

$$D_1 = (A + B) - (C + D) \tag{7.4}$$

$$D_2 = (A + D) - (B + C). \tag{7.5}$$

The detector is aligned such that the beam is centred uniformly between the four quadrants.

7.3.3. FOCUSING EFFICIENCY

The amount of power concentrated in the focus spot can be calculated as [25],

$$\begin{aligned}\eta_{\text{focus}} &= \eta_{\text{FZP}}\,\eta_{\text{circ}}\,\eta_{\text{DMD}} && (7.6)\\ &= 0.016 \quad \text{(experimentally measured)}, && (7.7)\end{aligned}$$

where,

- η_{focus} is the fraction of total power incident on the DMD that is concentrated in the focus spot of the FZP
- $\eta_{\text{FZP}} = 1/\pi^2$ is the focusing efficiency of a binary FZP into the first-order focus,
- $\eta_{\text{circ}} = 0.250$ is the fraction of the area covered by the FZP on the DMD,
- $\eta_{\text{DMD}} = 0.633$ (experimentally measured) is the overall optical efficiency due to the DMD [38].

$$\eta_{\text{DMD}} = \eta^2_{\text{transmission window}}\,\eta_{\text{fillfactor}}\,\eta_{\text{diffraction}}\,\eta_{\text{reflectivity}} \tag{7.8}$$

- $\eta_{\text{transmission window}}$ is the single-pass window transmission including anti-reflection coatings,
- $\eta_{\text{fillfactor}}$ is the fractional mirror coverage,
- $\eta_{\text{diffraction}}$ is the mirror array diffraction efficiency which can include effects of non-flat mirrors,
- $\eta_{\text{reflectivity}}$ is the mirror reflectivity.

7.4. SYSTEM CHARACTERISATION

This section discusses system characteristics relevant to scanning performance: step size, intensity calibration, and position-dependent aberrations.

7.4.1. STEP SIZE MEASUREMENT

Unlike scanning stages with position sensors for feedback, the beam position during DMD scanning is not directly measured and therefore must be calibrated before use. In practice, this amounts to mapping scan parameters expressed in DMD coordinates to coordinates in the sample (image) plane. Apart from residual optical distortion, the mapping is a geometric scaling set by the effective magnification of the relay after the DMD (lens L3 and the objective).

To guarantee sufficient sampling, the Nyquist criterion is applied to the highest spatial frequency of interest. As detailed in section 3.2, for a system with NA = 0.40 and a wavelength of 632.8 nm, the largest detectable sample spatial frequency is $f_{\text{max}} = 1.264\,\mu\text{m}^{-1}$. According to the Nyquist criterion,

$$\Delta x_{\text{s,min}} \leq \frac{1}{2 f_{\text{max}}} = 0.396\,\mu\text{m},$$

where $\Delta x_{\mathrm{s,min}}$ denotes the sample-plane step corresponding to a one-micro-mirror shift on the DMD.

The actual step size $\Delta x_{\mathrm{s,min}}$ is unknown a priori and is therefore determined experimentally. For this purpose, a diffraction grating with a period of 1658 nm and a 50% duty cycle was used. The sample was fabricated and pre-calibrated by partners of the 17FUN01 BeCOMe project. Their periods have been independently measured using a SEM. The differential signal obtained while scanning perpendicular to the grating lines is periodic with the same spatial period as the grating. The step size corresponding to one micro-mirror shift is computed directly from the scan data. Figure 7.4 shows the step-size calculation from the 2D differential data of a grating sample. Figure 7.4b shows a profile perpendicular to the grating lines (blue circles) extracted from the 2D data, interpolated profile (black dashed line), and the minima (red triangles). The separation distance between two consecutive minima corresponds to one grating period. From the data, the step-size corresponding to one micro-mirror shift is measured to be (0.363 ± 0.008) μm, which satisfies the Nyquist condition.

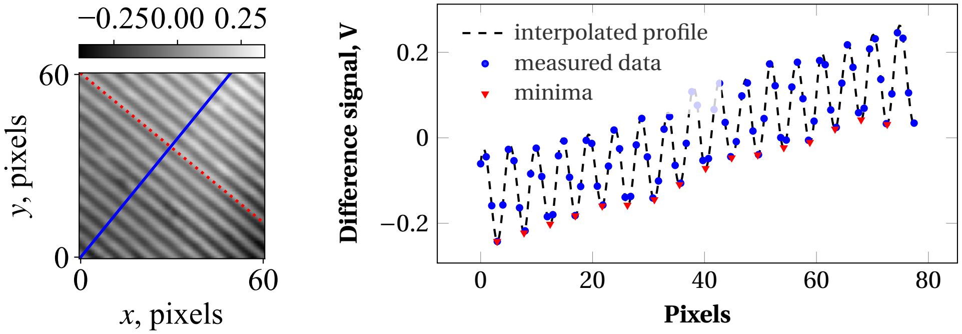

(a)

(b)

Figure 7.4: Step-size calculation. (a) 2D differential CFS signal from a grating with a period of 1658 nm. The red dotted line is parallel to the grating (detected via a Hough transform), the blue solid line is the profile drawn perpendicular to the grating lines. The $x-y$ axes correspond to the center pixel of the FZP projection on the DMD. (b) Measured data along the perpendicular profile (blue circles), interpolated profile (black dashed), and detected minima (red triangles). The distance between two consecutive minima equals one grating period.

The same method was also used to measure the optical distortion in the system. Ideally, the scan grid in the sample plane is a rectilinear mapping of the DMD micro-mirror array. Optical distortion would appear as location-dependent changes in the measured step size. Scans shifted by ±250 micro-mirrors along x resulted in step-sizes of 0.364 μm and 0.366 μm, respectively, both within the ±0.008 μm measurement uncertainty, indicating negligible distortion over the tested field of view.

7.4.2. INTENSITY VARIATION

After expansion by lenses L1 and L2, the beam incident on the DMD exhibits a low-frequency, non-uniform intensity distribution across the DMD surface owing to the Gaussian distribution of the light emitted from the HeNe laser. During scanning, each displayed pattern samples only a local portion of this beam. Consequently, spatial variations in the input intensity produce position-dependent variations of the focal-spot intensity in the image plane, directly affecting the measurement.

To compensate, the intensity distribution is measured in advance and used for a position-dependent normalisation. Over the operating range, the differential signal varies linearly with input power, so a simple correction suffices: if $P(x_\mathrm{s}, y_\mathrm{s})$ is the measured power map in the sample plane at scan position $(x_\mathrm{s}, y_\mathrm{s})$, the corrected signals are,

$$D_1'(x_\mathrm{s}, y_\mathrm{s}) = \frac{D_1(x_\mathrm{s}, y_\mathrm{s})}{P(x_\mathrm{s}, y_\mathrm{s})}, \qquad D_2'(x_\mathrm{s}, y_\mathrm{s}) = \frac{D_2(x_\mathrm{s}, y_\mathrm{s})}{P(x_\mathrm{s}, y_\mathrm{s})}.$$

$P(x_\mathrm{s}, y_\mathrm{s})$ was measured directly using a power meter placed in the image plane without any sample. Figure 7.5 shows the variation in input power as a function of the focus spot position in the image plane. Across the measured field ($N = 64$ positions), the power ranged from 9.51 µW to 51.4 µW, with a mean of 30.58 µW and standard deviation of 11.27 µW, corresponding to a coefficient of variation of 36.84%. The peak-to-peak variation is 36.77 µW, i.e. 136.96% of the mean, indicating substantial non-uniformity.

The measured non-uniformity reflects not only the laser beam envelope but also system effects such as relay vignetting so the normalisation compensates for their combined influence. To guard against temporal drift, it is advisable to re-measure the power variation every day before actual sample measurements.

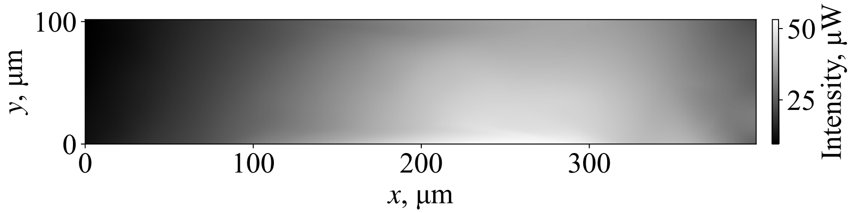

Figure 7.5: Measured intensity variation in the image plane. The power at each scan position is recorded with a power meter to generate a position-dependent normalisation map $P(x_\mathrm{s}, y_\mathrm{s})$.

7.4.3. ABERRATION CORRECTION

Building on the preceding calibration of step size and intensity uniformity, this section addresses field-dependent aberrations introduced while scanning. Each scan position experiences a slightly different optical path, as a result, the point-spread function (PSF) varies across the field of view. This variability degrades measurement quality because identical structures at different scan coordinates can yield inconsistent signals, increasing measurement uncertainty. Using the programmability of the DMD, in addition to scanning, the same device can also be used to correct aberrations. For each scan coordinate in the image plane, a suitable correction phase can be computed and displayed on the DMD, thereby improving PSF uniformity in the image plane over the entire field of view and reducing measurement uncertainty.

To determine the optimal correction, the wavefront at each position is expressed in a Zernike polynomial basis. Zernike polynomials provide a convenient, orthogonal basis for representing common aberrations such as astigmatism, coma, defocus, and spherical aberration on a circular pupil. An optimisation algorithm, shown schematically in Figure 7.6, is used to find the optimal Zernike coefficients at each scan position. Zernike modes follow the Noll indexing, and are reported in units of wavelength for the illumination wavelength λ [39]. As the DMD can project only binary amplitude modulation, the required phase corrections must first be encoded as binary amplitude patterns. The binary amplitude distribution $A(x, y)$ for each scan position is computed from the desired phase-correction map $\varphi(x, y)$ as

$$A(x, y) = \begin{cases} 1, & \cos\varphi(x, y) > 0, \\ 0, & \text{otherwise.} \end{cases} \tag{7.9}$$

During the optimisation, only the first 14 Zernike modes (excluding piston, tip and tilt) were considered as there was minimal improvement in the spot after that. In the first pass, each coefficient was varied between -2 to 2 in steps of 0.1. Successive passes reduced the range and step size by half. The optimisation was implemented as a two-loop process: the outer loop controlled the total number of passes over the selected modes, while the inner loop optimised each aberration sequentially. Once an aberration coefficient was determined, it was kept fixed while the next mode was optimised. When all selected modes were completed, the process repeated according to the number of passes specified in the outer loop, with the reduced coefficient range and step size in each iteration.

A camera conjugate to the image plane, located at the focal plane of lens L5 (see Figure 7.2a), is used to record the resulting focus spot. Spot intensity and shape are quantified by fitting a two-dimensional Gaussian distribution to each image after mean-background subtraction. The peak of the fitted Gaussian is evaluated as a function of the Zernike coefficient, and the coefficient that maximises the peak is taken as the optimal value for that mode. This procedure is repeated for each scan coordinate to determine the aberration correction at every scan position.

To evaluate the effectiveness of the method, quantitative comparisons of the focus spot characteristics before and after optimisation are conducted. A representative example at the scan position $(14.52\,\mu\text{m}, 0)$ in the image plane (pattern centred at $(40, 0)$ on the DMD) is shown in Figure 7.7. Figure 7.7a shows the optimised phase map used for correction. The corresponding intensity profiles of the focus spot along the x- and y-axes, before and after aberration correction, are shown in Figure 7.7b. Before correction, the intensity distribution exhibits noticeable asymmetry and a reduced peak due to aberration-induced wavefront distortion. After correction, the intensity profiles are more symmetric, and the peak intensity increases by 45%. Asymmetry is quantified using full width at half-maximum (FWHM) of the spot as,

$$\epsilon = \frac{|\text{FWHM}_x - \text{FWHM}_y|}{\text{FWHM}_x + \text{FWHM}_y}, \tag{7.10}$$

where FWHM_x and FWHM_y are the full widths at half maximum along the x and y axes. For the example shown, ϵ decreases from 0.053 to 0.007 after correction.

Figure 7.8 shows the spatial distributions after optimisation over a 400 × 200 DMD-pixel scan area: (a)–(c) focus-spot peak intensity (before optimisation, after optimisa-

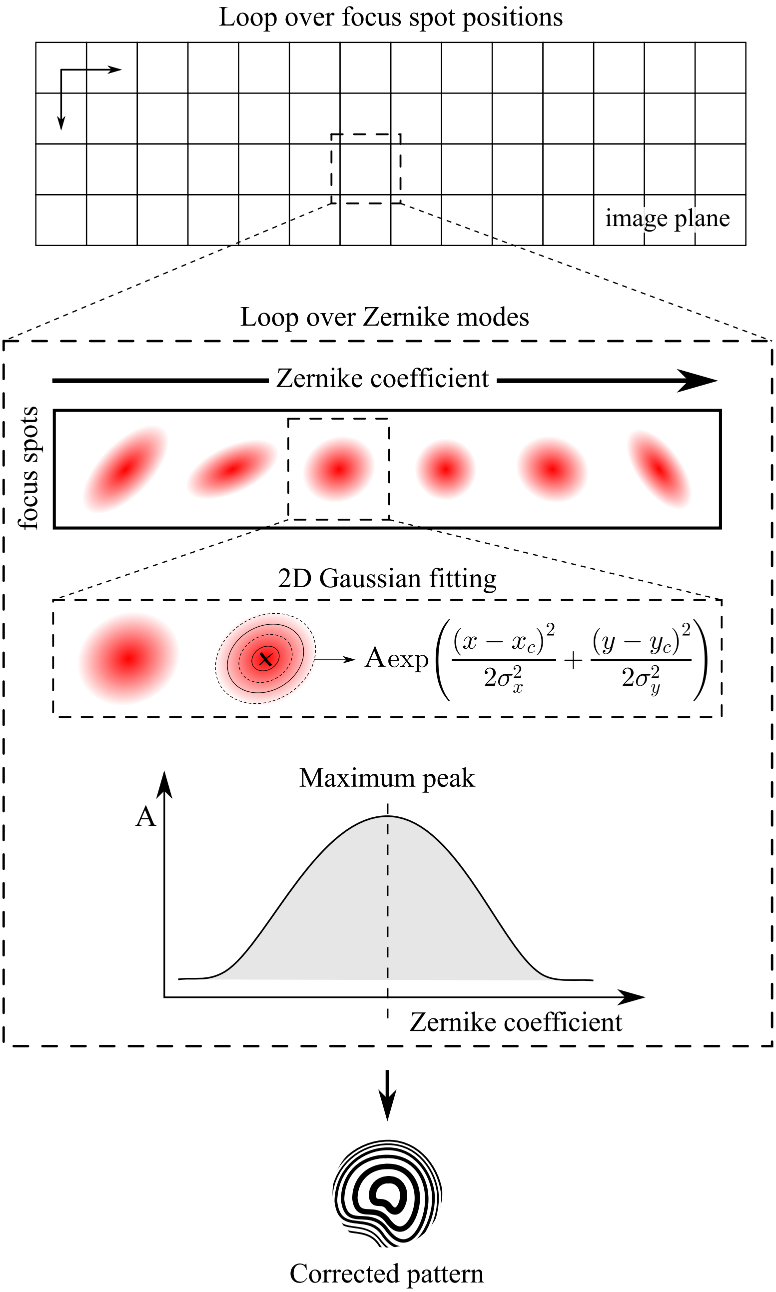

Figure 7.6: Schematic of the optimisation algorithm for aberration correction.

tion, and after normalisation with input power) and (d)–(e) ϵ (before and after optimisation). The mean improvement in the spot intensity across the area is $205 \pm 115\%$. The coefficient of variation (standard deviation/mean) in the spot intensity across the 2D array before optimisation is 39.42%. The value reduces to 16.13% after optimisation and further reduces to 4.47% after normalisation with input intensity. Similarly, the mean ϵ value reduces from 0.109 to 0.022 after optimisation. More plots about the algorithm convergence, coefficient fitting and the spatial variation of the retrieved optimum coefficients are shown in Appendix F.

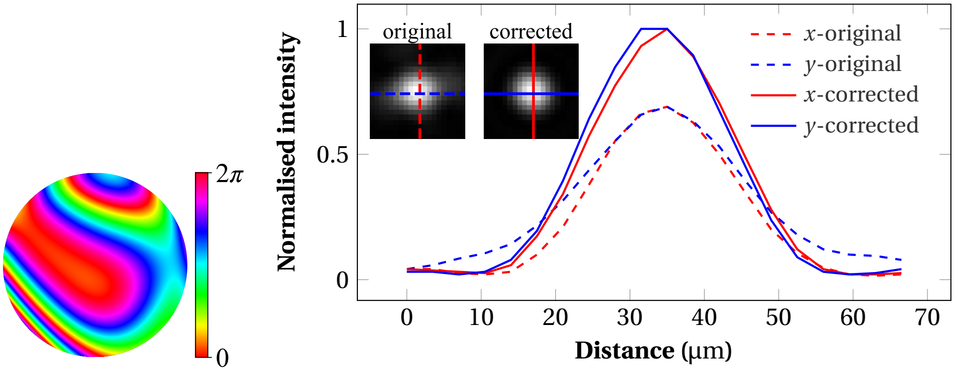

(a) (b)

Figure 7.7: (a) Phase map of the Zernike-based phase correction. (b) Magnified focus spot intensity profiles along the x- and y-axes before (dashed) and after (solid) correction.

7.5. APPLICATIONS

The performance of the DMD-based CFS system is illustrated through two different examples: particle detection on a Si wafer and calibration of nanopillars with varying diameter.

7.5.1. PARTICLE DETECTION ON SI WAFER

The scanning system was demonstrated by measuring polystyrene latex (PSL) particles that are randomly deposited on a Si wafer. PSL particles are widely used as metrology standards to test the sensitivity of contamination detection systems. Their scattering properties also mimic those of insulating contaminants, commonly found on wafers. Figure 7.9 shows the 2D differential scan map of a Si wafer with 1 µm PSL particles. The signal-to-noise ratio (SNR) of the differential signal was measured to be 16.12 dB, following the definition $\mathrm{SNR} = 20\log_{10}\left(\frac{\mathrm{V_{signal}}}{\mathrm{V_{noise}}}\right)$.

7.5.2. CALIBRATION OF NANOPILLARS WITH DIFFERENT DIAMETERS

Another application of the setup is to measure the geometrical parameters of different nanostructures. In this example the CFS setup was used to measure and calibrate the diameters of nanopillars on a Si wafer. Two kinds of structures were measured: etched

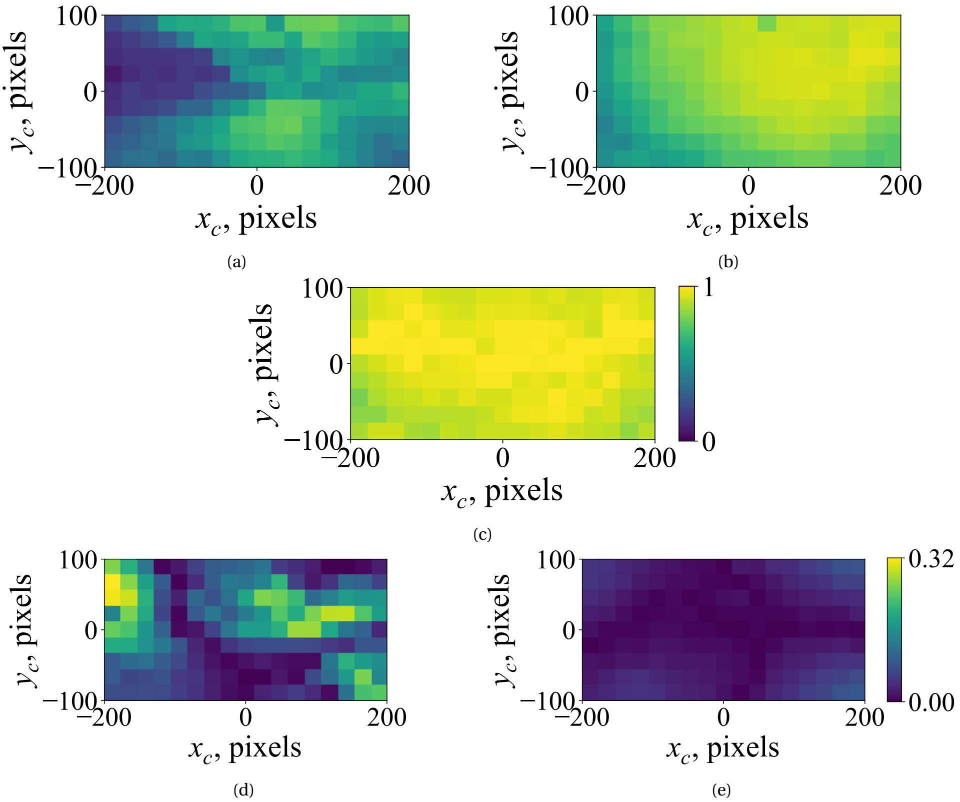

(a) (b) (c) (d) (e)

Figure 7.8: 2D distribution of focus spot metrics before and after optimisation. Focus spot peak intensity a) before optimisation, b) after optimisation and c) after optimisation and normalisation with input power. FWHM asymmetry, ϵ d) before and e) after optimisation.

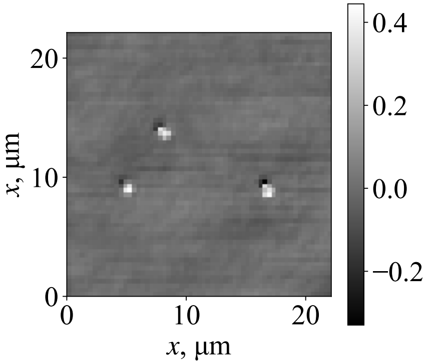

Figure 7.9: 2D differential scan of 1 µm PSL particles on a Si wafer.

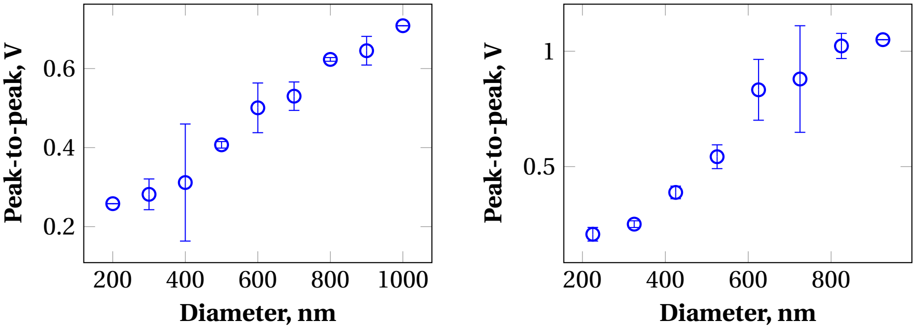

(a) (b)

Figure 7.10: Peak-to-peak of the differential signal plotted as a function of the diameter of the a) Si nanopillars and b) etched cylindrical pits on a Si wafer. The error bars correspond to one standard deviation over 4 measurements.

pits and raised pillars. The etched pit sample consisted of an array of circular pits etched into a Si substrate, with diameters ranging uniformly from 225 nm to 1125 nm in 100 nm increments, spaced 10 µm apart and having constant depth of 150 nm. The sample with the nanopillars has pillar diameters varying from 200 to 1000 nm in 100 nm increments also spaced 10 µm apart with a height of 150 nm. Both samples were fabricated using e-beam lithography followed by reactive-ion etching. Figure 7.10a plots the peak-to-peak of the difference signal as a function of the pillar diameter while Figure 7.10b plots the same for the etched pits. Each data point is an average of 4 separate measurements with the error bar corresponding to one standard deviation. The plots demonstrate a monotonic increase in the peak-to-peak of the difference signal with the diameter and can be used as calibration curves to estimate an unknown pillar diameter.

7.6. UNCERTAINTY ASSESSMENT

This section details the measurement uncertainty contributions from the different system components.

- Detector: The dark noise of the detector is measured with the detector switched on but no light incident on the bi-cell. The measured value is 9.27 mV. This includes the noise from the ADC (analog-to-digital converter) as well.
- Laser: The laser used in the scan head is not intensity stabilised and may have fluctuations in the output power. The mean laser power was measured to be 19.2 mW with a standard deviation of 65.2 µW. The value was calculated from a 1 minute measurement of the laser intensity using a power meter, two hours after the laser is switched on. The duration of the measurement corresponds to the duration of a typical scan time. The signal varies linearly as a function of laser intensity and can differ by 0.338% from the mean value.
- DMD: The pointing stability of the DMD was measured by placing the quadrant detector directly in the sample plane and recording the difference signal as a func-

tion of time. The difference signal was normalised by the total power to account for variation in input power. Ideally, the signal should remain constant with time and any deviations indicate drift or disturbances to the setup. The standard deviations of the two difference signals, D'_1 and D'_2 for a two minute measurement are 0.051 V and 0.024 V respectively.

7.7. DISCUSSION

In this chapter, a DMD-based scanning system for a CFS setup is presented. An FZP pattern is projected on the DMD and sequentially shifted to scan the focus spot in the image plane. The setup has no macroscopic moving components, reducing mechanical vibrations. The high switching rate of the DMD also enables fast scanning. The setup used a switching rate of 250 Hz as the patterns were in 8-bit format. 1-bit encoding should enable faster scans up to 17 kHz. The measurement protocol takes into account issues such as non-uniform intensity of the incident beam as well as the intrinsic problem of off-axis beam aberrations associated with beam scanning approaches. An iterative optimisation algorithm is used to project aberration corrected scan patterns on the DMD combining both scanning and aberration correction improving PSF uniformity over the scan area.

The system performance was demonstrated in two applications: the detection of particle contamination on a Si wafer and calibration of the diameter of cylindrical nanostructures. These results show the potential of the system for applications in sub-wavelength contamination detection and nanostructure metrology.

Despite the advantages, the biggest drawback of the technique is the low power efficiency. The use of an FZP pattern over single pixel scanning improves the efficiency but is still limited to 1.6%. A parallelised scanning strategy making use of the existing higher diffraction orders generated from the grating effect of the DMD can improve both the scan time and power utilisation even further.

BIBLIOGRAPHY

[1] S. Soman, E. Özdemir, and S. F. Pereira, "Scanning in coherent Fourier scatterometry using Fresnel zone plate projection on a digital micro-mirror device", *Measurement Science and Technology*, vol. 37, p. 155 002, 2026. DOI: https://doi.org/10.1088/1361-6501/ae5abc.

[2] S. T. S. Holmström, U. Baran, and H. Urey, "MEMS laser scanners: A review", *Journal of Microelectromechanical Systems*, vol. 23, no. 2, pp. 259–275, 2014. DOI: https://doi.org/10.1109/JMEMS.2013.2295470.

[3] Q. Cui and R. Liang, "Chromatic confocal microscopy using liquid crystal display panels", *Applied optics*, vol. 58, no. 8, pp. 2085–2090, 2019. DOI: https://doi.org/10.1364/AO.58.002085.

[4] Z. Qiu and W. Piyawattanamatha, "New endoscopic imaging technology based on MEMS sensors and actuators", *Micromachines*, vol. 8, no. 7, p. 210, 2017. DOI: https://doi.org/10.3390/mi8070210.

[5] P. F. Van Kessel, L. J. Hornbeck, R. E. Meier, and M. R. Douglass, "A mems-based projection display", *Proceedings of the IEEE*, vol. 86, no. 8, pp. 1687–1704, 1998. DOI: https://doi.org/10.1109/5.704274.

[6] J. Ma, "Advanced mems-based technologies and displays", *Displays*, vol. 37, pp. 2–10, 2015. DOI: https://doi.org/10.1016/j.displa.2014.10.003.

[7] G.-D. Su, S.-S. Lee, and M. C. Wu, "Optical scanners realized by surface-micromachined vertical torsion mirror", *IEEE Photonics Technology Letters*, vol. 11, no. 5, pp. 587–589, 1999. DOI: https://doi.org/10.1109/68.759407.

[8] X. Jiang, Y. Lu, H.-Y. Tang, *et al.*, "Monolithic ultrasound fingerprint sensor", *Microsystems & nanoengineering*, vol. 3, no. 1, pp. 1–8, 2017. DOI: https://doi.org/10.1038/micronano.2017.59.

[9] X. Zhang, K. Kwon, J. Henriksson, J. Luo, and M. C. Wu, "A large-scale microelectromechanical-systems-based silicon photonics LiDAR", *Nature*, vol. 603, no. 7900, pp. 253–258, 2022. DOI: https://doi.org/10.1038/s41586-022-04415-8.

[10] U. Hofmann, F. Senger, F. Soerensen, V. Stenchly, B. Jensen, and J. Janes, "Biaxial resonant 7 mm-MEMS mirror for automotive LIDAR application", in *2012 International Conference on optical MEMS and nanophotonics*, IEEE, 2012, pp. 150–151. DOI: https://doi.org/10.1109/OMEMS.2012.6318847.

[11] H. H. Refai, J. J. S. Jr., and M. P. Tull, "Digital micromirror device for optical scanning applications", *Optical Engineering*, vol. 46, no. 8, p. 085 401, 2007. DOI: https://doi.org/10.1117/1.2768978.

[12] J. Cheng, C. Gu, D. Zhang, D. Wang, and S.-C. Chen, “Ultrafast axial scanning for two-photon microscopy via a digital micromirror device and binary holography”, *Opt. Lett.*, vol. 41, no. 7, pp. 1451–1454, Apr. 2016. DOI: https://doi.org/10.1364/OL.41.001451.

[13] Q. Wang, J. Zheng, K. Wang, K. Gui, H. Guo, and S. Zhuang, “Parallel detection experiment of fluorescence confocal microscopy using DMD”, *Scanning*, vol. 38, no. 3, pp. 234–239, 2016. DOI: https://doi.org/10.1002/sca.21265.

[14] S. Li and R. Liang, “DMD-based three-dimensional chromatic confocal microscopy”, *Applied optics*, vol. 59, no. 14, pp. 4349–4356, 2020. DOI: https://doi.org/10.1364/AO.386863.

[15] D. Dan, M. Lei, B. Yao, *et al.*, “DMD-based LED-illumination super-resolution and optical sectioning microscopy”, *Scientific reports*, vol. 3, no. 1, p. 1116, 2013. DOI: https://doi.org/10.1038/srep01116.

[16] M. Li, Y. Li, W. Liu, *et al.*, “Structured illumination microscopy using digital micromirror device and coherent light source”, *Applied Physics Letters*, vol. 116, no. 23, 2020. DOI: https://doi.org/10.1063/5.0008264.

[17] B. Smith, B. Hellman, A. Gin, A. Espinoza, and Y. Takashima, “Single chip lidar with discrete beam steering by digital micromirror device”, *Opt. Express*, vol. 25, no. 13, pp. 14 732–14 745, Jun. 2017. DOI: https://doi.org/10.1364/OE.25.014732.

[18] J. Rodriguez, B. Smith, B. Hellman, and Y. Takashima, “Fast laser beam steering into multiple diffraction orders with a single digital micromirror device for time-of-flight lidar”, *Applied Optics*, vol. 59, no. 22, G239–G248, 2020. DOI: https://doi.org/10.1364/AO.393075.

[19] H. Rueda, H. Arguello, and G. R. Arce, “DMD-based implementation of patterned optical filter arrays for compressive spectral imaging”, *Journal of the Optical Society of America A*, vol. 32, no. 1, pp. 80–89, 2014. DOI: https://doi.org/10.1364/JOSAA.32.000080.

[20] A. Sun, Z. Ding-fu, Y. Sheng, H. You-jun, Z. Peng, Y. Jian-ming, *et al.*, “Optical scanning holography based on compressive sensing using a digital micro-mirror device”, *Optics Communications*, vol. 385, pp. 19–24, 2017. DOI: https://doi.org/10.1016/j.optcom.2016.10.034.

[21] C. Kuang, Y. Ma, R. Zhou, *et al.*, “Digital micromirror device-based laser-illumination Fourier ptychographic microscopy”, *Opt. Express*, vol. 23, no. 21, pp. 26 999–27 010, Oct. 2015. DOI: https://doi.org/10.1364/OE.23.026999.

[22] A. Sun, X. He, Y. Kong, *et al.*, “Ultra-high speed digital micro-mirror device based ptychographic iterative engine method”, *Biomedical Optics Express*, vol. 8, no. 7, pp. 3155–3162, 2017. DOI: https://doi.org/10.1364/BOE.8.003155.

[23] Y. Zhang, S. Strube, G. Molnar, *et al.*, “Parallel large-range scanning confocal microscope based on a digital micromirror device”, *Optik*, vol. 124, no. 13, pp. 1585–1588, 2013. DOI: https://doi.org/10.1016/j.ijleo.2012.04.028.

[24] J. Jang, W. Kim, J. S. Oh, S.-W. Kim, and Y.-J. Kim, “Fast and precise laser beam scanning by nonperiodic grating on a binary micromirror array”, *Optical Engineering*, vol. 61, no. 6, pp. 061 412–061 412, 2022. DOI: `https://doi.org/10.1117/1.OE.61.6.061412`.

[25] D. M. Benton, “Multiple beam steering using dynamic zone plates on a micromirror array”, *Optical Engineering*, vol. 57, no. 7, pp. 073 109–073 109, 2018. DOI: `https://doi.org/10.1117/1.OE.57.7.073109`.

[26] Q. Cao and J. Jahns, “Comprehensive focusing analysis of various Fresnel zone plates”, *Journal of the Optical Society of America A*, vol. 21, no. 4, pp. 561–571, 2004. DOI: `https://doi.org/10.1364/josaa.21.000561`.

[27] J. R. Lindle and A. T. Watnik, “Large angle nonmechanical laser beam steering at 4.6 um using a digital micromirror device”, *Optical Engineering*, vol. 57, no. 2, pp. 027 108–027 108, 2018. DOI: `https://doi.org/10.1117/1.OE.57.2.027108`.

[28] M. Ren, J. Chen, D. Chen, and S.-C. Chen, “Aberration-free 3D imaging via DMD-based two-photon microscopy and sensorless adaptive optics”, *Optics letters*, vol. 45, no. 9, pp. 2656–2659, 2020. DOI: `https://doi.org/10.1364/OL.392947`.

[29] Y. Wang, H. Li, Q. Hu, *et al.*, “Aberration-corrected three-dimensional non-inertial scanning for femtosecond lasers”, *Optics Express*, vol. 28, no. 20, pp. 29 904–29 917, 2020. DOI: `https://doi.org/10.1364/OE.405532`.

[30] P. Pozzi, D. Wilding, O. Soloviev, *et al.*, “High speed wavefront sensorless aberration correction in digital micromirror based confocal microscopy”, *Optics Express*, vol. 25, no. 2, pp. 949–959, 2017. DOI: `https://doi.org/10.1364/oe.25.000949`.

[31] K. Singh, A. Dudley, and A. Forbes, “Versatile all-digital transport-of-intensity based wavefront sensor and adaptive optics using a dmd”, *Opt. Express*, vol. 31, no. 5, pp. 8987–8997, Feb. 2023. DOI: `https://doi.org/10.1364/OE.481767`.

[32] Q. Zhang, Q. Hu, C. Berlage, *et al.*, “Adaptive optics for optical microscopy”, *Biomed. Opt. Express*, vol. 14, no. 4, pp. 1732–1756, Apr. 2023. DOI: `https://doi.org/10.1364/BOE.479886`.

[33] D. Benton, “Aberration and coherence effects with a micromirror array”, in *Technologies for Optical Countermeasures XVIII and High-Power Lasers: Technology and Systems, Platforms, Effects V*, SPIE, vol. 11867, 2021, pp. 59–69. DOI: `http://dx.doi.org/10.1117/12.2597501`.

[34] M. Zandi, D. Benton, and K. Sugden, “Laser beam wavelength determination algorithm using a digital micromirror device”, *Optical Engineering*, vol. 62, no. 6, pp. 064 101–064 101, 2023. DOI: `https://doi.org/10.1117/1.OE.62.6.064101`.

[35] M. J. Booth, "Adaptive optics in microscopy", *Philosophical Transactions of the Royal Society A: Mathematical, Physical and Engineering Sciences*, vol. 365, no. 1861, pp. 2829–2843, 2007. DOI: https://doi.org/10.1098/rsta.2007.0013.

[36] M. J. Booth, "Adaptive optical microscopy: The ongoing quest for a perfect image", *Light: Science & Applications*, vol. 3, no. 4, e165–e165, 2014. DOI: https://doi.org/10.1038/lsa.2014.46.

[37] M. Young, "Zone plates and their aberrations", *Journal of the Optical Society of America*, vol. 62, no. 8, pp. 972–976, 1972. DOI: https://doi.org/10.1364/JOSA.62.000972.

[38] Texas Instruments, "DMD optical efficiency for visible wavelengths", Texas Instruments Incorporated, Application Note DLPA083B, Apr. 2023, Rev. B. [Online]. Available: https://www.ti.com/lit/pdf/DLPA083.

[39] R. J. Noll, "Zernike polynomials and atmospheric turbulence$*$", *J. Opt. Soc. Am.*, vol. 66, no. 3, pp. 207–211, Mar. 1976. DOI: https://doi.org/10.1364/JOSA.66.000207.

8

CONCLUSIONS AND OUTLOOK

CFS is an optical metrology technique based on scatterometry. It is sensitive to isolated, sub-wavelength, low-contrast particles and it has also been implemented in parameter inference of fabricated nanostructures. The technique is limited by the noise floor and in the past years, several implementations have been made to improve the signal-to-noise ratio and sensitivity. At its core, a lens transforms a collimated beam at the entrance pupil into a diffraction-limited focus, and the scattered field is measured in the Fourier plane (exit pupil). The optical system is therefore simple. Despite these advantages, the principal barrier to wider commercial adoption has been low scan speed. This work primarily sought to overcome that limitation. We explored several techniques to increase scan speed, each imposing distinct requirements on alignment tolerances, electronic bandwidth, optical power, and pre-calibration. Table 8.1 compares these scanning strategies across key system parameters. Each strategy has unique advantages and disadvantages and a specific technique can be chosen alone or in combination with other techniques based on the use case. The throughput values shown are for the implementations used in this thesis but are not fundamental limits.

Table 8.1: Scanning parameters (rows) compared across different scan strategies (columns).

	Scanning strategies				
Parameter	**Piezo**	**Multi-beam**	**Galvo-mirror**	**Rotation**	**DMD**
Hardware	P-625.2 CD (slow and fast axis)	P-625.2 CD (slow and fast axis)	GVS211/M (fast axis), P-625.2 CD, PI (slow axis)	Precilec 36SMOP-17 (rotation), P-611.3S (radial scan)	DLP9500, TI
Scan waveform	Triangle (fast axis); Staircase (slow axis)	Triangle (fast axis); Staircase (slow axis)	Sinusoidal (fast axis); Staircase (slow axis)	Motor driver at constant ω (fast axis); Staircase (slow axis)	FZP scanning, patterns projected on DMD.

Continued on next page

	Scanning strategies				
Parameter	**Piezo**	**Multi-beam**	**Galvo-mirror**	**Rotation**	**DMD**
Scan range ($x \times y$)	500 µm × 500 µm	600 µm × 500 µm	130 µm × 500 µm	π 80 µm × 80 µm	439.5 µm × 106 µm
Scan range limitation	Piezo travel	Piezo travel	Aberration-limited	Piezo travel (radial)	Relay optics
Pixel size	Δx =1.4 nm; Δy =1.4 nm	Δx =1.4 nm; Δy =1.4 nm	Δx =35 nm; Δy =1.4 nm	Δr =100 nm; $r\Delta\theta = \frac{v_{\mathrm{rot}}}{f_{\mathrm{s}}}$ [1] (tangential)	Δx =0.397 µm; Δy =0.397 µm
Max scan frequency (fast axis)	10.5 Hz	10.5 Hz	1 kHz	27.7 Hz	17.8 kHz [2]
Optical parameters	NA = 0.4; λ =632.8 nm	NA = 0.4; λ =632.8 nm	NA = 0.4; λ =632.8 nm	NA = 0.65; λ =635 nm	NA = 0.4; λ =632.8 nm
Cutoff frequency, (f_{cutoff}) [3]	1.264 μm^{-1}	1.264 μm^{-1}	1.264 μm^{-1}	2.047 μm^{-1}	1.264 μm^{-1}
Estimated bandwidth requirement	$(2x f_{\mathrm{scan}} + 10) f_{\mathrm{cutoff}} \approx$ 17.3 kHz	$(2x f_{\mathrm{scan}} + 10) f_{\mathrm{cutoff}} \approx$ 17.3 kHz	$\pi x f_{\mathrm{scan}} f_{\mathrm{cutoff}}$ $\approx$ 516.2 kHz	$2\pi r f_{\mathrm{scan}} f_{\mathrm{cutoff}}$ $\approx$ 17.6 kHz	$\Delta x f_{\mathrm{scan}} f_{\mathrm{cutoff}}$ $\approx$ 9 kHz
Advantages	Accurate positioning; Simple design; Identical PSF across scan range.	Linear speedup $\propto$ number of beams; Can be combined with other scanning strategies.	Fast beam scanning; Suitable for roll-to-roll manufacturing; Possible extension to 2D using dual-axis galvo mirror.	Continuous motion (no reversals); Large-area friendly; Low cost.	No macroscopic moving parts; High scan rate; Can correct off-axis aberrations; Parallelisation possible.
Limitations	Start–stop limits throughput; Long-scan drift.	Electronics complexity grows with N; Piezo-limited; Stitching overhead.	Angle-dependent detector shift; Field-of-view bounded by aberrations.	Centering and wobble critical; Non-linear sampling; Radius-dependent velocity.	Low power efficiency; Needs off-axis aberration correction; Pattern upload overhead.
Throughput (implemented in this thesis)	~500 s per 150 µm × 150 µm at Δy= 0.1 µm.	~167 s using N=3 beams for 150 µm × 150 µm area at Δy= 0.1 µm.	~ 1.5 s for 150 µm × 150 µm area at Δy= 0.1 µm.	~31 s for 150 µm × 150 µm area at Δr = 0.1 µm.	~8 s using 1-bit patterns for 150 µm × 150 µm area at Δx = 0.397 µm.

Continued on next page

---

[1] $v_{\mathrm{rot}=2\pi r f_{\mathrm{rot}}}$, f_{s} = sampling rate.

[2] 1-bit pattern rate.

[3] $f_{\mathrm{cutoff}} = \left(\frac{2\mathrm{NA}}{\lambda}\right)$, assuming no non-linear interactions.

	Scanning strategies				
Parameter	**Piezo**	**Multi-beam**	**Galvo-mirror**	**Rotation**	**DMD**
Throughput limitations for particular implementation	Piezo frequency	Number of beams and piezo frequency	Galvo frequency	Piezo range and detection bandwidth	DMD refresh rate

8.1. OUTLOOK 1: MASSIVELY PARALLEL CFS WITH EVENT-BASED DETECTION

A natural path to orders-of-magnitude higher throughput is to combine massively parallel illumination with event-based detection. Multiple, mutually non-interfering foci generated by a diffraction grating or a microlens array can probe the sample simultaneously, while an event sensor records only informative changes in the pupil signal. This decouples, to an extent, the large area scanning speed from bandwidth, reduces data volume to the number of events rather than the number of pixels, provided the analog bandwidth supports the fastest transitions for each pixel. Reconstruction then amounts to time-ordering events and mapping them onto the known scan trajectories for each focused spot. The scanning time reduces with the number of spots. For instance for a 100 × 100 spots reduces the scanning time for a given area by 10000× compared to a single spot system.

Near-term work can focus on modest parallelism with line detection and FPGA time stamping to validate linear throughput scaling. The principal challenges are calibration and synchronisation across beams, suppression of crosstalk through spacing, and robust event-to-position registration under varying SNR. With these addressed, the architecture can be extended to hundreds of beams, to scan mm-scale area, without ballooning bandwidth requirements. Schematics of the possible setups is shown in Figure 8.1.

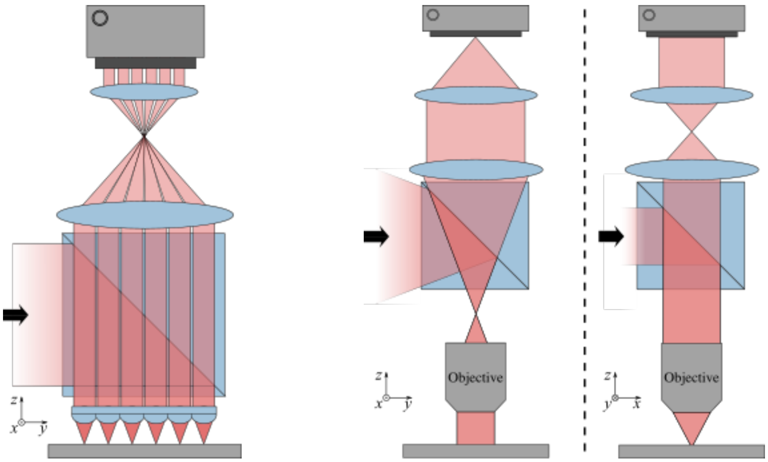

(a) (b)

Figure 8.1: Schematics of possible setups a) massively parallel CFS and b) line scanning CFS.

8.2. OUTLOOK 2: MINIATURISATION: ON-CHIP AND FIBER-BASED CFS

Fiber-based CFS targets remote or in-situ metrology using a single-mode/multimode/multicore fiber. The focusing of the light on the sample can be achieved with lensed fiber [1], beam shaping [2], [3], ball/GRIN lenses [4]–[6] or metasurfaces [7], [8]. Further, the path from laser to sample to detector can be fully fiber-based by using fiber-coupled light sources, fiber beamsplitter and fiber-coupled detectors. The strengths of this approach are that one can make use of a well-developed fiber technology to achieve a compact, rigid system with no bulk mechanics and straightforward packaging. The main challenges are the limited NA, working distance between probe and sample, back-reflection and limited pupil sampling.

An interesting extension of the technique would be to implement CFS on a photonic integrated circuit (PIC) [9]–[12]. Phase-controlled emitters or waveguide structures generate a diffraction-limited focus—or a small lattice of foci, a short distance above the chip and the scattered field is re-imaged into on-chip pupil samplers feeding parallel detectors, preserving the Fourier-plane measurement without bulk optics. The integration shortens the optical system, sets alignment by lithography, enabling straightforward parallelism. The principal challenges are the NA/field-of-view/working-distance trade-off set by chip aperture and coupling efficiency and insertion loss. With these addressed, a PIC-based CFS becomes a compact, programmable platform with parallel architecture.

BIBLIOGRAPHY

[1] D. R. Rivera, C. M. Brown, D. G. Ouzounov, W. W. Webb, and C. Xu, "Use of a lensed fiber for a large-field-of-view, high-resolution, fiber-scanning microendoscope", *Opt. Lett.*, vol. 37, no. 5, pp. 881–883, Mar. 2012. DOI: https://doi.org/10.1364/OL.37.000881.

[2] A. M. Caravaca-Aguirre, E. Niv, D. B. Conkey, and R. Piestun, "Real-time resilient focusing through a bending multimode fiber", *Optics express*, vol. 21, no. 10, pp. 12 881–12 887, 2013. DOI: https://doi.org/10.1364/OE.21.012881.

[3] A. D. Gomes, S. Turtaev, Y. Du, and T. Čižmár, "Near perfect focusing through multimode fibres", *Optics Express*, vol. 30, no. 7, pp. 10 645–10 663, 2022. DOI: https://doi.org/10.1364/OE.452145.

[4] T. M. Urner, A. Inman, B. Lapid, and S. Jia, "Three-dimensional light-field microendoscopy with a grin lens array", *Biomedical Optics Express*, vol. 13, no. 2, pp. 590–607, 2022. DOI: https://doi.org/10.1364/BOE.447578.

[5] H. J. Brueckner, L. Y. Chai, S. Tiedeken, V. Braun, and U. Teubner, "Design considerations and experimental investigations on fiber ball lens systems for optical metrology", *Journal of Physics: Photonics*, vol. 5, no. 3, p. 035 004, 2023. DOI: https://doi.org/10.1088/2515-7647/acdba6.

[6] T. Wu, Y. Huang, Y. Liu, *et al.*, "Ultrathin lensed fiber based anastigmatic needle probe for endoscopic swept source optical coherence tomography", *Optics and Lasers in Engineering*, vol. 154, p. 107 043, 2022. DOI: https://doi.org/10.1016/j.optlaseng.2022.107043.

[7] N. Xie, Z. Zhou, J. E. Fröch, *et al.*, "Inverse-designed large field-of-view polychromatic metalens for tri-color scanning fiber endoscopy", *Communications Engineering*, vol. 4, no. 1, p. 53, 2025. DOI: https://doi.org/10.1038/s44172-025-00377-7.

[8] A. Shanker, J. E. Fröch, S. Mukherjee, *et al.*, "Quantitative phase imaging endoscopy with a metalens", *Light: Science & Applications*, vol. 13, no. 1, p. 305, 2024. DOI: https://doi.org/10.1038/s41377-024-01587-y.

[9] H. Wang, F. H. Groen, S. F. Pereira, and J. J. M. Braat, "Optical waveguide focusing system with short free-working distance", *Applied Physics Letters*, vol. 83, no. 22, pp. 4486–4487, Dec. 2003, ISSN: 0003-6951. DOI: https://doi.org/10.1063/1.1631063.

[10] G. Yue and Y. Li, "Integrated lithium niobate optical phased array for two-dimensional beam steering", *Opt. Lett.*, vol. 48, no. 14, pp. 3633–3636, Jul. 2023. DOI: https://doi.org/10.1364/OL.491748.

[11] A. Tuniz, O. Bickerton, F. J. Diaz, *et al.*, “Modular nonlinear hybrid plasmonic circuit”, *Nature communications*, vol. 11, no. 1, p. 2413, 2020. DOI: https://doi.org/10.1038/s41467-020-16190-z.

[12] A. L. Hendriks, D. Rabelink, M. Dolci, *et al.*, “Detecting single nanoparticles using fiber-tip nanophotonics”, *Optica*, vol. 11, no. 4, pp. 512–518, Apr. 2024. DOI: https://doi.org/10.1364/OPTICA.516575.

A

DETAILS OF FDTD SIMULATIONS

The interaction between a sub-wavelength nanostructure and a focused spot is quite complex and needs to be modelled using a rigorous 3D Maxwell solver. These models can be used to provide a theoretical reference that can be compared to the experimental results for better understanding of the underlying physical phenomena behind the obtained scattered signals. For the FDTD simulations used in this work, a commercial solver (Lumerical, Ansys) is used [1].

For the simulations, the incident field consisted of a 0.4 NA focused spot with a wavelength of 633 nm. The field is linearly polarised in the x-direction at the back focal plane of the objective. The spot was precomputed analytically after solving the vectorial Debye integral using the formalism by Richards and Wolf [2] and was used as an imported source. Figure A.1 shows the schematic of the overall simulation model. The scattering object is a pit with a diameter of 400 nm and a depth of 150 nm etched into Si (refractive index = 3.882 + i0.019). The source is injected at a height of 200 nm from the Si surface. The scattered near field is recorded using a monitor placed at the height of 300 nm above the Si surface. The complete simulation domain has dimensions of 15 µm × 15 µm × 0.7 µm with perfectly matched layer (PML) boundary conditions. The far field or the field in the Fourier plane is calculated from the near field recorded using the monitor. The near-to-far-field projections are performed using in-built functions in the software [3].

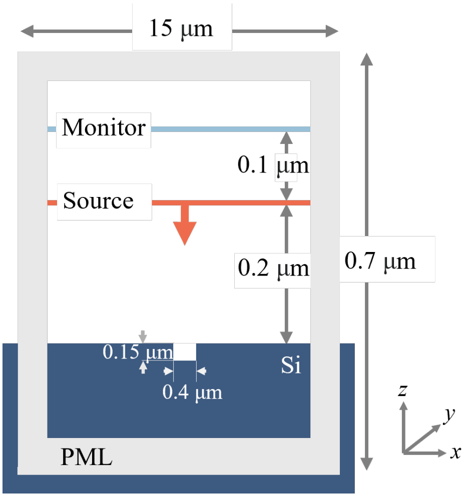

Figure A.1: Schematic of the FDTD simulation.

BIBLIOGRAPHY

[1] Ansys Lumerical FDTD, https://www.lumerical.com/, Accessed on: 15-02-2025.

[2] B. Richards and E. Wolf, “Electromagnetic Diffraction in Optical Systems. II. Structure of the Image Field in an Aplanatic System”, *Proceedings of the Royal Society of London Series A*, vol. 253, no. 1274, pp. 358–379, Dec. 1959. DOI: 10.1098/rspa.1959.0200.

[3] A. Taflove, S. Hagness, and M. Piket-May, “Computational electromagnetics: The finite-difference time-domain method”, in *The Electrical Engineering Handbook*. Elsevier Inc, Dec. 2005, pp. 629–670, ISBN: 9780121709600. DOI: 10.1016/B978-012170960-0/50046-3.

B

IMPROVEMENT IN PEAK-TO-PEAK OF DIFFERENCE SIGNAL FOR DEFOCUS ABERRATIONS

The following calculations are based on the work by Peng. et.al (1998) [1] and uses scalar approximation. Pupil-plane coordinates: $\mathbf{r} = (x, y)$ with $\rho = \sqrt{x^2 + y^2}$. Sample-plane coordinates: $\mathbf{s} = (u, v)$. Uniform illumination within a circular aperture with pupil phase $\phi(x, y)$:

$$P(x, y) = P_0(x, y)\, \mathrm{e}^{i\phi(x,y)}, \qquad P_0(x, y) = \mathrm{circ}(\rho). \tag{B.1}$$

Let S be the mark shape, centered at (u_0, v_0):

$$r(u, v) = \begin{cases} r_a, & (u - u_0,\, v - v_0) \in S, \\ r_c, & \text{otherwise}, \end{cases} \qquad \Delta r \equiv r_a - r_c. \tag{B.2}$$

Then the spectrum of $r(u, v)$ is

$$\mathscr{F}_{u,v}\{r(u, v)\}(f_u, f_v) = \mathrm{e}^{-i2\pi(f_u u_0 + f_v v_0)} \Big[\, r_c\, \delta(f_u)\, \delta(f_v) \;+\; \Delta r\, m(f_u, f_v) \Big], \tag{B.3}$$

where the shape spectrum m is

$$m(f_u, f_v) = \iint_S \mathrm{e}^{-i2\pi(f_u u + f_v v)}\, du\, dv. \tag{B.4}$$

The complex field amplitude of the reflected light at the exit pupil can be written as,

$$A(x, y) = P(x, y) * R(x, y), \tag{B.5}$$

$$\tag{B.6}$$

Pupil intensity:

$$I(x, y) = |A(x, y)|^2 = P_0(x, y) \Big(|r_c|^2 + |\Delta r|^2\, |F_\phi|^2 + 2\Re\{ r_c^*\, \Delta r\, \mathrm{e}^{-i\phi(x,y)}\, F_\phi(x, y) \} \Big). \tag{B.7}$$

where,

$$F_\phi(x,y;u_0,v_0) = \iint P(x',y')\, m\big(x-x',\, y-y'\big)\, \mathrm{e}^{-i2\pi[\,u_0(x-x')+v_0(y-y')\,]}\, dx'\, dy'. \tag{B.8}$$

$$= P(x,y) * m(x,y)\, \mathrm{e}^{-i2\pi[u_0 x + v_0 y]} \tag{B.9}$$

Left–right difference (right minus left) using the signum weight:

$$D_{LR} = \iint \operatorname{sgn}(x)\, P_0(x,y)\, I(x,y)\, dx\, dy, \tag{B.10}$$

$$= \frac{2}{\pi}\,\Re\big\{\, r_c^*\,(r_a - r_c)\, Q_1 \,\big\} + \frac{|r_a - r_c|^2}{\pi}\, Q_2, \tag{B.11}$$

with,

$$Q_1(u_0,v_0) = \iint \operatorname{sgn}(x)\, P_0(x,y)\, \mathrm{e}^{-i\phi(x,y)}\, F_\phi(x,y)\, dx\, dy, \tag{B.12}$$

$$= \iint \operatorname{sgn}(x)\, P(x,y)\, F_\phi(x,y)\, dx\, dy, \tag{B.13}$$

$$= \iint \Big[\mathscr{F}\{\operatorname{sgn}(x)\, P(x,y)\}(u,v)\Big]\, \mathscr{F}\{F_\phi\}(u,v)\, du\, dv, \quad \text{(Plancherel theorem)} \tag{B.14}$$

$$= \iint D(u,v)\, \widetilde{P}(u,v)\, M(u-u_0,\, v-v_0)\, du\, dv, \tag{B.15}$$

$$= \big(M * K_\phi\big)(u_0,v_0), \qquad K_\phi(u,v) = D(u,v)\, \widetilde{P}(u,v). \tag{B.16}$$

$$D(u,v) = \mathscr{F}\{\operatorname{sgn}(x)\, P(x,y)\}(u,v), \tag{B.17}$$

$$\tilde{P}(u,v) = \mathscr{F}\{P(x,y)\}(u,v), \tag{B.18}$$

$$M(u-u_0,\, v-v_0) = \mathscr{F}\{m(x,y)\, \mathrm{e}^{-i2\pi[u_0 x + v_0 y]}\}(u,v). \tag{B.19}$$

$$Q_2(u_0,v_0) = \iint \operatorname{sgn}(x)\, P_0(x,y)\, |F_\phi(x,y)|^2\, dx\, dy. \tag{B.20}$$

If $|\Delta r| \ll |r_c|$, then the quadratic term $|\Delta r|^2 Q_2$ is negligible compared to the linear term $2\Re\{r_c^*\, \Delta r\, Q_1\}$.

The identity

$$\mathscr{F}\{\rho^2 f\}(u,v) = -\frac{1}{4\pi^2}\, \Delta_{u,v}\big[\mathscr{F}\{f\}(u,v)\big], \quad \rho^2 = x^2 + y^2, \;\; \Delta_{u,v} = \partial_u^2 + \partial_v^2,$$

holds for any suitable f. In our case:

$$B_1(u,v) = \mathscr{F}\{P_0\,\phi\} = \alpha\,\mathscr{F}\{\rho^2 P_0\} = -\frac{\alpha}{4\pi^2}\,\Delta_{u,v}\,\underbrace{\mathscr{F}\{P_0\}}_{B_0} = -\frac{\alpha}{4\pi^2}\,\Delta B_0,$$

$$A_1(u,v) = \mathscr{F}\{\operatorname{sgn}(x)\, P_0\,\phi\} = \alpha\,\mathscr{F}\{\rho^2(\operatorname{sgn}(x) P_0)\} = -\frac{\alpha}{4\pi^2}\,\Delta_{u,v}\,\underbrace{\mathscr{F}\{\operatorname{sgn}(x) P_0\}}_{A_0} = -\frac{\alpha}{4\pi^2}\,\Delta A_0.$$

Thus

$$\delta K_{\text{defocus}} = -\frac{i\alpha}{4\pi^2}\Big(A_0^*\,\Delta B_0 - (\Delta A_0)^*\, B_0\Big).$$

With circular P_0 (even) and defocus ϕ (even), A_0, A_1 are odd/pure-imaginary in u, B_0, B_1 are even/real; hence δK is real and odd in the scan coordinate $\mathbf{r_0} = (u_0, v_0)$. For a symmetric sample, M is even thus the convolution $M * K_\phi(u_0, v_0)$ remains odd. The peak-to-peak is calculated as, $D_{LR}(\mathbf{r}) - D_{LR}(-\mathbf{r})$. A small defocus produces a linear change in the peak-to-peak value, its sign set by the sign of the defocus coefficient and the sample spectrum through the convolution with δK. The difference signal for a symmetric sample and even aberration mode is also symmetric.

BIBLIOGRAPHY

[1] C. Peng, W.-H. Yeh, and M. Mansuripur, “Measurements and simulations of differential phase-tracking signals in optical disk data storage”, *Appl. Opt.*, vol. 37, no. 20, pp. 4425–4432, Jul. 1998. DOI: `https://doi.org/10.1364/AO.37.004425`.

C

AREA OF INFLUENCE OF A SPOT

The sensitivity of our detection system is fundamentally limited by its noise floor. For the multi-beam coherent Fourier scatterometry setup described in Figure 4.1, the detector output has a maximum measurable range of 2 V_{pp}, limited by the analog-to-digital converter (ADC). The measured noise floor, including electronic noise, laser fluctuations, and positioning uncertainties, is approximately 35.9 mV_{pp}. This corresponds to a dynamic range of about 35 dB.

To quantify the effective area of influence of an individual focused optical spot, the signal generated by scanning a small scatterer is simulated under ideal conditions, explicitly excluding optical aberrations, electronic noise, and surface roughness. The rigorous 3D electromagnetic simulation was performed using the FDTD solver, Lumerical. The simulated domain consisted of a Si substrate ($n = 3.882 + i0.019$) with an etched pit of 1 µm diameter and 150 nm depth. The illumination was an x-polarised focused beam with an NA of 0.4 at a wavelength of 633 nm. The simulation domain spans 15 µm × 15 µm × 0.7 µm.

We assume the largest scatterer measurable without saturating the detector is the 1 µm etched pit. The effective spot radius is defined as the maximum distance from the focused spot center to the scatterer, at which the signal peak-to-peak remains at least twice the noise floor (71.8 mV_{pp}). Due to differential detection and input source polarisation, the effective radius differs along the scan direction (x-axis) and orthogonal direction (y-axis).

From simulation results in Figure C.1, the effective radius is:

- Along x-direction (scan direction): 1.596 µm,
- Along y-direction (orthogonal direction): 0.818 µm.

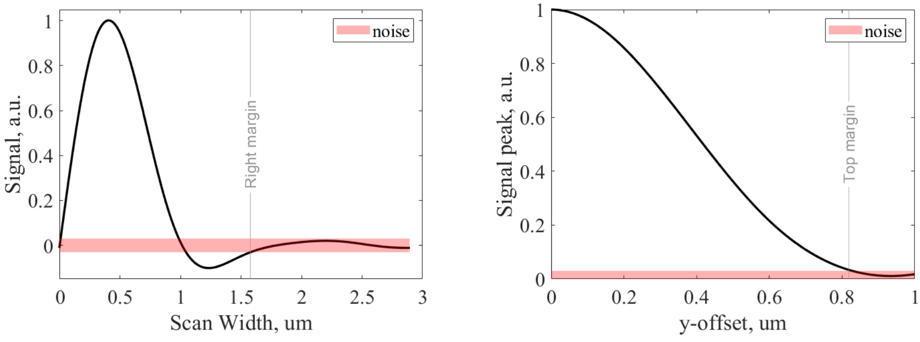

(a) (b)

Figure C.1: Simulated detector signals for a 0.4 NA focused beam at 633 nm wavelength scanning across an etched pit of 1000 nm diameter and 150 nm depth: (a) differential signal when scanning along the x-axis passing directly through the center of the scatterer; (b) the peak-to-peak of the differential signal for scans along the x-axis with varying lateral offsets (y-axis) from the scatterer. The red horizontal line indicates twice the noise floor threshold.

D

BEAM SHIFT CALCULATION DUE TO GALVO MIRROR OFFSET

In this section, the beam shift after the galvo reflection is calculated in the exit pupil plane. This plane is chosen since the pupil plane can be related with ease to the image plane or the sample plane using a simple Fourier transform.

Let the rotation axis of the galvo mirror be shifted from the back focal plane (BFP) by dz. Further, let the incident beam be shifted by d from the mirror rotational axis. Figure Figure D.1 shows the diagram of the galvo mirror scan including the incident and reflected beams. **LM** represents the galvo mirror rotated about the rotational axis by an arbitrary amount θ and $\mathbf{L'M'}$ the unrotated galvo mirror with the mirror tilted by 45° with respect to the optical axis. **UV** and $\mathbf{UV'}$ represent the incident beam when the mirror is rotated and unrotated respectively. **VW** and $\mathbf{V'W'}$ are the corresponding reflected beams. The shift is calculated by extending the beams to the BFP. The two reflected beams intersect the BFP at C and B respectively. VN is the mirror normal at the point of incidence of the beam. The angle of incidence, ∠UVN, and the angle of reflection, ∠NVW can be calculated from simple trigonometric relations to be $45^\circ - \theta$. **AS** is the normal to the BFP drawn through the rotational axis of the galvo mirror.

Consider the triangles $\triangle$RVS and $\triangle$RV′S: $\angle \mathrm{RV'S} = 45^\circ$, $\angle \mathrm{RVS} = 45^\circ + \theta$, and $\angle \mathrm{VRS} = 45^\circ - \theta$.

$$\begin{aligned}\mathbf{VV'} &= \mathbf{V'S} - \mathbf{VS}\\ &= d - \frac{d}{\tan 45^\circ + \theta}\\ &= \frac{2d\tan\theta}{1+\tan\theta}\end{aligned}$$

Now consider the triangles formed by the two reflected beams, $\triangle$OVV′ and $\triangle$OCB. $\angle \mathrm{OV'V} =$

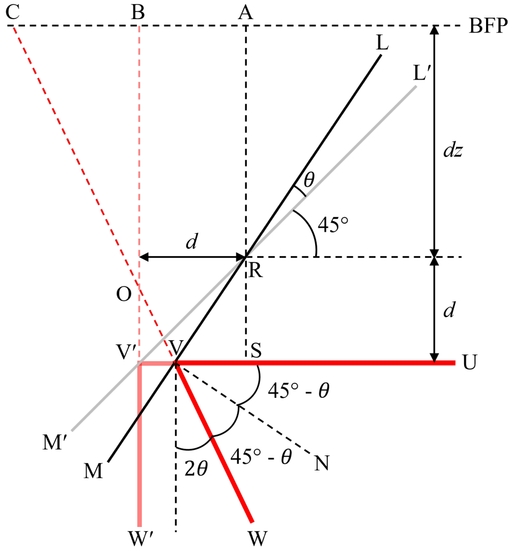

Figure D.1: Galvo mirror shifted from the exit pupil by dz.

$\angle \mathrm{OBC} = 90°$, $\angle \mathrm{OVV'} = \angle \mathrm{OCB} = 90° - 2\theta$, and $\angle \mathrm{V'OV} = \angle \mathrm{COB} = 2\theta$.

$$
\begin{aligned}
\mathbf{BV'} &= d + dz \\
\mathbf{OV'} &= \frac{\mathbf{VV'}}{\tan 2\theta} \\
&= d(1 - \tan\theta) \\
\mathbf{OB} &= \mathbf{BV'} - \mathbf{OV'} \\
&= dz + d\tan\theta \\
\mathbf{BC} &= \mathbf{OB}\tan 2\theta \\
&= (dz + d\tan\theta)\tan 2\theta
\end{aligned}
$$

Thus the total shift, $\delta = (dz + d\tan\theta)\tan 2\theta$. The BFP is related to the image plane by Fourier transform [1]. The beam tilt translates to shift of the focused spot in the image plane and vice versa. Let (x_o, z_o) be the coordinates in the BFP, (x_i, z_i) be the coordinates in the image plane and f be the focal length of the Fourier transforming lens. If $U(x_o)$ is the field in the BFP, the field in the image plane is calculated as,

$$U(x_i) = \frac{1}{\mathrm{i}\lambda f}\int_{-\infty}^{\infty} U(x_o)\exp\left[-\mathrm{i}\frac{2\pi}{\lambda f}x_i x_o\right]dx_o. \tag{D.1}$$

The shifted beam can be denoted as $U(x_o - \delta)$, where $\delta = |\mathbf{BC}|$. The tilted focused spot at the image plane is,

$$U(x_i) = \exp\left[-\mathrm{i}\frac{2\pi}{\lambda f}\delta x_i\right]\mathscr{F}\{U(x_o)\}(x_i) \tag{D.2}$$

The field after reflection from the image plane is,

$$U(x_i) = \exp\left[\mathrm{i}\frac{2\pi}{\lambda f}\delta x_i\right]\mathscr{F}\{U(x_o)\}(x_i) \tag{D.3}$$

The reflected field is again Fourier transformed by the same lens. The field at the BFP after reflection is $U(-x_o+\delta)$. Thus the shift after reflection from the sample remains the same but flipped about the rotation axis.

E

FREQUENCY SPREAD CALCULATION: HYPERPARAMETER OPTIMISATION

The choice of n used to calculate $S(x)$ (or $S(y)$) is determined qualitatively. Low values n results in a noisy spread - piezo position curve while large values of n broadens the minima. Figure E.1 plots $S(y)$ calculated using $n = 2$ and $n = 10$ respectively for the same scan. The plot calculated using $n = 2$ is much more noisy compared to the plot calculated using $n = 10$. However, the minima is much more sharper for $n = 2$ compared to $n = 10$. In both cases, the minima becomes hard to determine and ultimately the choice made is a compromise between the two.

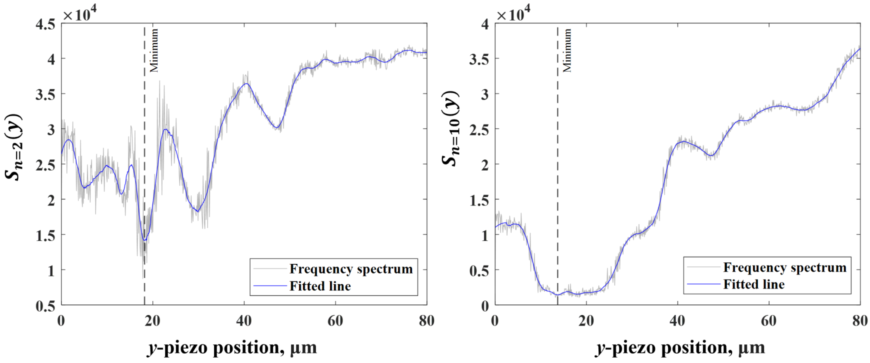

(a) (b)

Figure E.1: Frequency spread as a function of the piezo position along the y-direction with the spread calculated using a) $n = 2$ and b) $n = 10$. Low values of n create a noisy spread-piezo position curve while large values spread the minima.

F

ZERNIKE MODES OPTIMISATION

This appendix supplements the aberration-correction subsection of chapter 7 by documenting how Zernike modes were optimised to homogenise the focus spot across the scan field. At each scan coordinate, individual Zernike coefficients C_n^m (Noll indexing, units of waves at $\lambda = 632.8\,\mathrm{nm}$) were swept while imaging the spot on a camera conjugate to the sample plane. The merit function was the fitted peak intensity. The FWHM along x and y, and the asymmetry metric ϵ (as defined in the main text) is also recorded. Figure F.1 shows convergence of these metrics over one optimisation pass, Figure F.2 shows an example coefficient sweep with Gaussian fits used to estimate the optimal C_n^m, and Figure F.3 shows the 2D maps of the retrieved optimal coefficients across the field of view. Unless noted otherwise, piston, tip and tilt were excluded and the first 14 non-trivial modes were considered.

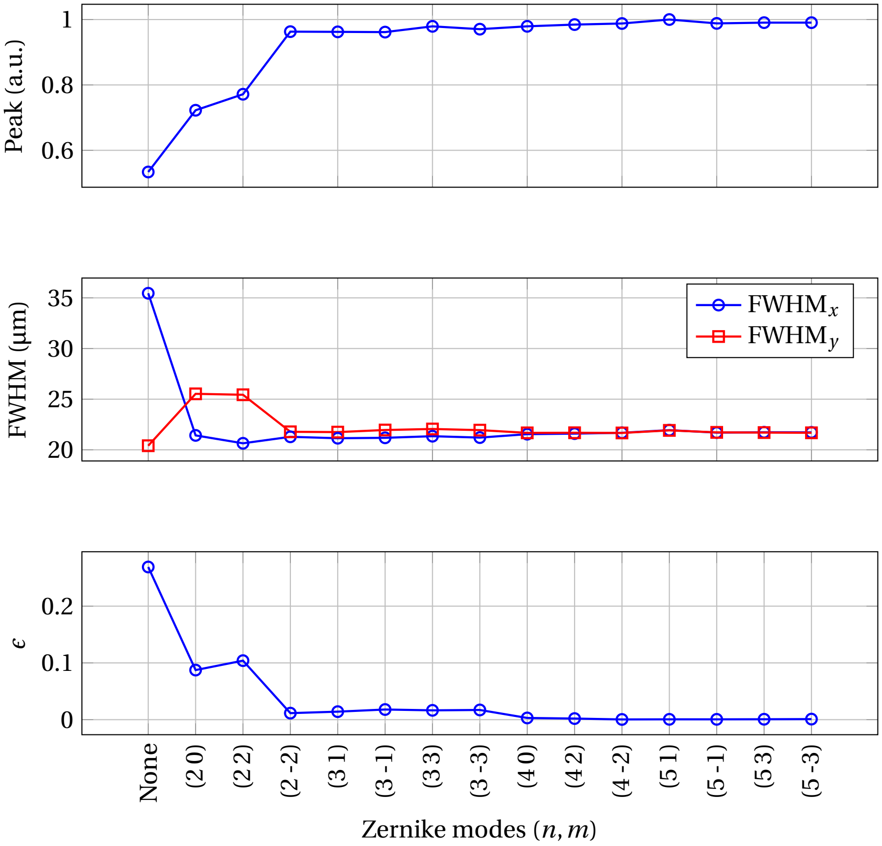

Figure F.1: Convergence of peak, FWHM, and ϵ across one optimisation pass. The first data point for the three plots correspond to the base values before optimisation.

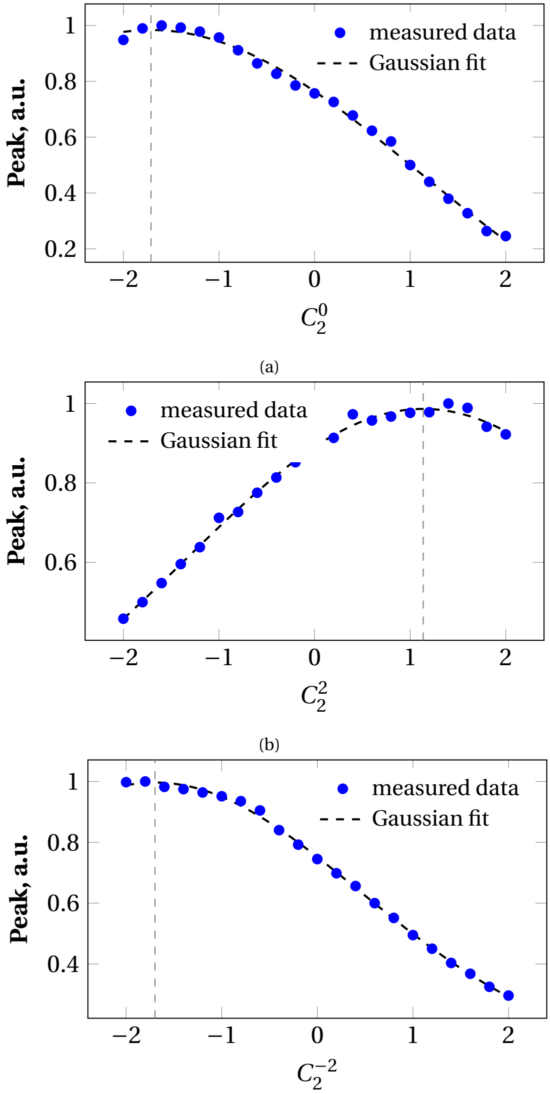

(a)

(b)

(c)

Figure F.2: Measured peaks vs. coefficient (blue markers), Gaussian fits (black dashed), and optimal coefficient (gray line) for a) defocus (Z_2^0), b) astigmatism (Z_2^2), and c) oblique astigmatism aberrations. The peaks correspond to the maximum intensity of the focus spot captured using a CCD camera.

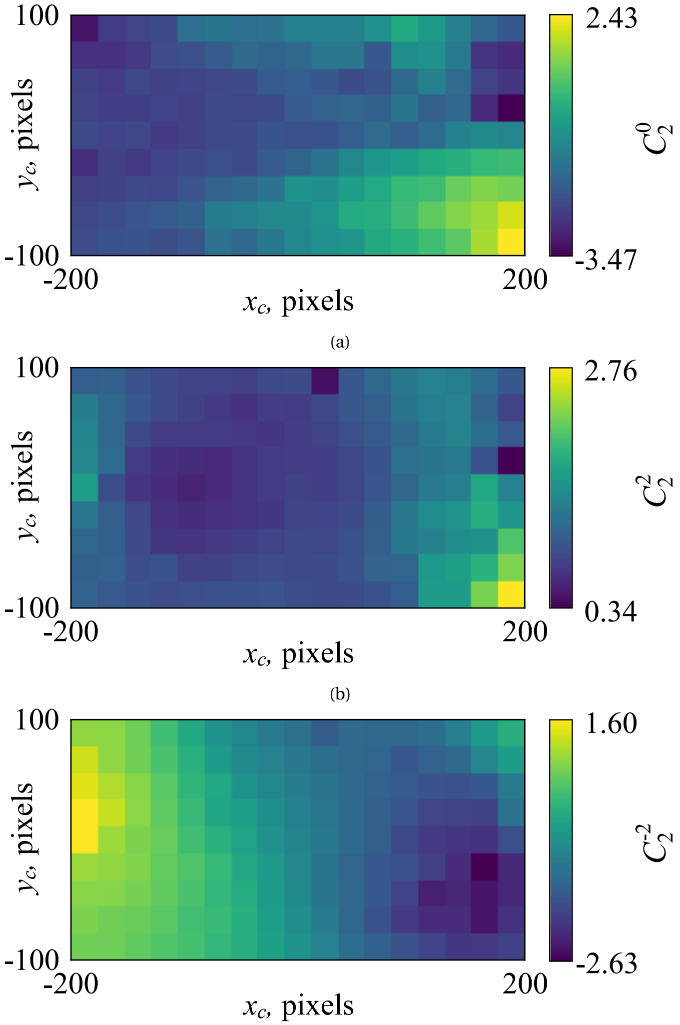

(a)

(b)

(c)

Figure F.3: The 2D heatmap of the optimal coefficients for a) defocus (Z_2^0), b) astigmatism (Z_2^2), and c) oblique astigmatism aberrations.

CURRICULUM VITÆ

Sarika Soman

24-2-1997	Born in Kerala, India.

EDUCATION

2006–2015	Bharatiya Vidya Bhavan's Vidya Mandir, Irinjalakuda, India
2015–2019	Bachelor of Technology in Engineering Physics, National Institute of Technology, Calicut, India
2019–2021	Masters in Applied Physics, Delft University of Technology, Netherlands
2019	PhD candidate, Delft University of Technology, Netherlands *Thesis:* High-speed coherent Fourier scatterometry *Promotor:* Prof. dr. S. F. Pereira

AWARDS

2011	National Talent Search Examination Scholarship
2019	Justus van Effen Excellence scholarship

LIST OF PUBLICATIONS

10. **S. Soman, E. Özdemir, S. F. Pereira**, *Scanning in coherent Fourier scatterometry using Fresnel zone plate projection on a digital micro-mirror device*, Measurement Science and Technology **37**, 155002 (2026)
9. **A. Paniate, G. Ortolano, S. Soman, M. Genovese, I. Ruo-Berchera**, *High-resolution quantum-enhanced phase imaging of cells*, Optica **13**, 3 (2026)
8. **S. Soman, R. C. Horsten, S. F. Pereira**, *High-Speed Coherent Fourier Scatterometry: Galvo Mirror Integration for Fast Surface Inspection*, Measurement **258**, 119294 (2025)
7. **S. Soman, S. F. Pereira**, *Aberration characterisation in coherent Fourier scatterometry*, Proc. SPIE **13567**, Optical Measurement Systems for Industrial Inspection XIV, 135672J (2025).
6. **S. Soman, B. In't Velt, R. C. Horsten, S. F. Pereira**, *Coherent Fourier scatterometry using rotational scanning*, Optical Engineering **64**, 074106 (2025).
5. **A. Paul, R. Wever, S. Soman, S. F. Pereira**, *Utilizing focused field as a probe for shape determination of subwavelength structures via coherent Fourier scatterometry*, Physical Review Applied **23**, 024016 (2025).
4. **S. Soman, S. F. Pereira**, *Beam scanning coherent Fourier scatterometry*, Proc. SPIE **13024**, Optical Instrument Science, Technology, and Applications III, 1302408 (2024).
3. **S. Soman, R. C. Horsten, T. Scholte, S. F. Pereira**, *Multi-beam coherent Fourier scatterometry*, Measurement Science and Technology **35**, 075905 (2024).
2. **G. Ortolano, A. Paniate, P. Boucher, et al.**, *Quantum enhanced non-interferometric quantitative phase imaging*, Light Science & Applications **12**, 171 (2023).
1. **S. Soman, S. F. Pereira, O. El Gawhary**, *Diffraction grating parameter retrieval using nonparaxial structured beams in coherent Fourier scatterometry*, Journal of Optics **24**, 034006 (2022).

ACKNOWLEDGEMENTS

This thesis is the result of many generous investments of time, patience, and expertise by people around me. I am deeply grateful to everyone who helped turn a set of ideas into a working set of instruments, experiments, and finally these pages.

First and foremost, I thank my daily supervisor and promotor Dr. Silvania Pereira for her constant support over the four years. You were always supportive, up for a visit to the lab anytime of the day and your door was always open. I have been lucky to be able rely on your feedback for all the numerous presentations, posters, articles or reports and I admire the way you conduct yourself with warmth in every interaction. I thank Dr. Omar El Gawhary for his constructive discussions during the PhD meetings. Every conversation with you from the first day of Advanced photonics course has been a source of endless motivation. I am deeply appreciative of your supervision and constant motivation since the master thesis and regret only that we did not interact as frequently during the PhD. Your love and passion for physics is something I can only hope to strive for.

This work relied on excellent technical support. I thank Roland Horsten for all the detectors and the labVIEW programs. I could always rely on you for everything from the electronics and feedback on the writing to even how to get rid of rats. You have been a constant source of support and I am so grateful to have worked with you during the past four years. I thank Thim Zuidwijk for all his support with everything optics. You have always been kind and I am grateful for all the discussions over coffee and in the office. It still suprises me that when i come to you about some new device or method that i read about or saw and you are like yes we have that in the group from the 60s. Without you and Roland the PhD would have taken twice as long and would not have been half as good. I thank Thomas Scholte for his help with the detectors, stages and all the 3D printed parts. I still don't know anyone else who enjoys watching as many weird movies as you do. I hope you watch more malayalam movies as well. I'm grateful to Carel and Anna for being amazing mentors and helping out with everything in the cleanroom.

I want to thank the current and previous members of the scatterometry group. Anubhav, we have been both office mates and group mates for the past four years. Thank you for all the closed door gossip sessions. It was great fun. I hope you have a grand north Indian style grand wedding that I can attend. I wish you all the best for whatever comes later. Dmytro, you were a postdoc when I started and was a constant support. I thank you for the readiness and enthusiasm with which you approached all new projects. You always had a really curious perspective to different problems. I appreciate all the helpful discussions. I cherish the time spent with Jila, you were always warm and ready to help with anything.

I want to thank the other members in the Synoptics consortium - Marnix, Paul, Peter, Eric, Sven, and Max for their helpful discussions and encouragements during all the project meetings.

It was an immense pleasure to share the office with Alex, Bruno and Hui. All the best for your upcoming defences. Thanks to Zizheng for really insightful discussions both inside the cleanroom and in the office; to Sander for his infectious enthusiasm for science; Luuk for all the random conversations in the corridor and for the Welford sessions with Reint; Jan for all the contrarian discussions; Sven, Thomas (plural), Roald, Hong, Rishav, Frank for all the coffee sessions, table tennis matches and dinners.

On the personal side, I owe a lot to friends who kept me balanced. Thank you for all the Friday night dinners and the countless chai sessions. Finally, and most importantly, I thank my family. To

my parents, Amma and Pappa, for their unconditional encouragement and to my grandmother, for celebrating every small milestone along the way, my brother, all my aunts, uncles and cousins, this thesis is for you.

വിശ്വനാഥ് ഈ തീസിസിന്റെ ഐശ്വര്യം.